


1-2-2013

Exergetic Analysis Of Hydrogen Combustion Involving Electronically Excited Species

Devon Alan Washington
Wayne State University,

Follow this and additional works at: http://digitalcommons.wayne.edu/oa_dissertations

 Part of the [Chemistry Commons](#), and the [Mechanical Engineering Commons](#)

Recommended Citation

Washington, Devon Alan, "Exergetic Analysis Of Hydrogen Combustion Involving Electronically Excited Species" (2013). *Wayne State University Dissertations*. Paper 809.

This Open Access Dissertation is brought to you for free and open access by DigitalCommons@WayneState. It has been accepted for inclusion in Wayne State University Dissertations by an authorized administrator of DigitalCommons@WayneState.

**EXERGETIC ANALYSIS OF HYDROGEN COMBUSTION INVOLVING
ELECTRONICALLY EXCITED SPECIES**

by

DEVON A. WASHINGTON

DISSERTATION

Submitted to the Graduate School

of Wayne State University,

Detroit, Michigan

in partial fulfillment of the requirements

for the degree of

DOCTOR OF PHILOSOPHY

2013

MAJOR: MECHANICAL ENGINEERING

Approved by:

Advisor

Date

DEDICATION

I would like to dedicate this work to the memory of my grandmother Martha Elizabeth Ford for being the ultimate example of dedication, consistency, and steadfastness.

I would also like to acknowledge the memory of Lee Bayer Shapiro for her long standing commitment to equality and well-being for all.

ACKNOWLEDGMENTS

I would like to acknowledge my mother Linda Louise Ford for being a tremendous mother, and for always being in full support of my academic endeavors and positive personal development. To my father Thomas Alan Washington, who initiated and nurtured my interest in science and engineering with many discussions regarding the fundamental nature of the universe; which we still have to this day. To all of my family and friends who have supported and encouraged me throughout this journey, without your support this would not be possible.

I would like to thank Dr. Howard N. Shapiro for your mentorship and tutelage regarding the many complexities of exergy analysis and its proper application. Your passion for education and the proliferation of knowledge is notable; it has definitely enhanced my understanding of thermodynamics. I would like to thank Dr. Trilochan Singh for your advice and direction with navigating my academic career while at Wayne State, it was very much appreciated. I would also like to acknowledge and thank Dr. Marcis Jansons for granting me access to CHEMKIN, as well as for many thoughtful discussions regarding its use. To Dr. Walter Bryzik, thank you for your leadership in fostering a challenging academic environment inside the department; I have increased my knowledge base a great deal through interactions with the faculty. To Dr. H. Bernhard Schlegel, thank you for consultation and advice in the nuances of quantum chemistry and electronic structure. I thank you all for serving on my committee and bring your wisdom and knowledge to bear on this research project; it has been a pleasure to work with you.

I would like to acknowledge Consumers Energy's Engineering Services Department (ESD) for their unwavering support throughout this process, and more importantly for providing me with the opportunity to live engineering. To James B. Lewis, P.E. and David J. Hubert, P.E.

thanks for the many enlightening conversations regarding thermodynamics and its applications to electric power generation. To my former supervisor Robert T. Gilmore, P.E., thank you for the many discussions regarding professional development and work-life in general. I would also like to acknowledge my current supervisor LeRoy N. Reiss, P.E. and the manager of ESD Scott D. Thomas, P.E., for creating a challenging technical work environment conducive to professional growth and excellence.

To my master's thesis advisor Dr. Abraham Engeda, I would like to extend my gratitude for the mentoring and guidance provided while at Michigan State University. This played a key role toward advancing my education. I would also like to acknowledge Dr. Percy Pierre and Dr. Barbara O'Kelly for their support; as well as the significant impact they have had through the development and implementation of several programs, such as, the NACME Alfred P. Sloan Foundation Graduate Scholarship Program. I would also like to recognize several Michigan State University, Department of Mechanical Engineering faculty who imparted the fundamental skillsets necessary to make this possible.

I would like to recognize Dr. Alec D. Gallimore and Bonnie Bryant for their work with the Michigan Space Grant Consortium, which provides a venue to present and discuss research in a fun and inviting atmosphere.

PREFACE

In recent years a considerable amount of attention has been devoted toward developing energy management strategies that will allow for more efficient use of energy resources. At the onset of my doctoral studies, Dr. Shapiro and I spent a considerable amount of time developing a research topic that would address this issue in a novel way. A better part of a year was spent doing an extensive literature review on the field of plasma-assisted combustion (PAC). As our familiarity grew on the subject, it became apparent that, for all its promising benefits with regard to enhancing combustion through modification of the fundamental chemical kinetics of the reaction, no one was asking the question “How does PAC impact exergetic efficiency?” It was that point forward that our full attention was set on how to develop an exergetic model of a PAC system.

The goal of this research project is not only to explore alternative means to enhance combustion efficiency, but also encourage a dialog between the PAC and exergy communities.

TABLE OF CONTENTS

Dedication	ii
Acknowledgments	iii
Preface	v
List of Tables	x
List of Figures	xi
Nomenclature	xviii
Chapter 1 Introduction	1
1.1 Motivation	1
1.2 Objective	2
1.3 Methodology	3
1.4 Literature Review	5
1.4.1 Exergy Analysis	6
1.4.2 Plasma-Assisted Combustion	9
Chapter 2 Nonthermal Plasma	12
2.1 Classifications of Plasma	12
2.1.1 Thermal Plasma	13
2.1.2 Nonthermal Plasma	14
2.2 Nonthermal Plasma Generation	15
2.2.1 NTP Generation Using Electric Fields	16

2.2.2	Electronic Excitation and Structure of Molecular Oxygen.....	17
Chapter 3	Chemical Simulation.....	18
3.1	Gas-Phase Kinetics.....	19
3.1.1	Mechanism Description	19
3.1.2	Selection of Inert Diluent Species.....	20
3.1.3	Thermodynamic Data.....	21
3.2	Plug Flow Reactor Model	22
3.2.1	Assumptions.....	22
3.2.2	Governing Equations	23
3.2.3	Inlet Conditions.....	24
3.3	Post Processing Algorithm.....	26
Chapter 4	Exergy Analysis of PAC Systems.....	26
4.1	Components of Exergy Analysis.....	26
4.1.1	Exergy Reference Environment and the Dead State.....	27
4.1.2	Governing Equations	29
4.1.3	Chemical Exergy of Electronically Excited Species	33
4.2	Exergy Analysis Results.....	34
4.2.1	Characterization of Combustion Zones	34
4.2.2	Exergy Destruction and Exergetic Efficiency.....	36
4.3	Reaction Mechanism Analysis Results	45

4.3.1	Background on Hydrogen-Oxygen Combustion	46
4.3.2	Sensitivity and Reaction Flow Analyses.....	47
4.4	Summary of Findings.....	84
4.4.1	Exergy Analysis Findings.....	84
4.4.2	Reaction Mechanism Findings.....	86
4.4.3	Comprehensive Review	87
Chapter 5	Parametric Study of PAC Systems	89
5.1	Aspects of the Parametric Study	89
5.1.1	Overview of Study Objectives	89
5.2	Selection of Combustion Parameters	89
5.3	Parametric Study Results	90
5.3.1	Present Model Results.....	90
5.3.2	Literature Model Results.....	99
5.4	Summary of Findings.....	102
5.4.1	Comprehensive Review	102
Chapter 6	Conclusions.....	103
6.1	Summary	103
6.2	Conclusions	106
6.3	Accomplishments.....	107
6.4	Future Work	108

Appendix A: Reaction Mechanism.....	109
Appendix B: Thermodynamic Data.....	115
Appendix C: Post Processing Algorithm.....	116
References.....	119
Abstract.....	131
Autobiographical Statement.....	133

LIST OF TABLES

Table 3.1 Moscow State University mechanism species [3, 5]	19
Table 3.2 Inlet conditions for Phase I, Model IA and Model IB [59].....	25
Table 3.3 Combustion parameters for Phase II parametric study	25
Table 4.1 Exergy reference environment [59]	28
Table A.1 Moscow State University mechanism [3, 5]	109
Table B.1 Thermodynamic polynomial curvefit coefficients [4, 52]	115

LIST OF FIGURES

Figure 1.1 World energy consumption [1].....	1
Figure 1.2 World energy consumption by fuel [1]	2
Figure 1.3 Method of approach.....	4
Figure 1.4 Constituent disciplines for exergy analysis of PAC system.....	5
Figure 1.5 Modes of combustion irreversibility [2].....	7
Figure 1.6.A-D Plasma-assisted combustion technologies [34]	11
Figure 2.1 Categories of NTPs as a function of reduced electric field [29]	16
Figure 2.2 Molecular orbital diagram of oxygen [47]	17
Figure 3.1 Influence of dilution on laminar flame speed validation results, for atmospheric H ₂ -O ₂ flames diluted with: (★) N ₂ , (●) Ar, (■) He (ratio O ₂ :N ₂ = O ₂ :Ar = O ₂ :He = 1:3.76). Line MSU model, symbols empirical data [3]	20
Figure 3.2 Rate balances for a differential plug.....	24
Figure 4.1 Exergy rate balance of a differential plug	29
Figure 4.2 Characterization of combustion zones.....	35
Figure 4.3 Flow exergy and exergy destruction vs. distance for 0% inlet O ₂ (a ¹ Δ _g) [59]	37
Figure 4.4 Flow exergy and exergy destruction vs. distance for 10% inlet O ₂ (a ¹ Δ _g) [59]	38
Figure 4.5 Flow exergy and exergy destruction vs. distance for 25% inlet O ₂ (a ¹ Δ _g).....	38
Figure 4.6 Exergy destruction and temperature vs. distance for 0% inlet O ₂ (a ¹ Δ _g) [59].....	39
Figure 4.7 Total exergy destruction before ignition and ignition temperature vs. inlet percentages of O ₂ (a ¹ Δ _g) [59]	41
Figure 4.8 Exit thermomechanical flow exergy and exit temperature vs. inlet percentages of O ₂ (a ¹ Δ _g) [59].....	41

Figure 4.9 Exit chemical flow exergy and molar conversion of H_2 vs. inlet percentages of $O_2(a^1\Delta_g)$ [59]	42
Figure 4.10 Completeness of combustion and exit temperature vs. inlet percentages of $O_2(a^1\Delta_g)$	44
Figure 4.11 Exergy destruction and exergetic efficiency of combustion vs. inlet percentages of $O_2(a^1\Delta_g)$ [59]	44
Figure 4.12 Reaction flow diagram for 0% inlet $O_2(a^1\Delta_g)$, $\Phi = 1$, and $T_{in} = 1200$ K [59]	47
Figure 4.13 Mole fractions of primary species vs. distance for 0% inlet $O_2(a^1\Delta_g)$, $\Phi = 1$, and $T_{in} = 1200$ K	49
Figure 4.14 Mole fractions of radicals and chain carriers vs. distance for 0% inlet $O_2(a^1\Delta_g)$, $\Phi = 1$, and $T_{in} = 1200$ K	49
Figure 4.15 Temperature and volumetric heat release rate vs. distance for 0% inlet $O_2(a^1\Delta_g)$, $\Phi = 1$, and $T_{in} = 1200$ K	50
Figure 4.16 Global sensitivity analysis of the overall mechanism for 0% inlet $O_2(a^1\Delta_g)$, $\Phi = 1$, and $T_{in} = 1200$ K	52
Figure 4.17 Global sensitivity analysis of O_2 for 0% inlet $O_2(a^1\Delta_g)$, $\Phi = 1$, and $T_{in} = 1200$ K	52
Figure 4.18 Local sensitivity analysis of O_2 for 0% inlet $O_2(a^1\Delta_g)$, $\Phi = 1$, and $T_{in} = 1200$ K	53
Figure 4.19 Local rate of production of O_2 for 0% inlet $O_2(a^1\Delta_g)$, $\Phi = 1$, and $T_{in} = 1200$ K	53
Figure 4.20 Total rate of production of O_2 for 0% inlet $O_2(a^1\Delta_g)$, $\Phi = 1$, and $T_{in} = 1200$ K	54
Figure 4.21 Global sensitivity analysis of OH for 0% inlet $O_2(a^1\Delta_g)$, $\Phi = 1$, and $T_{in} = 1200$ K	54

Figure 4.22 Local sensitivity analysis of OH for 0% inlet $O_2(a^1\Delta_g)$, $\Phi = 1$, and $T_{in} = 1200$ K	55
Figure 4.23 Local rate of production of OH for 0% inlet $O_2(a^1\Delta_g)$, $\Phi = 1$, and $T_{in} = 1200$ K	55
Figure 4.24 Total rate of production of OH for 0% inlet $O_2(a^1\Delta_g)$, $\Phi = 1$, and $T_{in} = 1200$ K	56
Figure 4.25 Global sensitivity analysis of temperature for 0% inlet $O_2(a^1\Delta_g)$, $\Phi = 1$, and $T_{in} = 1200$ K	56
Figure 4.26 Local sensitivity analysis of temperature for 0% inlet $O_2(a^1\Delta_g)$, $\Phi = 1$, and T_{in} $= 1200$ K	57
Figure 4.27 Volumetric heat release rate for R17 for 0% inlet $O_2(a^1\Delta_g)$, $\Phi = 1$, and $T_{in} =$ 1200 K	57
Figure 4.28 Total rate of production for OH and exergy destruction vs. distance for 0% inlet $O_2(a^1\Delta_g)$, $\Phi = 1$, and $T_{in} = 1200$ K	58
Figure 4.29 Reaction flow diagram for 10% inlet $O_2(a^1\Delta_g)$, $\Phi = 1$, and $T_{in} = 1200$ K [59]	59
Figure 4.30 Mole fractions of primary species vs. distance for 10% inlet $O_2(a^1\Delta_g)$, $\Phi = 1$, and $T_{in} = 1200$ K	60
Figure 4.31 Mole fractions of radicals and chain carriers vs. distance for 10% inlet $O_2(a^1\Delta_g)$, $\Phi = 1$, and $T_{in} = 1200$ K	62
Figure 4.32 Temperature and volumetric heat release rate vs. distance for 10% inlet $O_2(a^1\Delta_g)$, $\Phi = 1$, and $T_{in} = 1200$ K	62
Figure 4.33 Global sensitivity analysis of the overall mechanism for 10% inlet $O_2(a^1\Delta_g)$, $\Phi = 1$, and $T_{in} = 1200$ K	64

Figure 4.34 Global sensitivity analysis of $O_2(a^1\Delta_g)$ for 10% inlet $O_2(a^1\Delta_g)$, $\Phi = 1$, and $T_{in} = 1200$ K.....	64
Figure 4.35 Local sensitivity analysis of $O_2(a^1\Delta_g)$ for 10% inlet $O_2(a^1\Delta_g)$, $\Phi = 1$, and $T_{in} = 1200$ K.....	65
Figure 4.36 Local rate of production of $O_2(a^1\Delta_g)$ for 10% inlet $O_2(a^1\Delta_g)$, $\Phi = 1$, and $T_{in} = 1200$ K.....	65
Figure 4.37 Total rate of production of $O_2(a^1\Delta_g)$ for 10% inlet $O_2(a^1\Delta_g)$, $\Phi = 1$, and $T_{in} = 1200$ K.....	66
Figure 4.38 Global sensitivity analysis of OH for 10% inlet $O_2(a^1\Delta_g)$, $\Phi = 1$, and $T_{in} = 1200$ K.....	66
Figure 4.39 Local sensitivity analysis of OH for 10% inlet $O_2(a^1\Delta_g)$, $\Phi = 1$, and $T_{in} = 1200$ K.....	68
Figure 4.40 Local rate of production of OH for 10% inlet $O_2(a^1\Delta_g)$, $\Phi = 1$, and $T_{in} = 1200$ K.....	68
Figure 4.41 Total rate of production of OH for 10% inlet $O_2(a^1\Delta_g)$, $\Phi = 1$, and $T_{in} = 1200$ K.....	69
Figure 4.42 Global sensitivity analysis of temperature for 10% inlet $O_2(a^1\Delta_g)$, $\Phi = 1$, and $T_{in} = 1200$ K.....	69
Figure 4.43 Local sensitivity analysis of temperature for 10% inlet $O_2(a^1\Delta_g)$, $\Phi = 1$, and $T_{in} = 1200$ K.....	70
Figure 4.44 Volumetric heat release rate for R17 for 10% inlet $O_2(a^1\Delta_g)$, $\Phi = 1$, and $T_{in} = 1200$ K.....	70

Figure 4.45 Total rate of production for OH and exergy destruction vs. distance for 10% inlet $O_2(a^1\Delta_g)$, $\Phi = 1$, and $T_{in} = 1200$ K.....	71
Figure 4.46 Reaction flow diagram for 25% inlet $O_2(a^1\Delta_g)$, $\Phi = 1$, and $T_{in} = 1200$ K.....	71
Figure 4.47 Mole fractions of primary species vs. distance for 25% inlet $O_2(a^1\Delta_g)$, $\Phi = 1$, and $T_{in} = 1200$ K.....	74
Figure 4.48 Mole fractions of radicals and chain carriers vs. distance for 25% inlet $O_2(a^1\Delta_g)$, $\Phi = 1$, and $T_{in} = 1200$ K.....	74
Figure 4.49 Temperature and volumetric heat release rate vs. distance for 25% inlet $O_2(a^1\Delta_g)$, $\Phi = 1$, and $T_{in} = 1200$ K.....	75
Figure 4.50 Global sensitivity analysis of the overall mechanism for 25% inlet $O_2(a^1\Delta_g)$, $\Phi = 1$, and $T_{in} = 1200$ K.....	75
Figure 4.51 Global sensitivity analysis of $O_2(a^1\Delta_g)$ for 25% inlet $O_2(a^1\Delta_g)$, $\Phi = 1$, and $T_{in} = 1200$ K.....	76
Figure 4.52 Local sensitivity analysis of $O_2(a^1\Delta_g)$ for 25% inlet $O_2(a^1\Delta_g)$, $\Phi = 1$, and $T_{in} = 1200$ K.....	76
Figure 4.53 Local rate of production of $O_2(a^1\Delta_g)$ for 25% inlet $O_2(a^1\Delta_g)$, $\Phi = 1$, and $T_{in} = 1200$ K.....	77
Figure 4.54 Total rate of production of $O_2(a^1\Delta_g)$ for 25% inlet $O_2(a^1\Delta_g)$, $\Phi = 1$, and $T_{in} = 1200$ K.....	77
Figure 4.55 Global sensitivity analysis of OH for 25% inlet $O_2(a^1\Delta_g)$, $\Phi = 1$, and $T_{in} = 1200$ K.....	78
Figure 4.56 Local sensitivity analysis of OH for 25% inlet $O_2(a^1\Delta_g)$, $\Phi = 1$, and $T_{in} = 1200$ K.....	78

Figure 4.57 Local rate of production of OH for 25% inlet $O_2(a^1\Delta_g)$, $\Phi = 1$, and $T_{in} = 1200$ K	79
Figure 4.58 Total rate of production of OH for 25% inlet $O_2(a^1\Delta_g)$, $\Phi = 1$, and $T_{in} = 1200$ K	79
Figure 4.59 Global sensitivity analysis of temperature for 25% inlet $O_2(a^1\Delta_g)$, $\Phi = 1$, and $T_{in} = 1200$ K	80
Figure 4.60 Local sensitivity analysis of temperature for 25% inlet $O_2(a^1\Delta_g)$, $\Phi = 1$, and $T_{in} = 1200$ K	81
Figure 4.61 Volumetric heat release rate for R88 for 25% inlet $O_2(a^1\Delta_g)$, $\Phi = 1$, and $T_{in} =$ 1200 K	82
Figure 4.62 Total rate of production for OH and exergy destruction vs. distance for 25% inlet $O_2(a^1\Delta_g)$, $\Phi = 1$, and $T_{in} = 1200$ K	83
Figure 4.63 Volumetric heat release rate for R17 and R88 for 25% inlet $O_2(a^1\Delta_g)$, $\Phi = 1$, and $T_{in} = 1200$ K	83
Figure 4.64 Mole fractions of OH for 0%, 5%, 10%, 50%, and 100% inlet $O_2(a^1\Delta_g)$, $\Phi =$ 1, and $T_{in} = 1200$ K	84
Figure 5.1 Exergetic efficiency of combustion vs. inlet temperature – (A) 0% inlet $O_2(a^1\Delta_g)$, (B) 5% inlet $O_2(a^1\Delta_g)$, (C) 10% inlet $O_2(a^1\Delta_g)$, (D) 15% inlet $O_2(a^1\Delta_g)$, (E) 20% inlet $O_2(a^1\Delta_g)$, (F) Statistical summary. Data in Figures 1A-1F range equivalence ratios $0.7 \leq \Phi \leq 1.3$	93
Figure 5.2 Total exergy destruction before ignition vs. inlet temperature – (A) 0% inlet $O_2(a^1\Delta_g)$, (B) 5% inlet $O_2(a^1\Delta_g)$, (C) 10% inlet $O_2(a^1\Delta_g)$, (D) 15% inlet	

<p>$O_2(a^1\Delta_g)$, (E) 20% inlet $O_2(a^1\Delta_g)$, (F) Statistical summary. Data in Figures 1A-1F range equivalence ratios $0.7 \leq \Phi \leq 1.3$</p>	94
<p>Figure 5.3 Molar conversion of H_2 vs. inlet temperature – (A) 0% inlet $O_2(a^1\Delta_g)$, (B) 5% inlet $O_2(a^1\Delta_g)$, (C) 10% inlet $O_2(a^1\Delta_g)$, (D) 15% inlet $O_2(a^1\Delta_g)$, (E) 20% inlet $O_2(a^1\Delta_g)$, (F) Statistical summary. Data in Figures 1A-1F range equivalence ratios $0.7 \leq \Phi \leq 1.3$</p>	95
<p>Figure 5.4 Exit temperature vs. inlet temperature – (A) 0% inlet $O_2(a^1\Delta_g)$, (B) 5% inlet $O_2(a^1\Delta_g)$, (C) 10% inlet $O_2(a^1\Delta_g)$, (D) 15% inlet $O_2(a^1\Delta_g)$, (E) 20% inlet $O_2(a^1\Delta_g)$, (F) Statistical summary. Data in Figures 1A-1F range equivalence ratios $0.7 \leq \Phi \leq 1.3$</p>	96
<p>Figure 5.5 Ignition temperature vs. inlet temperature – (A) 0% inlet $O_2(a^1\Delta_g)$, (B) 5% inlet $O_2(a^1\Delta_g)$, (C) 10% inlet $O_2(a^1\Delta_g)$, (D) 15% inlet $O_2(a^1\Delta_g)$, (E) 20% inlet $O_2(a^1\Delta_g)$, (F) Statistical summary. Data in Figures 1A-1F range equivalence ratios $0.7 \leq \Phi \leq 1.3$</p>	97
<p>Figure 5.6 Ignition distance vs. inlet temperature – (A) 0% inlet $O_2(a^1\Delta_g)$, (B) 5% inlet $O_2(a^1\Delta_g)$, (C) 10% inlet $O_2(a^1\Delta_g)$, (D) 15% inlet $O_2(a^1\Delta_g)$, (E) 20% inlet $O_2(a^1\Delta_g)$, (F) Statistical summary. Data in Figures 1A-1F range equivalence ratios $0.7 \leq \Phi \leq 1.3$</p>	98
<p>Figure 5.7 Exergetic efficiency vs. excess air.....</p>	100
<p>Figure 5.8 Product temperature vs. excess air</p>	101
<p>Figure 5.9 Extent of reaction vs. excess air</p>	101

NOMENCLATURE

Latin Symbols

a	First excited electronic state different multiplicity than ground state; thermodynamic curvefit coefficient
A, A	Generic atom or molecule; first excited electronic state same multiplicity as ground state; area; pre-exponential factor
Avg.	Average
B	Magnetic field vector
c	Speed of light in a vacuum
\bar{c}_p	Molar specific heat
CORR	Correlation coefficient
D	Orbital angular momentum quantum number for an atom
e	Electron
e	Elementary charge
e_d	Mass specific exergy destruction
e'_d	Mass specific exergy destruction per unit length
\dot{E}_d	Rate of exergy destruction
\dot{E}'_d	Rate of exergy destruction per unit length
e_f	Mass specific flow exergy
E, E	Exergy; electric field scalar and vector
E_a	Activation energy
f	Maxwell-Boltzmann distribution function
g	Gas phase
\bar{g}	Molar Gibbs free energy

$\Delta_r G$	Gibbs free energy of reaction
h	Mass specific enthalpy
\bar{h}	Molar enthalpy
k	Boltzmann constant, rate constant
m	Arrhenius parameter, mass
\dot{m}	Mass flow rate
M	Molecular weight
MAD	Mean average deviation
Max.	Maximum
Min.	Minimum
n	Moles
N	Number density
p, \mathbf{p}	Momentum scalar and vector
P	Pressure
Q	Generic quencher
\dot{Q}	Rate of heat transfer
\bar{R}	Universal gas constant
R	Specific gas constant
s	Mass specific entropy
\bar{s}	Molar entropy
S	Entropy
s_g	Mass specific entropy generation

s'_g	Mass specific entropy generation per unit length
\dot{S}_g	Rate of entropy generation
t	Time
T	Temperature
u, \mathbf{u}	Velocity scalar and vector
v_x	x-component of the velocity vector
V	Mixture velocity; volume
\dot{W}	Work rate
x	Mole fraction or degenerate orbital
X	Ground electronic state; concentration
y	Mass fraction or degenerate orbital
y_g	Species generation
\dot{y}_g'''	Rate of volumetric species generation
Greek Symbols	
α	Stoichiometric parameter
β	Inlet percentage of excited oxygen
Δ, Σ	Orbital angular momentum quantum number for a molecule
ε	Exergetic efficiency
η_{CoC}	Completeness of combustion
η_{MCF}	Molar conversion of fuel
ν	Stoichiometric coefficient or frequency
Φ	Equivalence ratio

π Electron orbital quantum number for a molecule

ρ Density

$\dot{\omega}$ Net rate of production

Script Symbols

h Planck constant

Superscripts

ch Chemical exergy

tm Thermomechanical exergy

o Standard state

v'_{ij} Stoichiometric coefficients for reactants

v''_{ij} Stoichiometric coefficients for products

$+/-$ Reflective symmetry; negative charge

$1, 2, 3$ Spin multiplicity

$*$ Excited electronic state or antibonding electron orbital

Subscripts

cv Control volume

cs Control surface

e Electron

f Forward reaction

g Parity

i All mechanism species; ion; species

in Control volume inlet

j Non-reference environment species in mechanism;
reaction

<i>k</i>	Reference environment species in mechanism
<i>mix</i>	Mixture
<i>out</i>	Control volume outlet
<i>ox</i>	Oxidizer
<i>prod</i>	Product
<i>r</i>	Reverse reaction
<i>react</i>	Reactant
<i>ref</i>	Reference state for property evaluation
<i>st</i>	Stoichiometric
0	State of the exergy reference environment; initial state

CHAPTER 1 INTRODUCTION

1.1 Motivation

The International Energy Outlook 2011 (IEO2011) [1] predicts there will be a 53% increase in world energy consumption from 2008 to 2035 (Figure 1.1). The primary contributing factors are improved global economic prosperity and population growth. The IEO2011 also

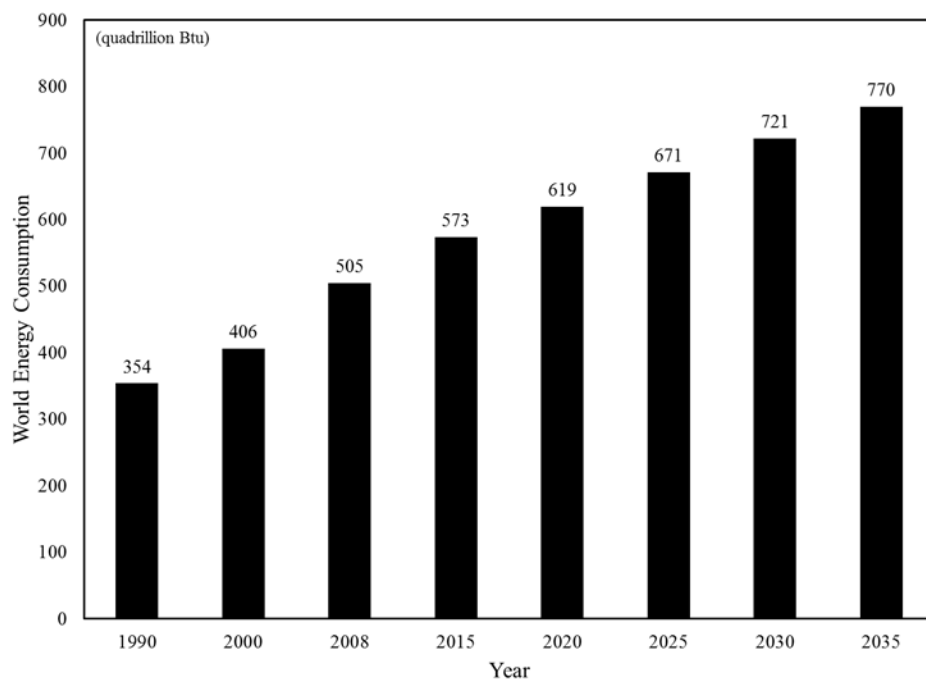


Figure 1.1 World energy consumption [1]

provides historic and projected data regarding the types of fuels that will be used to supply the energy consumption forecast, shown in Figure 1.2 [1]. Although energy supplied by renewable sources is increasing, for the foreseeable future non-renewables constitute the overwhelming majority of the world's energy resource portfolio. The top three fuels: liquids¹, coal, and natural gas are all fossil fuels. The principal method for liberating the chemical energy contained in

¹ Liquids are defined as petroleum based fuels and their derivatives (e.g. kerosene, gasoline, etc.)

these fuels is combustion. Fossil fuels are expected to constitute approximately 80% of the energy resources required to fulfill the projected global demand.

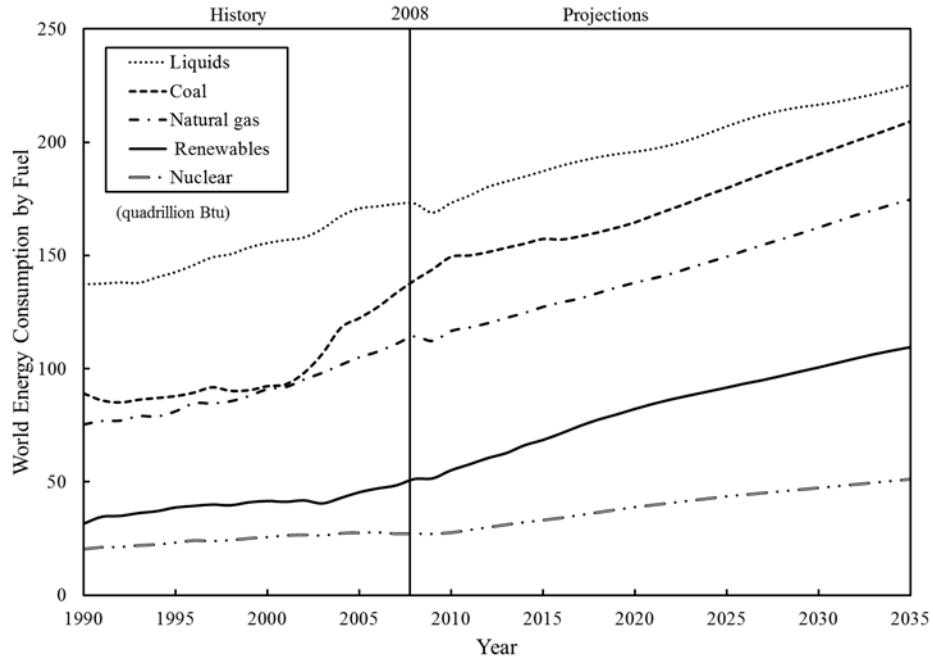


Figure 1.2 World energy consumption by fuel [1]

Amid increased demand driven by the rapid development of emerging economies and population growth, coupled with limited non-renewable energy reserves, the development of more efficient combustion devices is of the utmost importance. Due to the complex nature of combustion, bringing such technologies to fruition requires a multipronged approach to research and development, as well as a synergetic relationship between scientists and engineers from various fields of knowledge to confront these issues.

1.2 Objective

The introduction of electronically excited oxygen into the combustion process has been shown to reduce ignition delay, improve flame stability, and increase flammability limits [3]. By understanding how the presence of excited oxygen alters the chemical kinetics of oxidation, it

may be possible to reduce the irreversibility of combustion thereby reducing fuel use to achieve desired energy conversion. To accomplish this requires that three fundamental objectives be met. First, construction of an appropriate model from first principles that successfully isolates the irreversibility associated with chemical reaction from all other sources of irreversibility generated during combustion. Second, conducting a detailed exergy analysis of the system; this requires developing a method for calculating the chemical exergy of electronically excited species. Third, carrying out a parametric study to ascertain what influences varying the inlet concentration of electronically excited oxygen and other traditional combustion parameters have on the irreversibility of chemical reaction.

1.3 Methodology

To achieve the defined objectives, a plug flow reactor (PFR) model was developed using the chemical simulation software CHEMKIN-PRO[®] [4] in conjunction with the Moscow State University mechanism [3, 5]. The Moscow State University mechanism is a hydrogen-oxygen oxidation mechanism that includes explicit reaction pathways for electronically excited atomic and molecular oxygen, as well as hydroxyl. The second objective was accomplished by using the output variables from the chemical simulation to perform a detailed exergy analysis of the system. Two cases were considered. The first was a base case which did not include excited oxygen in the inlet composition of reactants. The second was an extended case composed of a series of model runs with increasing concentrations of excited oxygen in the charge, while maintaining a stoichiometric fuel-oxidizer ratio. Finally, a parametric study was conducted. The combustion parameters considered in addition to the inlet concentration of excited oxygen were inlet temperature and equivalence ratio (Figure 1.3).

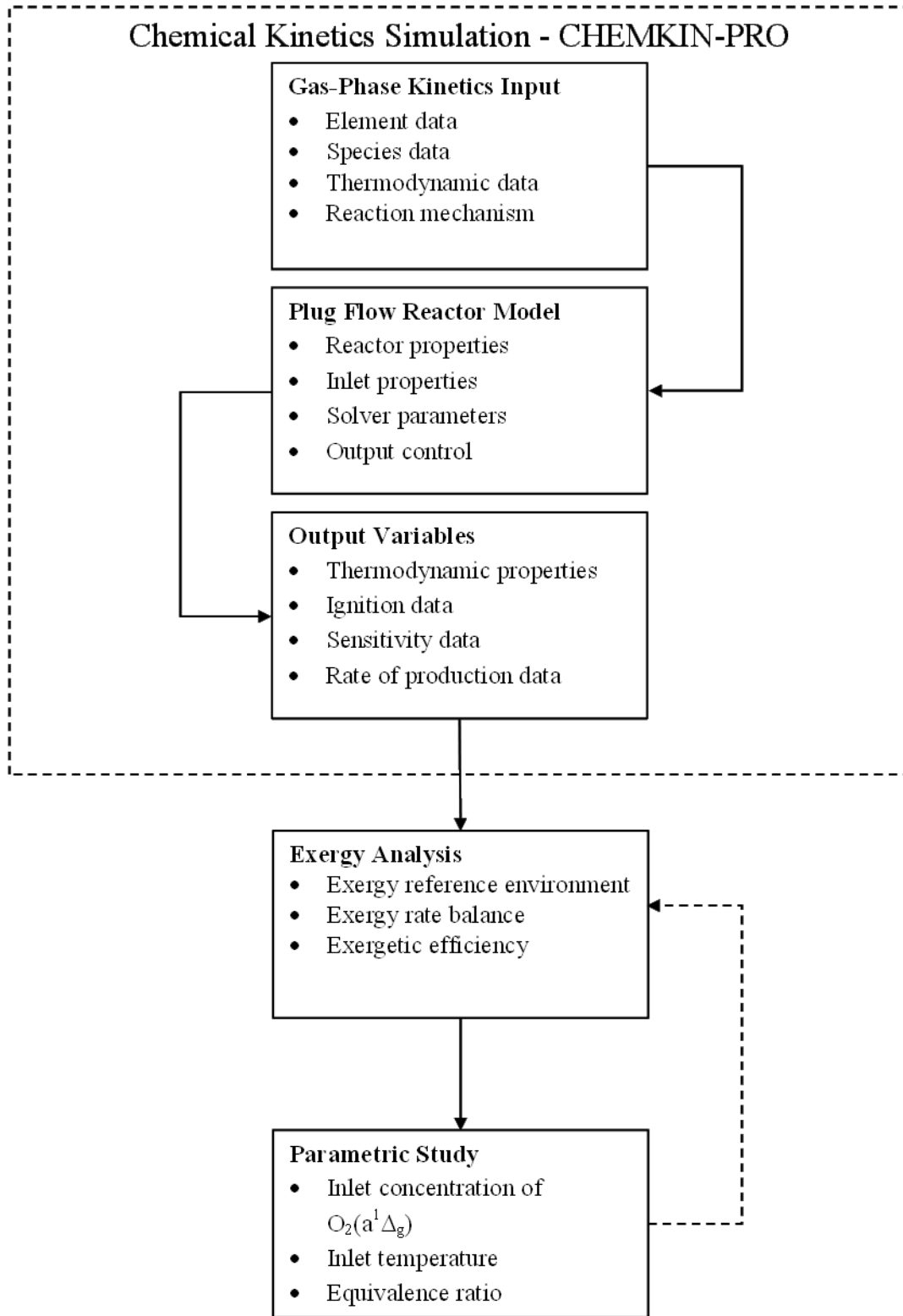


Figure 1.3 Method of approach

1.4 Literature Review

Combustion research has progressed significantly over the past several years [6]. Combustion is a confluence of several complex physical phenomena requiring the collective effort of a wide variety of researchers from many fields of study. One area that has received a considerable amount of attention is the enhancement of combustion efficiency. Two particular

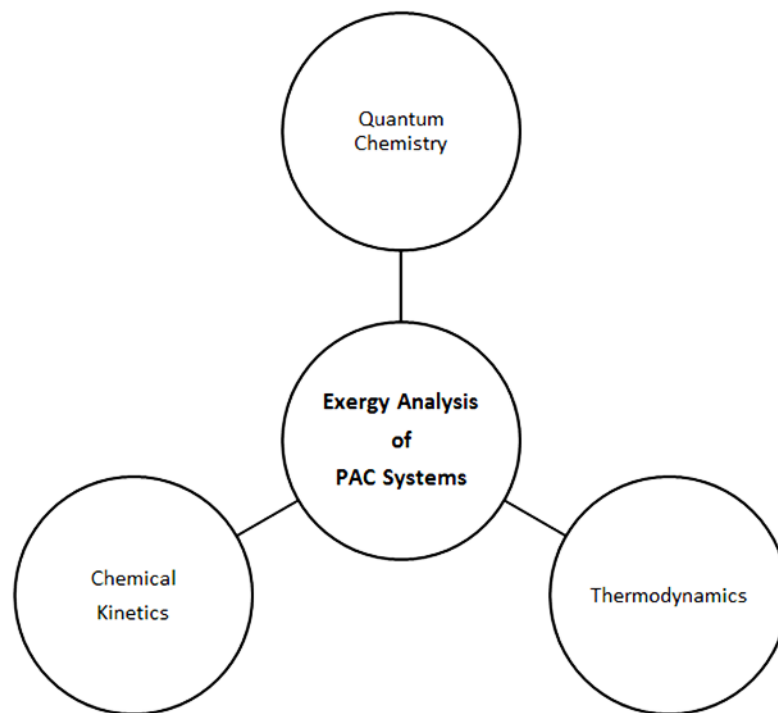


Figure 1.4 Constituent disciplines for exergy analysis of PAC system

avenues of research pursued to address this are exergy analysis and plasma-assisted combustion (PAC). Exergy analysis focuses on the effective utilization of resources and efficient design of thermal systems [7]. PAC is centered on the use of plasma to improve ignition, and enhance combustion stability and control [8]. Until now these fields of research have been pursued separately. This research project applies the analytical power of exergy analysis to PAC systems. Relevant literature from both fields of study are presented providing insight into

opportunities where the coupling of these two tracks of research can significantly advance the goal of achieving more efficient combustion.

1.4.1 Exergy Analysis

1.4.1.1 A Brief History

Exergy is defined as the maximum theoretical useful work obtained if a system is brought into complete thermodynamic equilibrium with the environment [7, 9]. The conceptual development of exergy began with Carnot in 1824. However, it was Gibbs in 1873 that first derived an explicit thermodynamic function for available work. It took approximately another thirty-five years before Jouget introduced the concept of dissipated work, or in today's terminology *exergy destruction*. In 1949, in what is considered by many to be a seminal paper, Obert and Birnie applied the concept of exergy analysis to a 60 MW fossil fueled power plant, identifying and rank-ordering losses and irreversibilities [10].

1.4.1.2 Applications of Exergy Analysis

A comprehensive review conducted by Rakopoulos and Giakoumis [11], regarding exergy analysis of internal combustion (IC) engines, shows that in IC engines combustion irreversibility is responsible for the destruction of approximately 21% of the available fuel exergy [12-14]. Kaushik *et al.* [15] conducted an inclusive review on exergy analysis of thermal power plants (TPP) that indicates combustion irreversibility accounts for the destruction of 35% of the fuel exergy. Work carried out by Turgut *et al.* [16] demonstrated that combustion irreversibility in turbofan aircraft engines destroys nearly 33% of the fuel exergy. Clearly irreversible combustion is responsible for a large portion of the exergy destruction that occurs in

energy conversion systems involving chemical reaction; its reduction is the primary focus of this study.

1.4.1.3 Modes of Combustion Irreversibility

The work of Dunbar and Lior identified the major sources of irreversibility in energy conversion systems involving combustion [2]. In addition, Dunbar and Lior go a step further by applying exergy analysis explicitly to the combustion process with the express goal of dissecting the specific modes of combustion irreversibility. As shown in Figure 1.5, the results of their work indicates that for the fuel exergy destroyed there are three primary modes of irreversibility which occur during combustion: (1) internal heat transfer, (2) diffusion and oxidation, and (3)

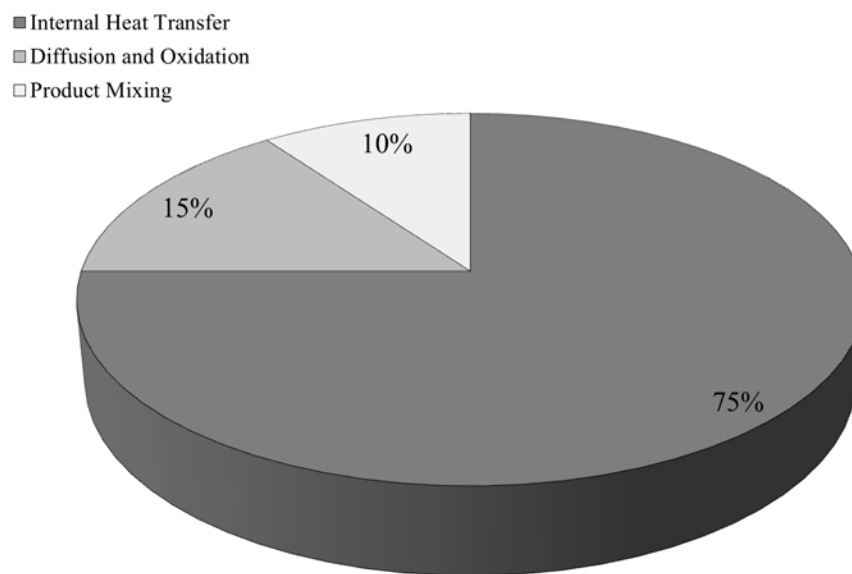


Figure 1.5 Modes of combustion irreversibility [2]

product mixing.

Internal heat transfer refers to thermal energy exchange between hot products and cooler reactants, which constitutes the vast majority of the irreversibility that evolves during

combustion. Several groups have proposed theoretical methods for minimizing irreversibility due to internal heat transfer [17-19]. The concept is termed near-equilibrium combustion and focuses on the controlled heating of reactants; in the limiting case if the reactants were heated to the product temperature equilibrium combustion would result. The irreversibility corresponding to diffusion lends itself to mixing at the molecular level due to the random motion of atoms and molecules and acts to increase the randomness of a system. Mixing is a transport mechanism which acts to increase the randomness of the system through bulk motion [20]. There is a large body of research which addresses irreversibility due to both diffusion and mixing. However, to preserve the continuity of the discussion at hand the author leaves the pursuit of this information to the reader. Finally, regarding irreversibility due to oxidation there is very little literature which exclusively addresses this in detail. Although oxidation is a relatively small amount of the overall combustion irreversibility there are still gains to be had from its reduction. More importantly the pursuit of this line of research advances the application of exergy analysis and targets contributions to its destruction at a more fundamental level, as well as furthering the objective of designing hyper-efficient combustion apparatus. Irreversibility due to oxidation, from the perspective of advanced exergy analysis, would have previously been considered an unavoidable endogenous form of exergy destruction. In other words a source of irreversibility that is integral to a system component or process, and due to technological limitations is inevitable [21, 22]. However, with the advent of PAC an opportunity is presented to optimize combustion in ways not previously possible.

1.4.2 Plasma-Assisted Combustion

1.4.2.1 *A Brief History*

In 1600, Gilbert was the first person to detect an electric charge associated with a flame [23] by using an electroscope². Brande's work, published in 1814, was the first series of detailed experiments carried out regarding the influence of an electric field on flame behavior [24]. The 1950s and 60s, research regarding electrical aspects of combustion increased greatly. Much of the research was centered on identifying generation mechanisms and the detection of ionic species in flames. By the 1970s and 80s, research progressed to the point that electric fields were being used to enhance flame stability and increase flammability limits. In the 1990s, work was directed toward the reduction of the emission of NO_x [25-27]. The vast majority of the aforementioned work utilized thermal plasmas (TP). Currently, the state-of-the-art plasma research takes advantage of nonthermal plasmas (NTP) which possess properties that are uniquely suited to enhance ignition and combustion stability in high performance propulsion systems [28].

1.4.2.2 *Applications of Plasma-Assisted Combustion*

The automotive industry is currently exploring several types of engine designs to reduce fuel consumption; the gasoline direct injection (GDI) engine is one such design. GDI engines use the quantity of injected fuel to control engine load as opposed to throttling intake air, which is the typical method used in standard spark-ignition (SI) engines. At low loads the charge is so lean that traditional spark plug technology is not capable of initiating combustion. However, spark plasma technologies capable of reliable and stable ignition in lean high-pressure (15-40 atm) combustion environments are in the early stages of development [8, 29].

² A scientific instrument used to detect the presence and magnitude of electric charge.

Hypersonic aviation has long been pursued by the aerospace industry. The design and development of ram and scramjet technologies have encountered formidable technical challenges pertaining to ultra-fast low pressure (0.1 atm) combustion environments. One such issue is the shock wave interaction with the influent air which results in dissociation and ionization reducing engine efficiency; one of the primary parameters for scramjet engine efficiency is completeness of combustion. NTPs show great promise with regard to offering a means by which stable combustion can be achieved for high altitude ultra-fast situations; thereby expanding the region of efficient, stable engine operation [8, 29].

In the electric power generation industry the use of plasma technologies are in the initial stages of development; they are generally referred to as plasma-fuel systems (PFS). The primary objective of PFS is to reduce the use of fuel oils and natural gas for the startup of coal-fired TPP, as well as facilitating efficient combustion of low-ranked coals and decreasing the emissions of SO_x and NO_x [30, 31]. It works by segregating a fraction of the influent coal-air charge and subjecting it to a plasma flame, which in turn gasifies the coal and produces partially oxidized char carbon. This yields an oxygen deficient charge resulting in a highly reactive fuel (HRF), when introduced back into the furnace promotes ignition and stable combustion [32]. In addition to computational work, Karpenko *et al.* [33] carried out experiential testing on 27 boilers using several types of coals. The results of the testing showed that when PFS were used there was a twofold reduction in NO_x emission and unburned carbon was reduced by a factor of four.

1.4.2.3 Plasma-Assisted Combustion Technologies

Currently, several plasma technologies are either already well-established or are well into the proof of concept phase of development. Four of those technologies will be presented here: (1) plasma pilot burners, (2) plasma fuel nozzles, (3) plasma torches, and (4) plasma combustors.

Plasma pilot burners are ignition and flame control devices which are designed for long term

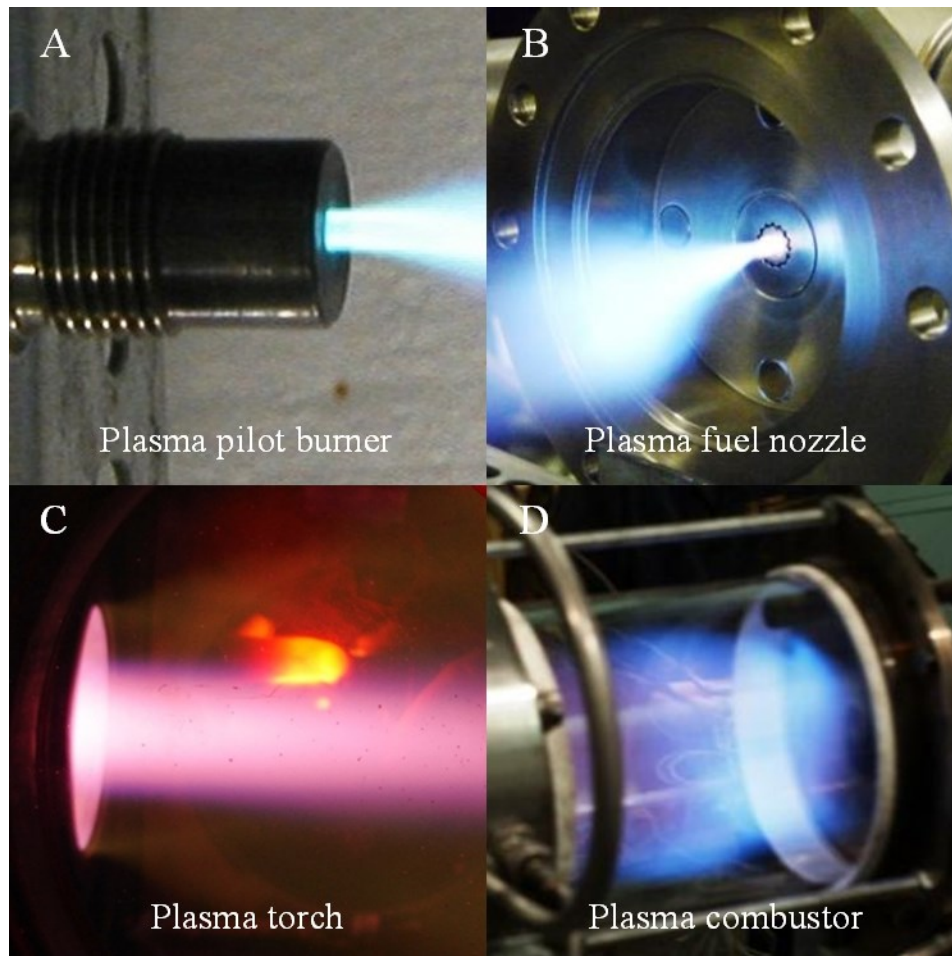


Figure 1.6.A-D Plasma-assisted combustion technologies [34]

continuous operation. The one displayed in Figure 1.6.A [34] functions by emitting a high speed plume of active NTP into the charge. It can operate in flow conditions ranging from a few meters per second to supersonic Mach numbers, pressures up to 3 MPa, and temperatures as high 1070 K. Additionally, it can sustain a stable flame under super-lean operating conditions [34].

Plasma fuel nozzles are combination plasma generators and fuel atomizers, which provide simultaneous fuel atomization, ignition, and flame control in one unit. The unit displayed in Figure 1.6.B [34] is designed for continuous operation while providing super-fine fuel

atomization, as well as low power ignition, partial oxidation, and continuous flame control. In addition to holding the primary fuel, it is capable of processing two additional fuels simultaneously, including solid fuels. It can operate over all ranges of ambient conditions including high altitudes. This device can generate both TPs and NTPs [28, 34].

The primary functions of a continuous operation plasma torch are flame stabilization to increase the mass flow of fuel in lean-burn regimes, as well as reduce soot and NO_x . This is accomplished by using plasma to heat the gas stream to very high temperatures, above that which is seen in the typical combustion environment [28]. The unit depicted in Figure 1.6.C [34] is used for ignition, combustion, waste processing, coal gasification, and fuel reformation applications. It uses NTPs and operates at temperatures up to 10270 K. The output velocity of the plasma ranges from 20 m/s to 1000 m/s.

Plasma combustors are primarily intended for gaseous-fuels and use NTPs. Their primary function is to improve fuel efficiency and reduce CO_2 emissions. Figure 1.6.D [34] is a plasma-assisted tornado combustor. These types of plasma combustors incorporate the use of vortexes, which concentrates the flow toward the center of the reactor insulating the plasma from the walls and allowing it to heat the gases to much higher temperatures [28].

CHAPTER 2 NONTHERMAL PLASMA

2.1 Classifications of Plasma

The term plasma was first used in connection with electric discharge in gases by Nobel laureate Irving Langmuir in 1923 [35]. Generally, plasma is defined as an ionized gas composed of positively and negatively charged particles. Due to its unique properties and overwhelming

abundance in the universe³, plasma is considered to be the fourth state of matter [36]. However, this definition is not adequate enough to describe in totality all the states of plasma [37].

In the literature plasma is classified several different ways based on the nature of the respective research. Care must be given as to the language used for its description, which should also be accompanied by proper context of the associated physical processes surrounding its state and method of generation. Common vernacular used is “hot” (thermal) or “cold” (nonthermal) plasma [28]. Depending on the method of generation or physical phenomena, “hot” is typically understood to mean temperatures greater than 10^4 K, which generally implies there is sufficient energy to initiate ionization. The term “cold” plasma refers to processes where production occurs at temperatures around 10^2 K, and the fraction of ionized molecules is significantly smaller than for hot plasma [37, 38].

2.1.1 Thermal Plasma

In PAC literature, the term TP usually implies that the plasma is in thermal equilibrium [28]. In general this is not necessarily the case, as there can be both equilibrium and nonequilibrium, as well as thermal and nonthermal plasmas [36]. For simplicity and conformity with terminology in the literature, in these discussions TP implies that the plasma is in thermal equilibrium and generated at elevated temperatures.

Temperature (T) generally refers to the bulk temperature of the plasma. However, as mentioned previously, plasmas are composed of positively and negatively charged particles: electrons and ions. The presence of neutral particles is also common, but for this discussion not addressed here. At a specific state related to the production process, each category of particle

³ It is estimated that as much as 99% of the visible matter in the universe is in a plasma state (e.g. stars, etc.)

possesses a certain average kinetic energy and hence temperature: electron temperature (T_e) and ion temperature (T_i). The relative difference between these temperatures is what defines whether or not the plasma is in thermal equilibrium. Strict thermal equilibrium is defined as $T \equiv T_e \equiv T_i$. This implies that the Maxwell-Boltzmann distribution can be expressed in terms of the bulk plasma temperature [36, 37].

$$f(p) = \frac{N}{(2\pi mkT)^{3/2}} \exp\left(-\frac{p^2}{2mkT}\right) \quad (2.1)$$

A corollary of this is that the bulk plasma temperature characterizes the average kinetic energy.

$$\frac{3}{2}kT = \frac{1}{2}m\langle u^2 \rangle \quad (2.2)$$

2.1.2 Nonthermal Plasma

In the case of NTP, the electron temperature is significantly greater than either the bulk plasma temperature or ion temperature $T \approx T_i \ll T_e$ [36]. The degree to which the electron temperature differs is a strong function of the process used to generate the plasma. For example, (Equation 2.3) in the case of electric discharge where an electric field is used to accelerate electrons, if the temporal and spatial characteristics of the field are sufficiently larger than the mean free path and collisional frequency, the result will be a non-Maxwellian energy distribution; hence the definition of a nonequilibrium plasma state. Inelastic collisions occurring



between the electrons and other particles in the gas result in transfer of energy. Since the

electron mass is much less than the masses of the other gas particles, the momentum transferred excites their rotational, vibrational, and electronic states [39, 40]

For comparison to Equation 2.1, the distribution function for a charged particle in a strong constant electric field is presented. Here it is assumed that the plasma is stationary and that the electric field \mathbf{E}_0 and magnetic field \mathbf{B}_0 are parallel. Restricting the discussion to electrons, the relationship between momentum and time is given by Equation 2.4. For $t < \nu_e^{-1}$ where ν_e is the electron collisional frequency, Equation 2.4 suggests that all electrons are accelerated by the

$$\mathbf{p}_0(t) = \frac{m_e \mathbf{u}_e}{\sqrt{1 - u_e^2/c^2}} = e_e \mathbf{E}_0 t \quad (2.4)$$

field and ions are held fixed. Assuming the electrons possessed equilibrium Maxwellian distribution before engaging the electric field, the momentum distribution function is given by Equation 2.5 [37]. This simplified case is also presented since much of the PAC literature cited

$$f_0(\mathbf{p}, t) = \frac{N_e}{(2\pi m T_e)^{3/2}} \exp\left(-\frac{[\mathbf{p} - \mathbf{p}_0(t)]^2}{2m T_e}\right) \quad (2.5)$$

in this study presents empirical and numerical data for NTP generated using pulsed DC discharge [41-43].

2.2 Nonthermal Plasma Generation

The generation of NTPs can be divided into two primary categories, production using electric fields or beams. Methods of production using electric fields include: continuous DC discharge, pulsed DC discharge, radio frequency (RF) discharge, microwave (MW) discharge,

and dielectric barrier discharge⁴ (DBD). Plasma generation employing beams is usually accomplished by using either electron or laser beams [44]. Although there is a significant amount of literature pertaining to NTPs generated using beams and their use in combustion applications, the focus here are those produce by pulsed DC discharge.

2.2.1 NTP Generation Using Electric Fields

The reduced electric field E/N , which is the ratio of the magnitude (i.e. strength) of the electric field to the number density of the gas, is an important parameter for NTPs generated using electric discharge. Its value dictates the energy distribution in the discharge and as a result the composition of active particles [40]. Figure 2.1 [29] illustrates the relationship between the types of NTPs generated to the reduced electric field. Additionally, it provides insight into their various applications.

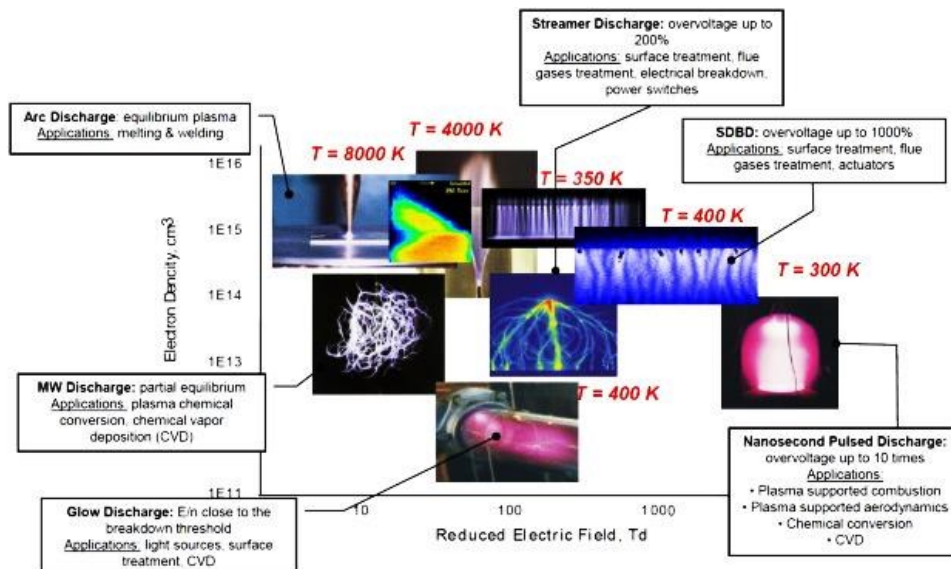


Figure 2.1 Categories of NTPs as a function of reduced electric field [29]

⁴ Sometimes referred to as silent dielectric barrier discharge (SDBD)

2.2.2 Electronic Excitation and Structure of Molecular Oxygen

In gases for E/N values ranging from 100 - 500 Td⁵, the primary mode of excitation is electronic. However, the transition of molecular oxygen from its first electronically excited state to its ground state (Equation 2.6) has a much lower excitation threshold, ranging from 3 - 10 Td.



At pressures around 1 atm the excited state $\text{O}_2(a^1\Delta_g)$ has a relatively long radiative half-life of approximately 45 minutes. This is attributed to the fact that this transition is doubly forbidden [45]. The selection rules governing transitions for diatomic molecules dictate that the transition undergone by the orbital angular momentum quantum number $\Delta - \Sigma$ and the change in parity $g - g$ are both forbidden. Here, forbidden does not suggest that the transition cannot occur, but

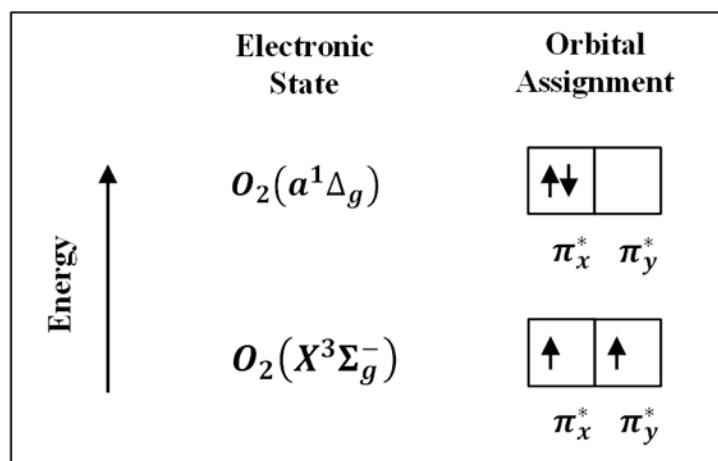


Figure 2.2 Molecular orbital diagram of oxygen [47]

that quantum mechanically it is highly improbable [46].

Figure 2.2 is a simplified representation [47] of the electron configuration of the valence electrons for molecular oxygen. Although the true description of the electronic state is more

⁵ 1 Td (Townsend) = 10^{-21} V/m²

complex than what is depicted here, the diagram provides some insight regarding what the implications are regarding the transition which occurs during plasma generation. Triplet oxygen $O_2(X^3\Sigma_g^-)$ is relatively unreactive. If it attempts to oxidize another molecule its electron configuration requires that both electrons have antiparallel spin, reducing its oxidizing potential. However, this spin restriction is lifted for singlet oxygen which significantly increases its oxidizing potential [48]. This property is an important characteristic and integral to the remainder of the discussion.

CHAPTER 3 CHEMICAL SIMULATION

This project was executed in two phases. Phase I consisted of conducting a single-parameter parametric study, which consisted of varying the amount of singlet oxygen included in the charge, while holding all other parameters fixed, and then analyzing the effects of varying the charge on trends in exergy destruction. This was accomplished by developing two numeric plug flow reactor models using the chemical simulation tool CHEMKIN-PRO[®]. Model IA, no excited oxygen was added to the inlet charge which served as the baseline. Model IB consisted of a series of extended model runs where singlet oxygen was added to the inlet charge in increasing amounts until it composed 100% of the oxidizer. Both models were subjected to identical inlet conditions.

Phase II consisted of conducting a multi-parameter parametric study where in addition to varying the percentage of excited oxygen in the charge, inlet temperature, equivalence ratio, and diluent type were also varied. A detailed exergy analysis was conducted on the results.

In order to address the goal of understanding how NTP affects trends in exergy destruction due to chemical reaction, the selected model must possess the capability of isolating the

phenomena. The plug flow reactor model served the purposes of this study very well. Invoking the appropriate assumptions the resulting governing equations allow for the isolation of oxidation, which will be demonstrated in subsequent subsections. Additionally, for any thorough analysis of a reacting system, where the interest of study is centered on rate drive phenomena, a detailed understanding of the chemical kinetics is required. Two well utilized methods that were used for this purpose are sensitivity analysis and reaction flow analysis [49, 50].

3.1 Gas-Phase Kinetics

3.1.1 Mechanism Description

In order to facilitate modeling, specific information regarding the species, their thermodynamic properties, and the chemical reaction mechanism must be provided. The mechanism and corresponding rate constants used for this model were developed by Moscow

Table 3.1 Moscow State University mechanism species [3, 5]

Species	Term Symbol	Electron Pairing
Argon, Ar (g)	1S_0	Non-Radical
Hydrogen, H (g)	$^2S_{1/2}$	Radical
Hydrogen, H ₂ (g)	$X^1\Sigma_g^+$	Non-Radical
Hydroperoxyl, HO ₂ (g)	X^2A''	Radical
Hydrogen Peroxide, H ₂ O ₂ (g)	X^1A	Non-Radical
Hydroxyl, OH (g)	$X^2\Pi$	Radical
Hydroxyl, OH (g)*	$A^2\Sigma^+$	Radical
Nitrogen, N ₂ (g)	$X^1\Sigma_g^+$	Non-Radical
Oxygen, O (g)	3P_2	Radical
Oxygen, O (g)*	1D_2	Non-Radical
Oxygen, O ₂ (g)	$X^3\Sigma_g^-$	Radical
Oxygen, O ₂ (g)*	$a^1\Delta_g$	Non-Radical
Ozone, O ₃ (g)	X^1A_1	Non-Radical
Water, H ₂ O (g)	X^1A_1	Non-Radical

* First electronically excited state

State University in conjunction with the European Union (INTAS 03-51-4736) [3, 5]. The mechanism includes fifteen species; twelve active and three inert. For this model, fourteen species were considered; twelve active and two inert. The mechanism is composed of 142 elementary reactions, including explicit reaction pathways for electronically excited species. The rate constants are expressed in terms of the generalized Arrhenius law (Equation 3.1).

$$k = AT^m \exp(-E_a/\bar{R}T) \quad (3.1)$$

3.1.2 Selection of Inert Diluent Species

In the work conducted by Bourig *et al.* [3] on the numeric modeling of hydrogen-oxygen flames involving electronically excited species, a considerable amount of work was done validating the Moscow State University mechanism against empirical data from the literature. Comparisons were made of laminar flame speed, influence of dilution on laminar flame speed, and ignition delay; which were all in good agreement with experiment. The generation of NTP

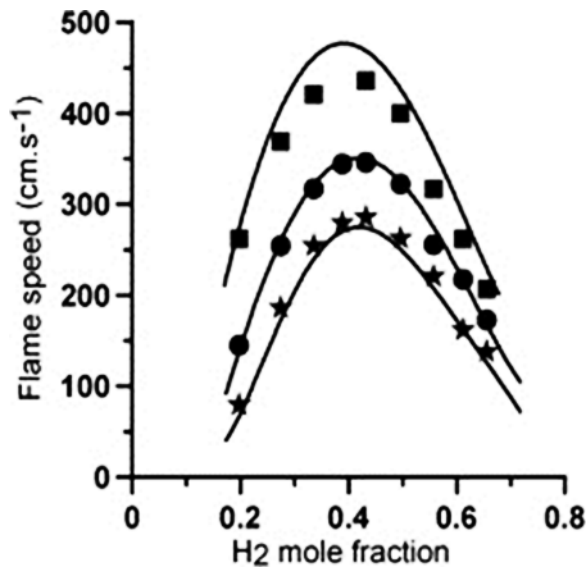


Figure 3.1 Influence of dilution on laminar flame speed validation results, for atmospheric H₂-O₂ flames diluted with: (★) N₂, (●) Ar, (■) He (ratio O₂:N₂ = O₂:Ar = O₂:He = 1:3.76). Line MSU model, symbols empirical data [3]

by pulsed DC discharge always occurs in the presence of diluents [3, 41]. The validation results displayed in Figure 3.1 [3] indicate argon produced the most accurate results over the range of hydrogen mole fractions considered, which coincides with the range explored in this study. Nitrogen produced the next most accurate results. Therefore, argon and nitrogen were selected as the diluents of choice. Due to its accuracy, argon was selected for the Phase I analysis, and both were considered in Phase II of the study. Phase II the case of no dilution was also included as a limiting case.

3.1.3 Thermodynamic Data

The thermodynamic properties for the various species are represented using polynomials. All species are treated as ideal gases, and gas mixtures are assumed to be ideal gases as well. NASA has published a comprehensive listing of the JANAF polynomial curvefit coefficients for several species [51, 52] which is included the thermodynamic properties database in CHEMKIN-PRO[®] [4]. For the excited species the curvefit coefficients were obtained from literature⁶ [3, 53, 54].

The polynomial representations for the thermodynamic properties enthalpy and entropy are given in Equations 3.2 and 3.3 [53, 55].

$$\frac{\bar{h}_i^o}{RT} = \left[a_1 + \frac{a_2}{2}T + \frac{a_3}{3}T^2 + \frac{a_4}{4}T^3 + \frac{a_5}{5}T^4 + \frac{a_6}{T} \right]_i \quad (3.2)$$

$$\frac{\bar{s}_i^o}{RT} = \left[a_1 \ln(T) + a_2T + \frac{a_3}{2}T^2 + \frac{a_4}{3}T^3 + \frac{a_5}{4}T^4 + a_7 \right]_i \quad (3.3)$$

⁶ Reference Appendix B for curvefit coefficients used

The actual property functions are given in Equations 3.4 and 3.5 [7, 53, 55]. For an ideal gas enthalpy is a function of temperature only; however, entropy is a function of both pressure and temperature.

$$\bar{h}_i^o = \bar{h}_{f,i}^o + \int_{T_{ref}}^T \bar{c}_{p,i} dT \quad (3.4)$$

$$\bar{s}_i^o = \bar{s}_{f,i}^o + \int_{T_{ref}}^T \frac{\bar{c}_{p,i}}{T} dT \quad (3.5)$$

This implies that the information contained in Equation 3.3 only provides the temperature component of entropy change.

$$\bar{s}_i^o = \bar{s}_{f,i}^o + \int_{T_{ref}}^T \bar{c}_{p,i} \frac{dT}{T} - \bar{R} \int_{P_{ref}}^{P_i} \frac{dP}{P} \quad (3.6)$$

The pressure component of entropy change was calculated using Equation 3.6 along with the thermodynamic model output variables from CHEMKIN-PRO[®] [4].

3.2 Plug Flow Reactor Model

3.2.1 Assumptions

The following assumptions were applied: (1) adiabatic, (2) no boundary work, (3) steady-state, (4) one-dimensional flow, (5) frictionless flow, (6) constant cross-sectional area, (7) ideal gas behavior, (8) no surface reactions, (9) stoichiometric fuel-oxidizer ratio, and (10) premixed charge. These assumptions lead to a set of governing equations which allow the irreversibility of chemical reaction to be isolated and studied. The assumptions were selected to ensure that

oxidation was the only rate driven process, which will be clear from the resulting governing equations for the model [56-58].

3.2.2 Governing Equations

The rate balances (Equations 3.7 - 3.10) take the following form when applying the assumptions and dividing the appropriate terms by the mass flow rate [20, 55].

Mass Rate Balance

$$\frac{d(\rho v_x)}{dx} = 0 \quad (3.7)$$

Momentum Rate Balance (x-component)

$$\frac{dP}{dx} + \rho v_x \frac{dv_x}{dx} = 0 \quad (3.8)$$

Energy Rate Balance

$$\frac{dh}{dx} + v_x \frac{dv_x}{dx} = 0 \quad (3.9)$$

Species Rate Balance

$$\frac{dy_i}{dx} - y_{g,i} = 0 \quad (3.10)$$

Equation of State

$$P = \frac{\rho \bar{R} T}{M_{mix}} \quad (3.11)$$

In Figure 3.2 the rate balances are applied to a differential plug. Based on the

$$y_{g,i} = \frac{\dot{\omega}_i M_i}{\rho v_x} \quad (3.12)$$

assumptions selected, the only rate driven process which appears in the control volume is the volumetric species generation term. Examining this term closer more insight can be gained into

$$\dot{\omega}_i = \sum_j v_{ij} \left(k_{fj} \prod_i [X_i]^{v'_{ij}} - k_{rj} \prod_i [X_i]^{v''_{ij}} \right) \quad (3.13)$$

its specific nature. In Equation 3.12, lowercase omega represents the net production rate (Equation 3.13) of the *i*th species. It contains the rate constants from each elementary reaction in

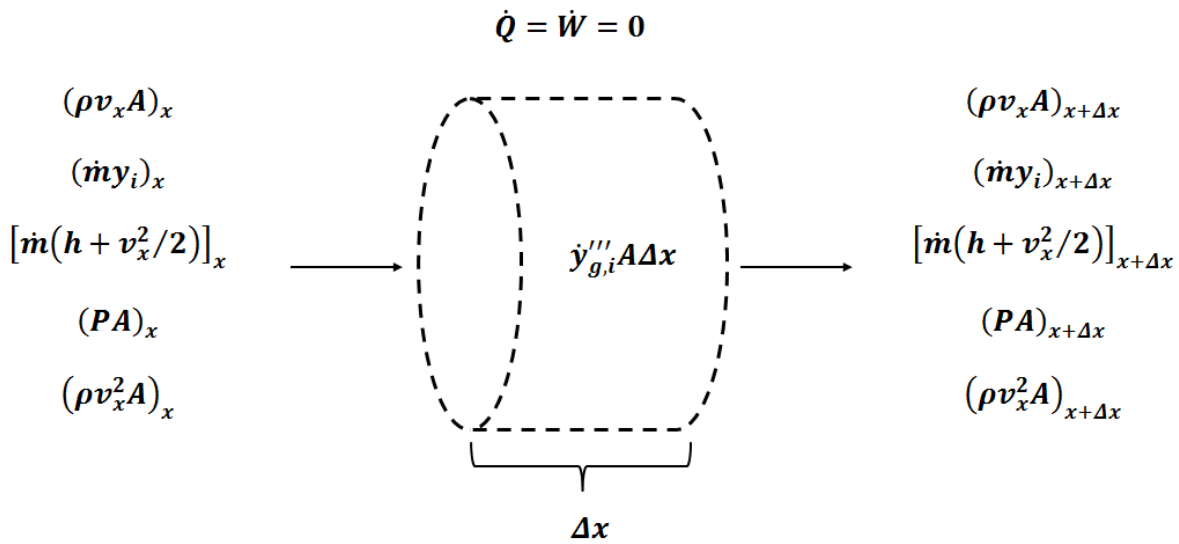


Figure 3.2 Rate balances for a differential plug

the mechanism that contribute to the consumption or formation of the *i*th species, as well as the respective stoichiometric coefficients from the corresponding reactions.

3.2.3 Inlet Conditions

Table 3.2 [59] presents the inlet conditions for the Phase I portion of the study. For Model IA: $\alpha = 0.5$, which implies there is 0% excited oxygen in the inlet charge. Model 1B is composed of a set of extended model runs. The defined functional relationship between triplet and singlet oxygen is such that when α is decreased by increments of 0.025, it increases the

amount of excited oxygen in the charge by 5% while reducing the ground state oxygen by the same amount maintaining a stoichiometric fuel-oxidizer ratio. When $\alpha = 0$, the oxidizer in the

Table 3.2 Inlet conditions for Phase I, Model IA and Model IB [59]

Thermodynamic Properties	
<i>Property</i>	<i>Magnitude</i>
Pressure	1 atm
Temperature	1200 K
Charge Composition	
<i>Fuel-Oxidizer</i>	<i>Stoichiometric Coefficient</i>
H ₂	1
$\alpha(\text{O}_2 + 3.76\text{Ar})$ $(0.5 - \alpha)[\text{O}_2(a^1\Delta_g) + 3.76\text{Ar}]$	$0 \leq \alpha \leq 0.5; \Delta\alpha = 0.025$

inlet charge is 100% singlet oxygen.

The combustion parameters for the Phase II multi-parameter parametric study are itemized in Table 3.3. In addition to the parameter listings, the ranges for each parameter are shown as well as the increments by which they were varied. The selected inlet temperature range is within the limit of work that has been reported in the literature for this mechanism [3]. The pressure was held fixed because the reaction rates are accurate for pressures up to 1 atm [3, 5]. Data from a few hyper-extended model runs, where the charge was either extremely fuel rich or lean, provide no new insight for the objectives of this study. The range of equivalence ratios

Table 3.3 Combustion parameters for Phase II parametric study

Parameter	Range
Inlet temperature	$1100 \text{ K} \leq T \leq 1300 \text{ K}, \Delta T = 50\text{K}$
Inlet pressure	1 atm (fixed)
Equivalence ratio	$0.7 \leq \Phi \leq 1.3, \Delta\Phi = 0.15$
Inlet percentage of O ₂ (a ¹ Δ _g)	$0\% \leq \beta \leq 20\%, \Delta\beta = 5\%$
Inert diluent species	No dilution, argon, nitrogen

selected covers common practical combustion operating conditions.

3.3 Post Processing Algorithm

In order to perform the exergy analysis, the thermodynamic output variables required post-processing. This was accomplished by an Excel based algorithm developed by the author. The computed output variables include: (1) species enthalpy, (2) species entropy, (3) mixture entropy, (4) entropy generation, (7) exergy, (8) chemical exergy (8) thermomechanical flow exergy, (9) chemical flow exergy, (10) total mixture flow exergy, (11) exergy destruction, (12) exergetic efficiency, and (13) completeness of combustion. All output variables were verified to a high degree of accuracy. The corresponding governing equations for variables (3) - (13) will be presented in Chapter 4. Additional details regarding the post processing algorithm are provided in Appendix C.

CHAPTER 4 EXERGY ANALYSIS OF PAC SYSTEMS

4.1 Components of Exergy Analysis

The primary components necessary for conducting an exergy analysis of a control volume include: (1) defining the exergy reference environment to specify the dead state, (2) proper application of the exergy rate balance to account for flow exergy and all exergy transfer and destruction, and (3) evaluation of the thermodynamic property exergy. For multicomponent reacting systems, the chemical exergy needs to be correctly evaluated for species that are included in the exergy reference environment and for those not included in the exergy reference environment [7, 9, 60]. This chapter will address these items in detail and highlight issues that are unique to the specifics of PAC systems.

4.1.1 Exergy Reference Environment and the Dead State

Exergy is defined as *the maximum theoretical work that can be achieved by a system if it were allowed to come into complete thermodynamic equilibrium with a specified reference environment*. For a reacting multicomponent system, this process can be separated into two-stages. First, the control mass is allowed to come into thermal and mechanical equilibrium with the reference environment, which will be defined shortly, without exchanging mass with the reference environment. When the system and the reference environment are in equilibrium, the system is said to be at the restricted dead state. The maximum theoretical work that can be obtained as the system moves to the restricted dead state is called the *thermomechanical exergy*. Second, mass is exchanged between the control mass and the exergy reference environment until the system and the reference environment are in chemical equilibrium. At this point, there is no other opportunity for change, and the system is said to be at the dead state. The maximum theoretical work obtained in the second part of the process is the *chemical exergy*. An important subtlety which needs to be noted is, even if the control mass contained only the exact species as found in the exergy reference environment, as long they are in different concentrations the opportunity to extract additional work still exists. In the most general case, not only do the concentrations differ, but the composition of species as well, which is the scenario for this study [7, 9, 60].

From the aforementioned discussion, it is clear that selection of an appropriate exergy reference environment is essential for accurate exergy analysis. In many cases, the thermomechanical state of the reference environment is selected to coincide with the standard state used to evaluate thermodynamic and thermochemical properties which is, $T_{ref} = 298.15\text{ K}$ and $P_{ref} = 1\text{ atm}$. However this is not always the case, the selection of the

appropriate state of the exergy reference environment is arbitrary and dependent on the physical process being considered. For example, in the aerospace industry, where aircraft span a wide range of altitudes, much deliberation is given to selecting the appropriate state for the exergy reference environment. One such case is cited here [61]. The implication of this statement is, in general $T_0 \neq T_{ref}$ and $P_0 \neq P_{ref}$.

The second part of selecting the appropriate exergy reference environment deals with choosing its chemical composition. The selection of the chemical composition should be made such that every molecule in the system under consideration can be composed by the atoms that make up the molecules in the reference environment; this is a central key concept. Without this constraint there would be no way to have a self-consistent means of accounting for chemical exergy.

Table 4.1 Exergy reference environment [59]

Thermodynamic Properties	
<i>Property</i>	<i>Magnitude</i>
Pressure	1 atm
Temperature	298.15 K
Chemical Composition, 70% Relative Humidity	
<i>Species</i>	<i>Mole Fraction</i>
Argon, Ar (g)	0.009126
Nitrogen, N ₂ (g)	0.763312
Oxygen, O ₂ (g)	0.205304
Water, H ₂ O (g)	0.021898
Trace gases	0.000361

The reference environment selected for this model is given in Table 4.1 [59], and the method for its selection is consistent with well cited literature [62, 63]. Recalling the mechanism

species listed in Table 3.1⁷, every one of those molecules in Table 3.1 can be constructed directly or indirectly from species in the selected exergy reference environment. Although not listed here, the mechanism species have a definite exergy value relative to the reference environment; for the electronically excited species this is of special interest.

4.1.2 Governing Equations

The general form of the exergy rate balance for control volumes is given by Equation 4.1 [7]. Applying Equation 4.1 to a differential reactor plug (Figure 4.1) and invoking the

$$\frac{dE_{cv}}{dt} = \sum_{cs} \left(1 - \frac{T_0}{T}\right) \dot{Q} - \left(\dot{W}_{cv} - P_0 \frac{dV_{cv}}{dt}\right) + \sum_{in} (\dot{m}e_f)_{in} - \sum_{out} (\dot{m}e_f)_{out} - \dot{E}_d \quad (4.1)$$

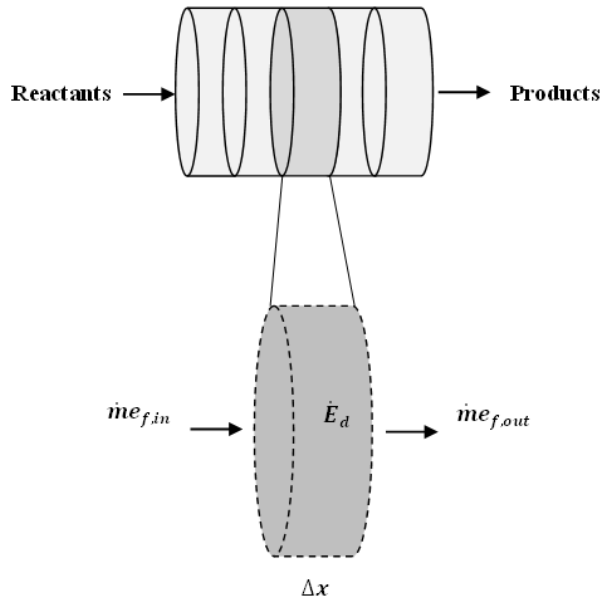


Figure 4.1 Exergy rate balance of a differential plug

assumptions cited in subsection 3.2.1 yields the result given in Equation 4.2.

⁷ The reference environment in Table 3.1 was used for both Phase I and Phase II of the study

$$\dot{m}_{in}e_{f,in}(x) = \dot{m}_{out}e_{f,out}(x + \Delta x) + \dot{E}'_d\Delta x \quad (4.2)$$

Although straight forward, this result is important because it provides insight on the methods used to calculate exergy destruction from the CHEMKIN-PRO[®] output variables in the post processing algorithm. Here, Δx represents the computational step size used by CHEMKIN-PRO[®] when executing its numerical scheme. The second term on the right-hand side of Equation 4.2 is the product of the exergy destruction per unit length and plug thickness, presented here to underscore its relationship to the computational step size. Rearranging

$$e_d = e_{f,in} - e_{f,out} \quad (4.3)$$

Equation 4.2 and using the result for from Equation 3.7, gives Equation 4.3.

The term on the left-hand side of Equation 4.3 is the mass specific exergy destruction and the two terms on the right-hand side are the inlet and outlet flow exergies. The flow exergy is the sum of the thermomechanical flow exergy and chemical flow exergy which both can be

$$e_f = e_f^{tm} + e_f^{ch} \quad (4.4)$$

subdivided yet further into even more elementary components of exergy [7, 9, 60].

The thermomechanical flow exergy is represented by Equation 4.5 [7, 9, 60]. Here the index i represents set of all mechanism species [59]. The terms inside brackets represent the

$$e_f^{tm} = \sum_i y_i [(h_i - h_{0,i}) - T_0(s_i - s_{0,i})] + \frac{V^2}{2} \quad (4.5)$$

physical exergy, and velocity term represents the kinetic exergy.

Looking at Equation 4.6 the chemical flow exergy is expressed in terms of all species

$$e_f^{ch} = e_{f,j}^{ch} + e_{f,k}^{ch} \quad (4.6)$$

entering or leaving the control volume [7, 9, 60, 64]. The component with the subscript j is the set of all mechanism species *not* included in the reference environment, where the subscript k is the set of all mechanism species which are included in the reference environment [59].

The contribution made to the chemical flow exergy by mechanism species which are not represented in the reference environment is given in Equation 4.7. The first term inside the brackets of Equation 4.7 is the product of the reciprocal of the molecular weight and the Gibbs

$$e_{f,j}^{ch} = \sum_j y_j [-M_j^{-1} \Delta_r G_j^o + R_j T_0 x_j \ln(x_j)] \quad (4.7)$$

free energy of reaction for the j th species. The Gibbs free energy of reaction is given in Equation 4.8.

$$\Delta_r G_j^o = \bar{g}_j^o + \sum_{j,k} v_{j,k} \bar{g}_{j,k}^o + \bar{R} T_0 \sum_{j,k} v_{j,k} \ln(x_j) \quad (4.8)$$

What differentiates this form of the Gibbs free energy from that of any other reaction, is for it to represent the chemical exergy of species *not* included in the reference environment, the non-reference environment species must react with species represented in the reference environment to produce species in the reference environment. This concept will play a key role in determining the chemical exergy for electronically excited species [59]. The second term inside the brackets is the exergy associated with mixing [7, 9, 46, 60, 65].

Equation 4.9 is the contribution of the mechanism species which are represented in the

$$e_{f,k}^{ch} = \sum_k y_k [-R_k T_0 \ln(x_j) + R_k T_0 x_k \ln(x_k)] \quad (4.9)$$

reference environment to the chemical flow exergy [7, 9, 60].

Revisiting Figure 4.1, the mass specific exergy destruction for a differential reactor plug

$$e_d \equiv T_0 s_g = \frac{\dot{E}_d}{\dot{m}} \quad (4.10)$$

is given by Equation 4.10. By definition, exergy destruction is equivalent to the product of the reference environment temperature and entropy generation.

Equation 4.11 represents the exergetic efficiency of combustion for the overall combustion process. Here the subscripts *in* and *out* refer to the inlet of the combustor and the

$$\varepsilon = \frac{e_{f,in} - e_d}{e_{f,in}} = \frac{e_{f,out}}{e_{f,in}} \quad (4.11)$$

outlet of the combustor, respectively.

Another metric commonly used to assess reactor performance is the molar conversion of fuel (MCF), depicted in Equation 4.12. In general reactors will have several rate driven

$$\eta_{MCF} = \frac{n_{H_2,react} - n_{H_2,prod}}{n_{H_2,react}} \quad (4.12)$$

processes occurring simultaneously which may affect a reactor's ability to convert fuel to product; a measure of this is the MCF. However, due to the model assumptions in this case the MCF is a direct measure of the reaction itself and how the introduction of singlet oxygen effects fuel conversion. A similar metric used to assess combustion performance is completeness of combustion (Equation 4.13). For hydrogen combustion it is a measure of the fraction of

$$\eta_{CoC} = \frac{n_{H_2O,prod}}{n_{H_2,react}} \quad (4.13)$$

hydrogen that has been converted to water [66].

4.1.3 Chemical Exergy of Electronically Excited Species

A major challenge to performing an exergy analysis of a PAC system is proper evaluation of the chemical exergy of the electronically excited species. A method was developed by Washington and Shapiro [59] which addresses this issue.

The fundamental problem is that under normal circumstances electronically excited species are not present in the environment at sea level, where most combustion processes occur. Based on prior discussion it has been established that for self-consistency for the purpose of exergy accounting, that all mechanism species must be able to be composed from species in the exergy reference environment. For the species under consideration here, $O(^1D_2)$, $O_2(a^1\Delta_g)$, $OH(A^2\Sigma^+)$, all of the atoms and molecules are available to construct them from species in the reference environment. However, the species in the reference environment are at their respective ground states. To deal with this, it is necessary to determine the maximum theoretical work that is associated with the difference in electronic states.

Deactivation of electronically excited species typically occurs one of three ways; the particle can undergo a photoluminescent process where radiant emission occurs (Equation 4.14) [46]. However, as a first approximation, issues surrounding radiant energy exchange with the



reference environment are not addressed, so this mode of deactivation is not considered. The other two modes of deactivation involve quenching. The first quenching mechanism is reactive quenching, shown in Equation 4.15 [67, 68]. Here the excited species is consumed in the



reaction. The second mechanism is collisional quenching, given in Equation 4.16 [47, 69]. In

both cases, idealized quenching was assumed, where the resulting products are in the reference environment at their ground states. Applying this concept and using Equations 4.7 and 4.15 the chemical exergies for $O(^1D_2)$ and $OH(A^2\Sigma^+)$ were calculated. For $O_2(a^1\Delta_g)$ Equations 4.7 and 4.16 were used. The resulting exergy destruction calculations using this method were in excellent agreement with exergy destruction calculations made using the entropy balance [59].



This result is significant because the entropy balance is independent of the selection of the exergy reference environment.

4.2 Exergy Analysis Results

Now that NTPs and their characteristics have been given, a detailed description of the chemical simulation has been laid out and, a set of governing equations derived; the primary combustion zones of the reactor can be defined and results from the exergy analysis presented.

4.2.1 Characterization of Combustion Zones

Characterizing the various combustion zones in the reactor helps guide the discussion regarding the chemical kinetics of oxidation and its influence on exergy destruction. The defined reaction zones in Figure 4.2 [70] look very similar to the structure commonly associated with premixed laminar flames [71]; however, the underlying physical processes which are responsible for ignition are quite different.

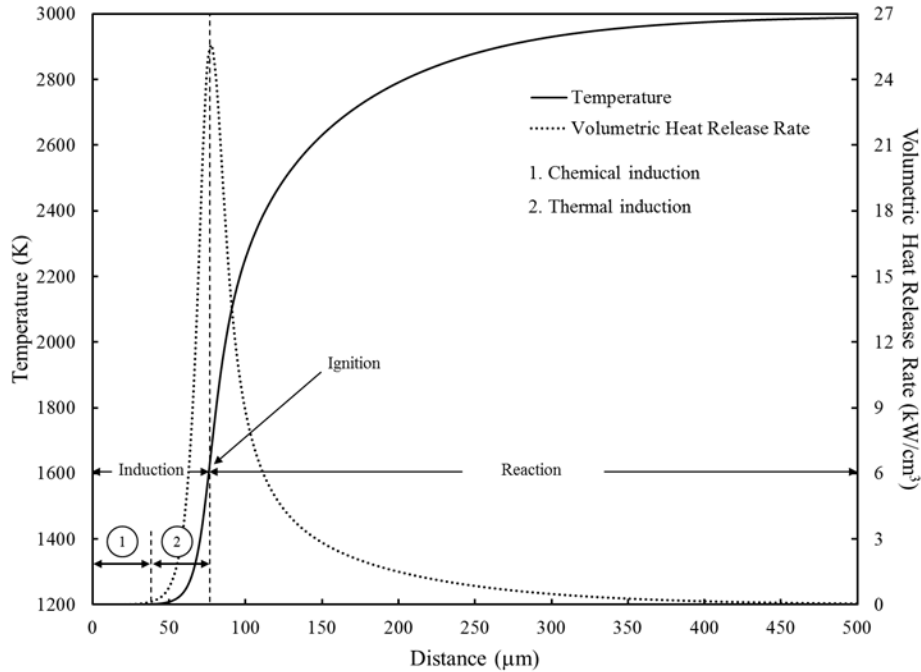


Figure 4.2 Characterization of combustion zones

The region preceding ignition is the induction zone. In this zone self-heating occurs due to chemical reaction until enough energy is liberated to sustain stable combustion. A more detailed explanation reveals that the induction zone is divided into two characteristic distances which are defined by different chemical processes that foster ignition.

The first distance is the chemical distance⁸ (or time). This distance is the length needed to achieve the degenerate chain branching step, as well as the critical concentration of radicals and chain carriers. There is very little chemical energy liberated over this distance, which can be seen in Figure 4.2 by examining the volumetric heat release curve. The second distance is the thermal distance, and it is characterized by the length required to liberate enough thermal energy through steady reaction to induce ignition. It is apparent from Figure 4.2 that the rate of heat release increases tremendously in the thermal zone [72].

⁸ Since the governing equations for PFR are explicitly a function of distance, all variable will be described accordingly; however, all corresponding distances can be converted to time using a characteristic velocity.

Ignition (induction) delay is defined in the literature various ways, including: (1) achieving a certain concentration of radicals or chain carriers [73, 74], (2) evaluating the time rate of change of various radicals and chain carriers, or temperature [75, 76], and (3) achieving a specific differential change in temperature to determine when ignition occurs [77]. For this analysis, the inflection point of the temperature gradient was used to define ignition, as is customary for plug flow reactor models [78].

Following ignition is the primary reaction zone where the bulk of the chemical energy is released. Examining the temperature gradient in Figure 4.2, the largest temperature rise occurs after ignition. Although the volumetric heat release rate reaches an absolute maximum at ignition, as it decreases the area bound under the curve after ignition is greater than the bounded area before ignition. All the processes discussed here are categorized as self-ignition, spontaneous ignition or autoignition, and are applicable to premixed adiabatic systems. It should also be noted that the incoming charge be heated to sufficiently high temperatures to initiate this process [72].

4.2.2 Exergy Destruction and Exergetic Efficiency

The first graphs to be presented are those which illustrate the how exergy destruction evolves as chemical flow exergy is converted to thermomechanical flow exergy. Figure 4.3 [59] represents the baseline case (Model IA), where 0% singlet oxygen was introduced into the charge. It is also a direct representation of information obtained from Equations 4.4 - 4.10. Referring back to the discussion on reaction zones, although neither the temperature nor volumetric heat release gradients are displayed on this graph, the trends in chemical flow exergy conversion and thermomechanical flow exergy evolution are direct measures of chemical

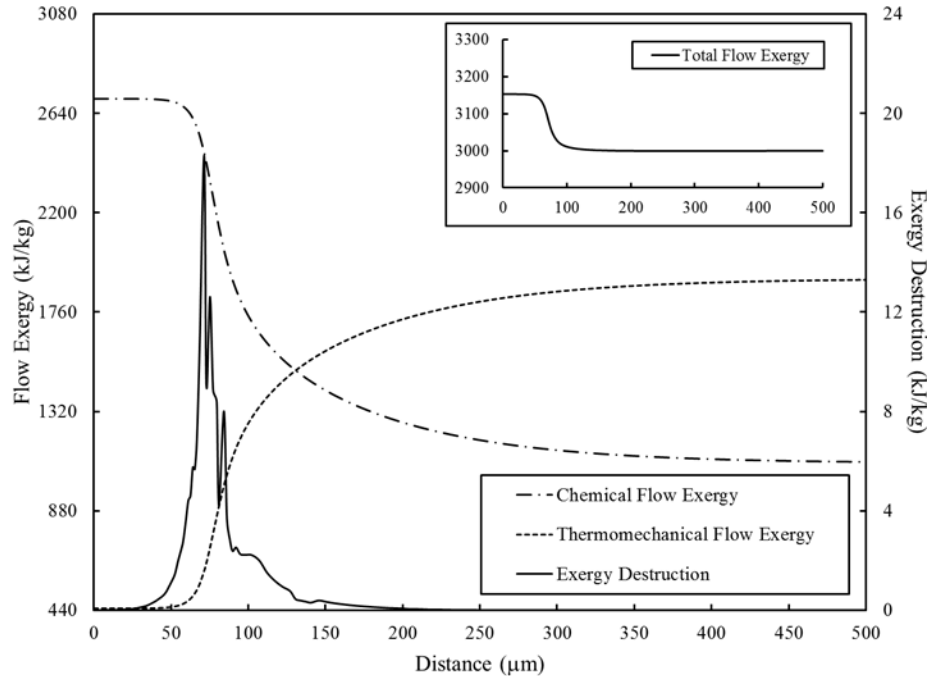


Figure 4.3 Flow exergy and exergy destruction vs. distance for 0% inlet $O_2(a^1\Delta_g)$ [59]

reaction. With this in mind it can be seen that throughout the chemical induction zone there is not much exergy destruction associated with radical buildup; however, at the onset of the thermal induction zone there is a sharp increase in the exergy destruction curve. It will be demonstrated shortly that under these conditions the exergy destruction curve reaches its maximum just prior to ignition. The inlaid graph represents the trend in the total flow exergy, which precisely depicts how much exergy has been destroyed due to oxidation.

Figure 4.4 [59] is the case for 10% excited oxygen (Model IB) in the charge. Comparing Figure 4.4 to Figure 4.3, there is a significant reduction in the maximum value for the exergy destruction. As discussed in literature [79], there is a significant reduction in the ignition delay time. Upon examination, it can be seen that the length of the chemical zone has been reduced substantially, implying a rapid increase in the rate of at which key radicals and chain carriers are being produced. This is reflected in the exergy destruction trend, where the destruction of

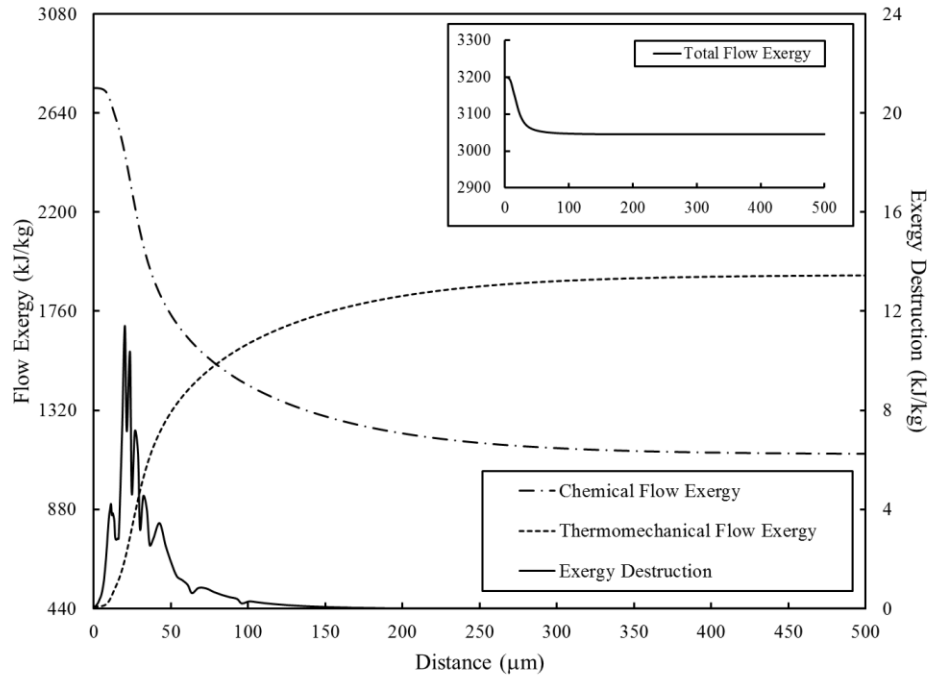


Figure 4.4 Flow exergy and exergy destruction vs. distance for 10% inlet $O_2(a^1\Delta_g)$ [59]

exergy begins almost immediately. The thermal zone has not undergone any notable change, other than occurring at a shorter distance.

For 25% excited oxygen in the charge (Model IB), shown in Figure 4.5 [59], the chemical

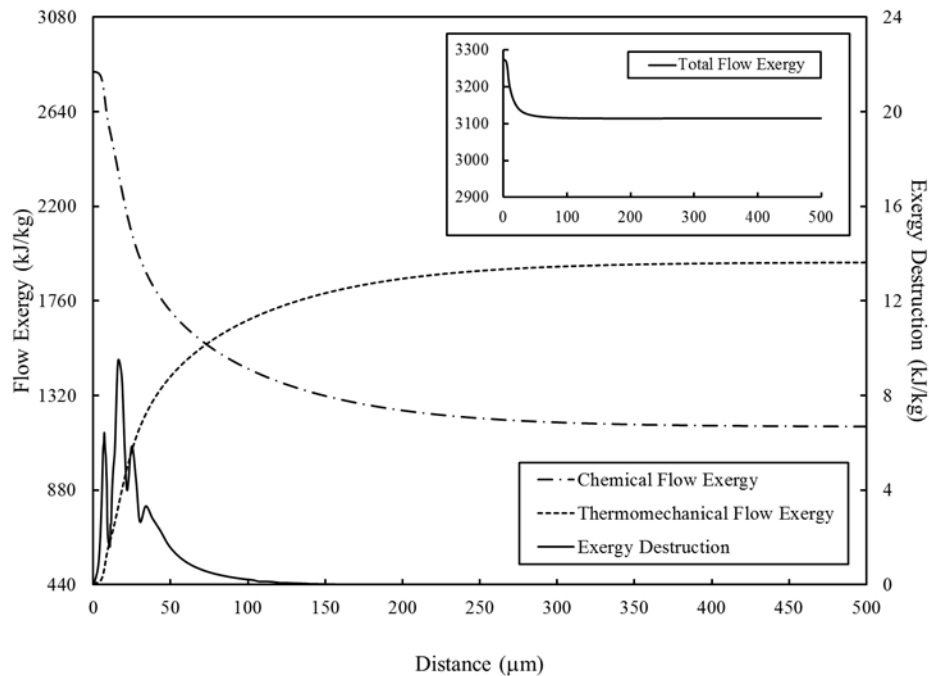


Figure 4.5 Flow exergy and exergy destruction vs. distance for 25% inlet $O_2(a^1\Delta_g)$

induction zone has been reduced even further. As was the case in Figure 4.4, the maximum exergy destruction value has been further reduced. The thermal induction zone or thermomechanical flow exergy have not undergone any significant changes.

Figure 4.6 [59] is a plot of the exergy destruction and temperature versus distance for the baseline case which provides insight into how much exergy destruction is occurring before

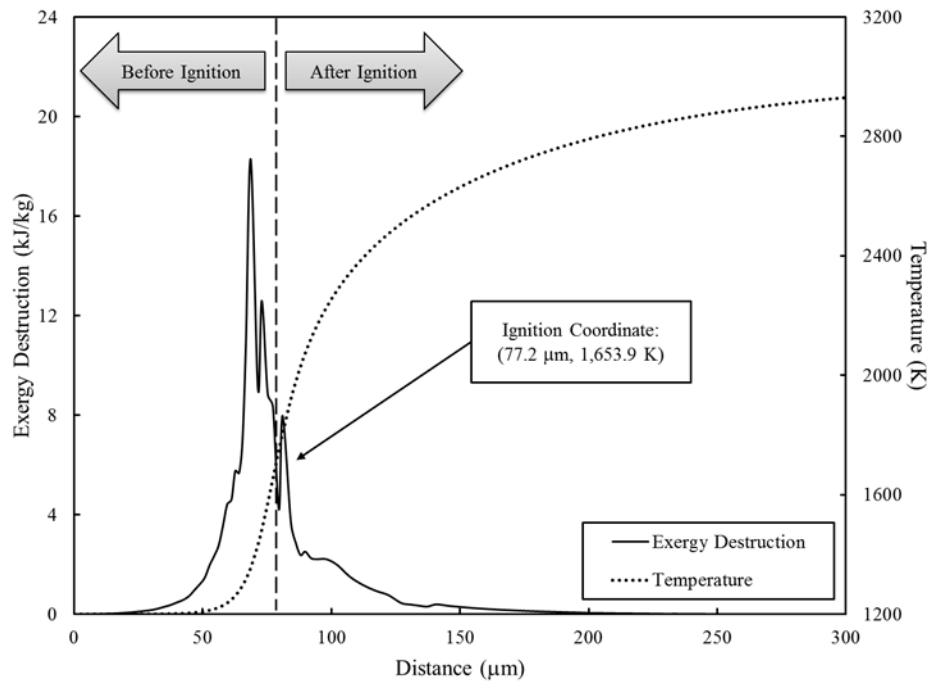


Figure 4.6 Exergy destruction and temperature vs. distance for 0% inlet $O_2(a^1\Delta_g)$ [59]

ignition and what portion is occurring post ignition. For 0% singlet oxygen in the charge, it is clear that the largest fraction of destruction occurs before ignition and after the chemical zone; therefore, in the thermal zone. Figure 4.6 also complements Figure 4.7 [59]. Figure 4.7 is a plot of total exergy destruction before ignition and ignition temperature versus inlet percentages of excited oxygen, ranging from 0% - 100% of the charge. Additionally, Figure 4.7 also shows two very important trends. First, for inlet charge compositions ranging from 0% - 20% the bulk of the total exergy destruction occurs before ignition. Second, there is a dramatic reduction in

ignition temperature between 20% and 25% inlet excited oxygen. Popov [80] discusses the introduction of NTPs, generated by various methods, into hydrogen-oxygen combustion and presents numerical results suggesting that NTP generated by electric discharge can reduce the ignition temperature by 500 - 600 K. Figure 4.7 shows a reduction of approximately 450 K. A third interesting trend illustrated in Figure 4.7 is the rebounding in ignition temperature up to 95% inlet singlet oxygen, followed by a 150 K reduction at 100%.

Figure 4.8 [59] shows that the exit thermomechanical flow exergy experiences a 6% increase and the exit gas temperature increases by 4%, with increasing percentages of excited oxygen. These trends are related directly to what is observed in Figure 4.9 [59]. In Figure 4.9, the exit chemical exergy experiences a 24% increase and the molar conversion of fuel decreases by 3%. Upon initial inspection, results from Figure 4.8 and Figure 4.9 appear to contradict each other; however, this is not the case. It is well cited in the literature [3] that the presence of singlet oxygen reduces the energy required to sustain various endothermic reactions in the mechanism; this will be explicitly demonstrated later in this chapter. Therefore, even though there is less fuel being converted to products, this is offset by the fact that less energy is being used to drive the reaction, and the residual energy appears as an incremental increase in temperature. With regard to the chemical flow exergy, since unreacted fuel is leaving the reactor there is a potential to extract additional work; therefore, its value must increase to reflect this.

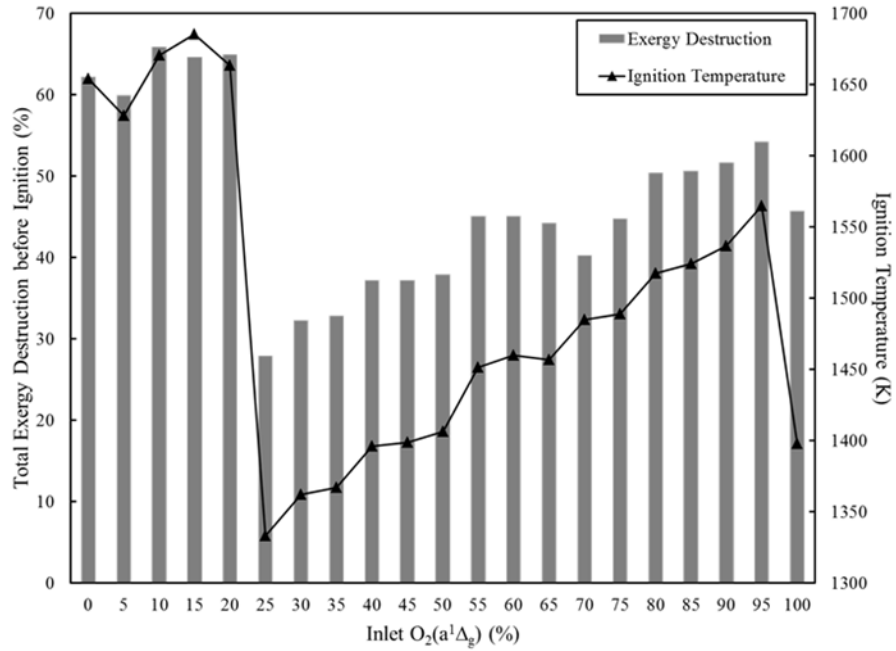


Figure 4.7 Total exergy destruction before ignition and ignition temperature vs. inlet percentages of $O_2(a^1\Delta_g)$ [59]

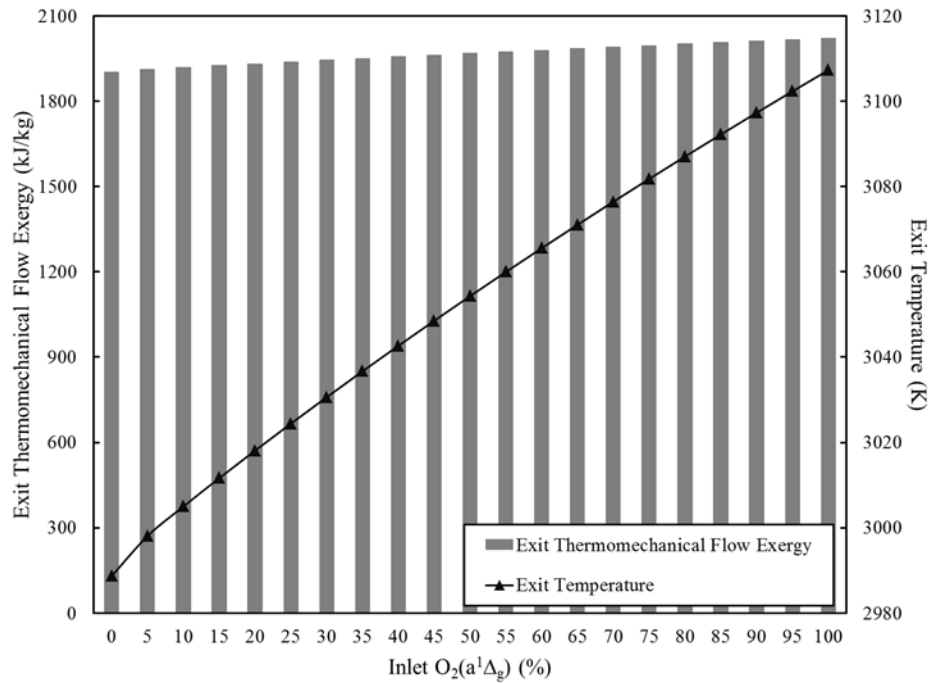


Figure 4.8 Exit thermomechanical flow exergy and exit temperature vs. inlet percentages of $O_2(a^1\Delta_g)$ [59]

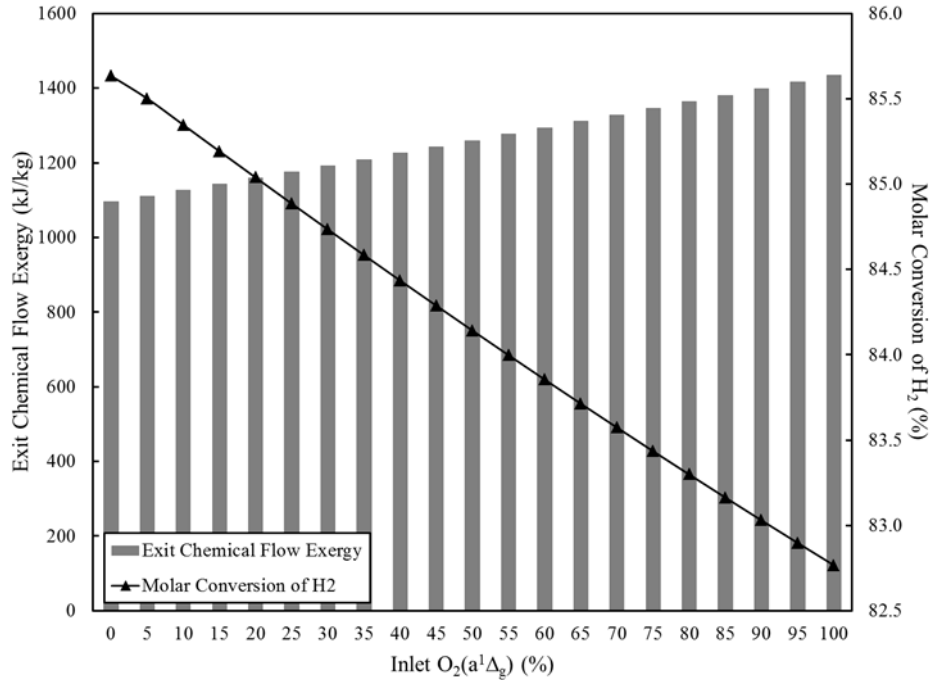


Figure 4.9 Exit chemical flow exergy and molar conversion of H₂ vs. inlet percentages of O₂(a¹Δ_g) [59]

Figure 4.10 [59] shows that the completeness of combustion experiences approximately a 7% reduction with increasing quantities of singlet oxygen. This is intriguing because from Figure 4.9 the molar conversion of hydrogen only decreased by 3%, which implies that as increasing amounts of singlet oxygen are added to the charge the mechanism is impacted in a fundamental way, whereby hydrogen is being diverted from elementary reactions associated with the formation of water. Recalling Table 3.1, aside from molecular hydrogen (fuel) and water all the other species containing hydrogen atoms are radicals or potential chain carriers.

From Figure 4.11 [59], an optimal range of inlet charge composition can be identified from 0% - 20%, the maximum occurring at approximately 10%. Outside of this range, exergetically, the production of the singlet oxygen outweighs the benefits of its use. Although this seems to be a very slight increase in efficiency, this trend is significant. After 20%, the

efficiency drops off by almost one full percentage point. As will be discussed later in Chapter 5, Dunbar and Lior [2] estimated that for hydrogen-oxygen combustion in an adiabatic flow reactor from fuel-lean to stoichiometric conditions the range for the exergetic efficiency is 95% - 96.5%. Although here stoichiometric combustion is being considered, it underscores the significance of the loss of one percentage point. Conversely, over the optimal range, exergetically, there is advantage for the use of singlet oxygen in addition to reaping all the other cited benefits of its use.

Upon reviewing the presented data, there are several key trends and behaviors that require further explanation. For increasing percentages of singlet oxygen, the chemical induction zone is significantly reduced. Over the optimal range of exergetic efficiency, as excited oxygen is added to the charge, a large portion of the total exergy destruction occurs before ignition and in the thermal induction zone. At 25% there is a significant reduction in the ignition temperature; this also marks the decline in exergetic efficiency. The exit reactor temperatures increase, even though the molar conversion of fuel decreases, due to reductions in the required energy to facilitate various endothermic reactions. The completeness of combustion decreases at a faster rate than the molar conversion of fuel. This indicates that as excited oxygen is added not only is less fuel converted to product, but hydrogen is diverted away to from water forming reactions to produce more radicals and chain carriers. In order to gain more insight into these phenomena, a detailed mechanism analysis is required [50, 81].

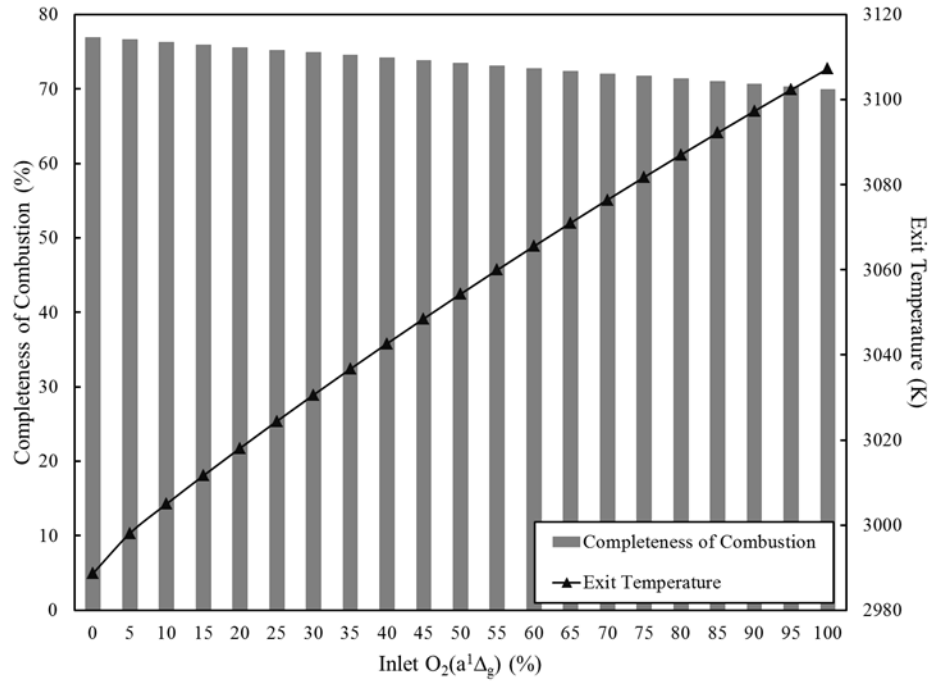


Figure 4.10 Completeness of combustion and exit temperature vs. inlet percentages of O₂(a¹Δ_g)

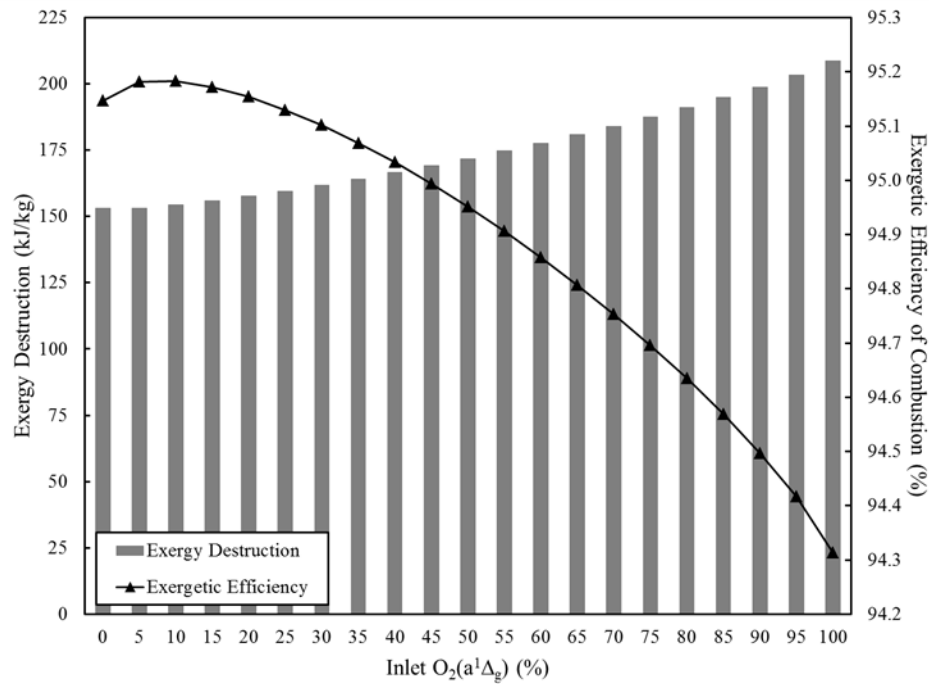


Figure 4.11 Exergy destruction and exergetic efficiency of combustion vs. inlet percentages of O₂(a¹Δ_g) [59]

4.3 Reaction Mechanism Analysis Results

In this section, results from a detailed analysis of the Moscow State University mechanism are presented to shed light on the phenomena observed regarding exergy destruction and efficiency from the previous section. The goal is to understand how the chemical kinetics of the mechanism is affected by singlet oxygen, which in turn drives the trends detected in exergy destruction.

Two methods will be used to assess the chemical kinetics of the mechanism: sensitivity analysis and rate-of-production (reaction flow⁹) analysis [72]. Sensitivity analysis allows for the identification of the rate limiting or controlling reaction step in a mechanism [6, 72, 82]. Rate-of-production analysis is a means by which to evaluate how much various elementary reactions in the mechanism contribute to the production or consumption of species of interest [6, 72, 82].

In addition to determining what the rate limiting reactions are in a mechanism, sensitivity analysis also allows a determination to be made of the relative importance of reactions in the mechanism. There are two categories of sensitivity analysis deterministic and stochastic. For the purposes of this study the discussion will be limited to the deterministic approach. Sensitivity analysis is centered on determining the uncertainties associated with various parameters relative to other system variables [6, 72, 82]. CHEMKIN-PRO[®] is capable of performing sensitivity analysis, the results of which are first-order sensitivity coefficients [4, 6, 82]. The sensitivity coefficients considered here are representative of the uncertainty associated with temperature and species fraction relative to rate coefficients [4]. The larger their magnitude, the more uncertainty there is associated with a particular reaction. Positive coefficients correspond to the formation of a particular species by an elementary reaction, and

⁹ Throughout the document rate-of-production analysis and reaction flow analysis will be used interchangeably

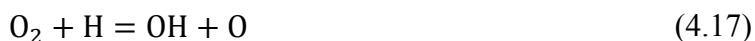
negative coefficients correspond to the consumption of a specific species by a reaction [76, 83, 84].

Reaction flow analysis can also be subdivided into, local and integral analyses. Local reaction flow analysis provides information regarding the formation or destruction of species at specific locations along the reactor. Integral reaction flow analysis provide integrated values of formation and consumption over the length of the reactor [6, 72, 82]. Both types of reaction flow analysis are used here. CHEMKIN-PRO[®] has a reaction path analyzer feature which allows for the generation of reaction flow diagrams to indicate the relative rates of production for various species and the responsible reaction. Additionally, CHEMKIN-PRO[®] provides raw rate-of-production data in the streamwise direction of the reactor [4].

4.3.1 Background on Hydrogen-Oxygen Combustion

To provide context for the ensuing discussion a brief background needs to be given regarding chain reaction and various features of high temperature hydrogen oxidation. Chain reactions can be classified as unbranched and branched. Combustion is described by chain branching reactions. Chain branching reactions include four fundamental steps: (1) initiation, (2) propagation, (3) branching, and (4) termination. The chain branching step is the one that makes rapid oxidation possible through the formation of radicals. By definition a chain branching reaction is one where two radicals are formed and one is consumed [55].

For hydrogen and many hydrocarbons at high temperature (>1100 K), the chain branching reaction given in Equation 4.17 is among the most dominant chain branching steps in



combustion. It is generally characterized by having large sensitivity coefficients, and atomic hydrogen is the limiting reactant. This reaction plays an important role in establishing a benchmark for comparing the kinetics of the baseline case to extended model runs [85].

4.3.2 Sensitivity and Reaction Flow Analyses

Analyses of results are now presented with the goal of providing additional insight into the trends observed in exergy destruction and exergetic efficiency. For our purposes, the methods are inextricably linked; therefore, results will be presented simultaneously from both analyses in support of the underlying goal.

4.3.2.1 0% Inlet $O_2(a^1\Delta_g)$

Figure 4.12 is a reaction flow diagram which shows the relative rates of production and reaction pathways with respect to triplet oxygen for the base case. The majority of the triplet

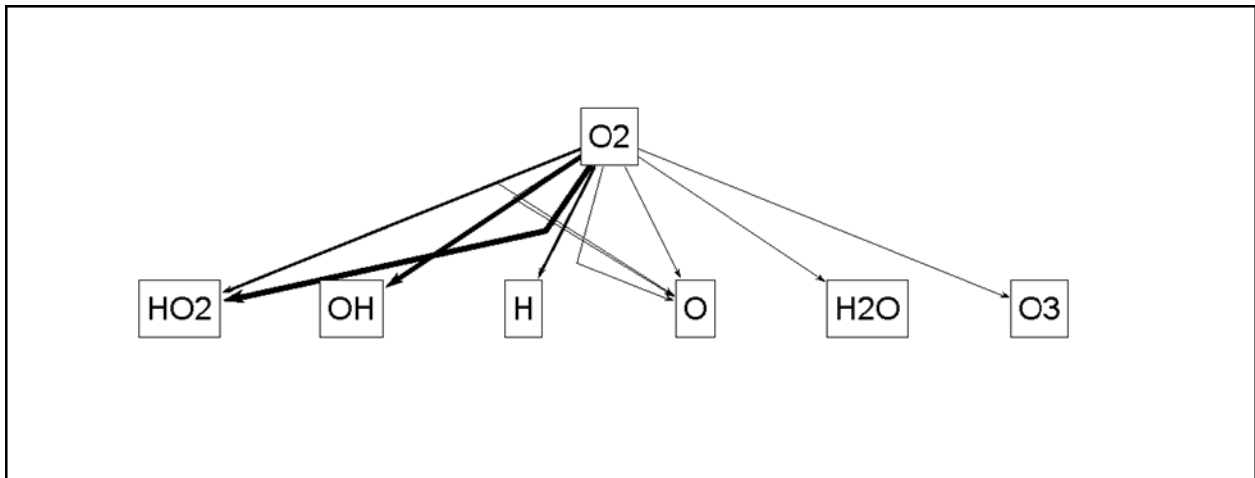


Figure 4.12 Reaction flow diagram for 0% inlet $O_2(a^1\Delta_g)$, $\Phi = 1$, and $T_{in} = 1200$ K [59]

oxygen is used to form hydroperoxyl and hydroxyl. At lower temperatures, hydroperoxyl is associated with chain termination. However, an examination of ignition limit curves and kinetics for hydrogen combustion at 1 atm and 1200 K show that hydroperoxyl becomes very reactive.

For these conditions, the reaction path diagram shows that the formation of atomic hydrogen is also associated with triplet oxygen. The formation of atomic oxygen by molecular oxygen has several smaller pathways leading to its production. Direct formation of water and ozone by ground state molecular oxygen is very limited. However, the mechanism contains many pathways by which triplet oxygen indirectly produces species that are important to fostering the production of both water and ozone.

Figures 4.13 [59] and 4.14 are mole fraction distributions along the reactor length for the primary species and minor species, respectively. The trends displayed in Figure 4.13 confirm what was suspected when examining the exergy destruction trends for the same case, most of the reaction occurs in the thermal induction zone. This is supported by the increase in water and hydroxyl formation before ignition. More interesting are the mole fraction trends of the radicals and other reactive species shown in Figure 4.14; notice that the vertical axis has a logarithmic scale. The trends in Figure 4.12 are supported by the mole fraction distributions in Figure 4.14. Note of all the reactive species, hydroperoxyl starts at the largest fraction. These results are notable because hydroperoxyl is not included in the inlet reactant composition; additionally, Figure 4.14 shows that along with atomic hydrogen and oxygen, hydroxyl has the largest magnitude. Ironically, all of this occurs with very little consumption of oxygen. Initially hydroperoxyl and hydroxyl are five and six orders of magnitude smaller than oxygen. Figure 4.14 provides insight into what roles each of the species play in the chemical and thermal induction zones.

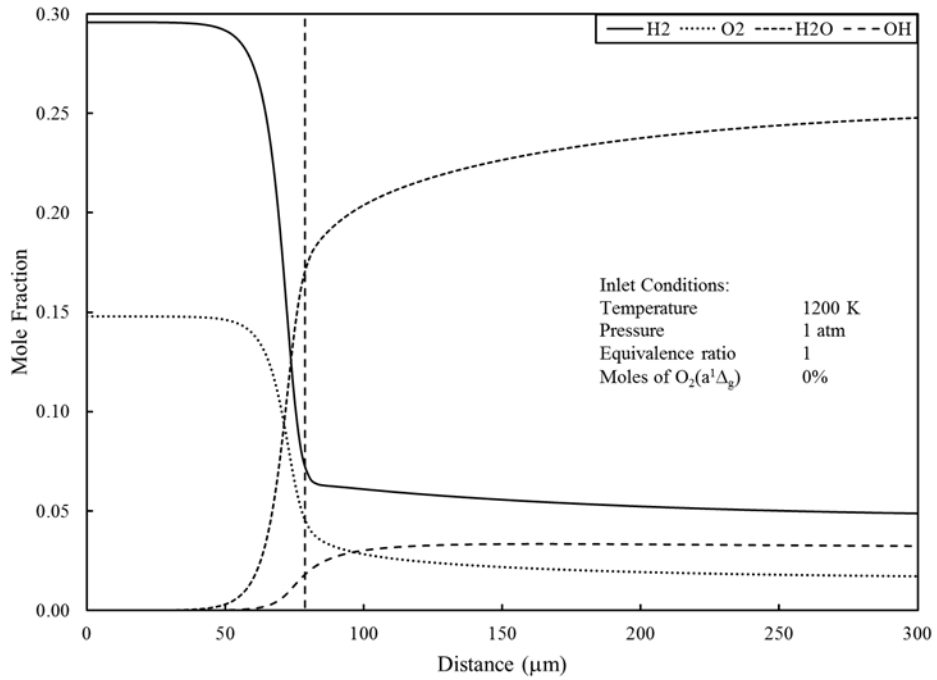


Figure 4.13 Mole fractions of primary species vs. distance for 0% inlet O₂(a¹Δ_g), Φ = 1, and T_{in} = 1200 K

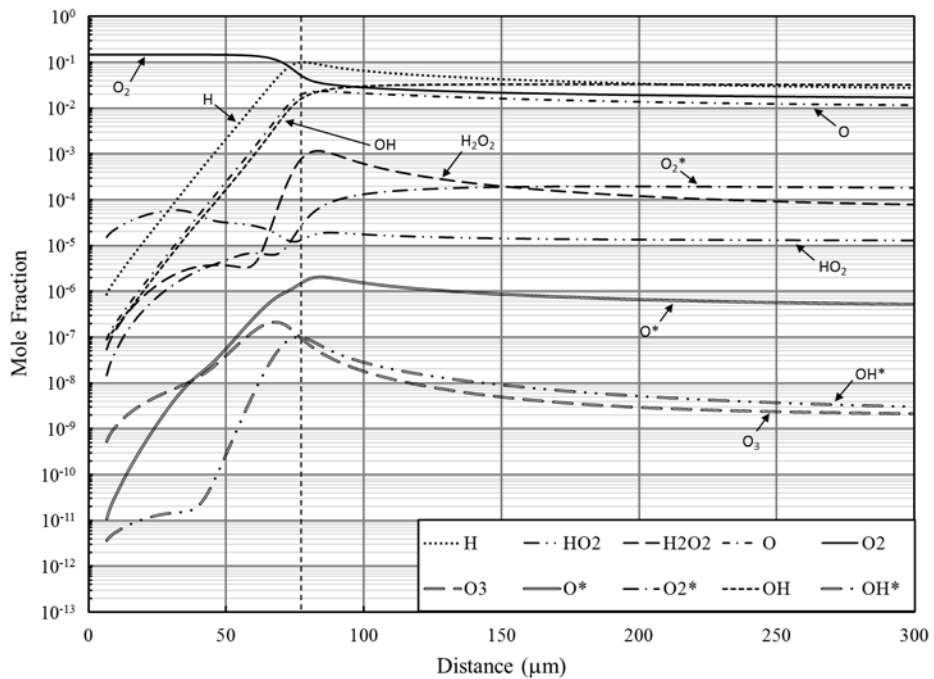


Figure 4.14 Mole fractions of radicals and chain carriers vs. distance for 0% inlet O₂(a¹Δ_g), Φ = 1, and T_{in} = 1200 K

Comparing Figures 4.14 and 4.15 it appears that the presence of hydrogen peroxide increases rapidly in the thermal induction zone, just ahead of ignition. The quantity of electronically excited hydroxyl also increases by a significant amount before ignition.

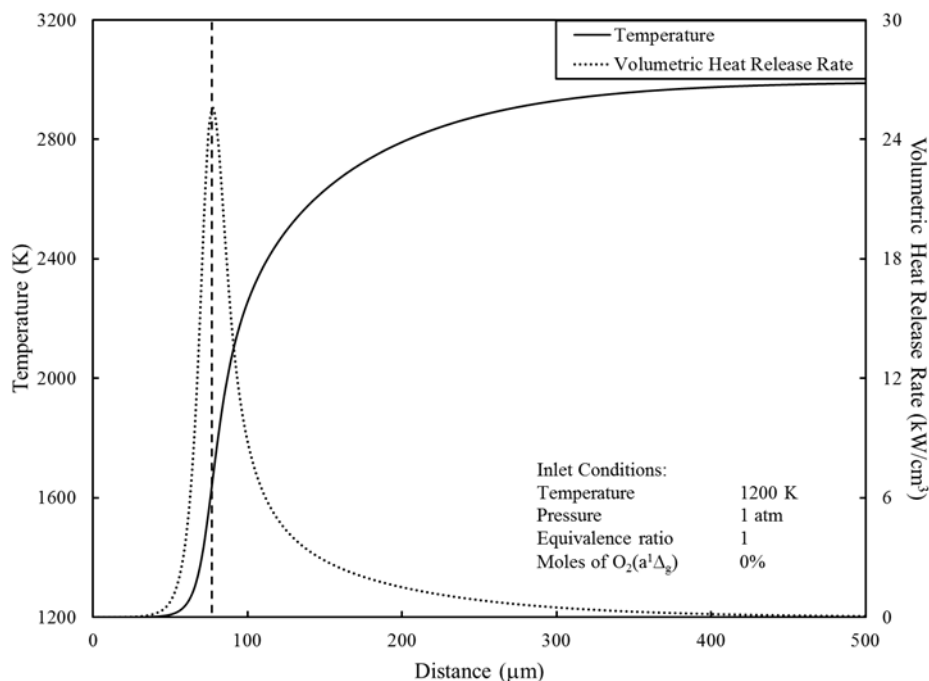


Figure 4.15 Temperature and volumetric heat release rate vs. distance for 0% inlet $O_2(a^1\Delta_g)$, $\Phi = 1$, and $T_{in} = 1200$ K

Figure 4.16 is a global sensitivity analysis of the overall reaction mechanism. Here the term global¹⁰ is used in the sense that all sensitivity coefficients for the entire mechanism were evaluated to find the top ten largest magnitudes, five positive and five negative. As mentioned in the subsection on hydrogen oxidation, R17 (refer to Appendix A for complete mechanism) surfaced as the dominate rate limiting reaction for several species; especially, for the formation of hydrogen peroxide. This is a key point for later discussion.

¹⁰ Here global should not be taken to mean global sensitivity associated with a stochastic analysis

Figure 4.17 represents the global sensitivity analysis of triplet oxygen. It depicts that the consumption of ground state oxygen is most sensitive to R17. The next largest sensitivity coefficient is for R18, which is also a chain branching reaction. Both of these are followed by the chain propagation reaction, R15. Reaction R17 and R18 are closely related, as they both produce species the other needs to sustain reaction.

Figure 4.18 shows the local sensitivities of triplet oxygen in the streamwise direction relative to R17. As expected, the maximum sensitivity occurs just before ignition. The local rate of production relative to R17 is given in Figure 4.19. Figure 4.20 shows that the overall rate of production trend is very close to that of Figure 4.19; this indicates that R17 is the dominate reaction involved in the consumption of triplet oxygen. Both Figures 4.19 and 4.20 indicate the maximum rate of consumption of triplet oxygen occurs just before ignition, which is in agreement with Figure 4.13.

According to Figure 4.21, hydroxyl is also very sensitive to R17. Although R18 is also a chain branching reaction, its sensitivity coefficient is less than half that of R17. This is mostly due to dependence of R17 on atomic hydrogen; the limiting reactant. The reaction with the third largest sensitivity is, R3; R3 a chain initiating reaction, which produces two hydroxyl molecules.

Figure 4.22 is the local sensitivity of hydroxyl relative to R17. The trend is similar to the mole fraction trend in Figure 4.14, where the maximum occurs just before ignition. This trend is supported by Figures 4.23 and 4.24, the local and total rates of production. Notice that even though both graphs are similar, the magnitudes are significantly different.

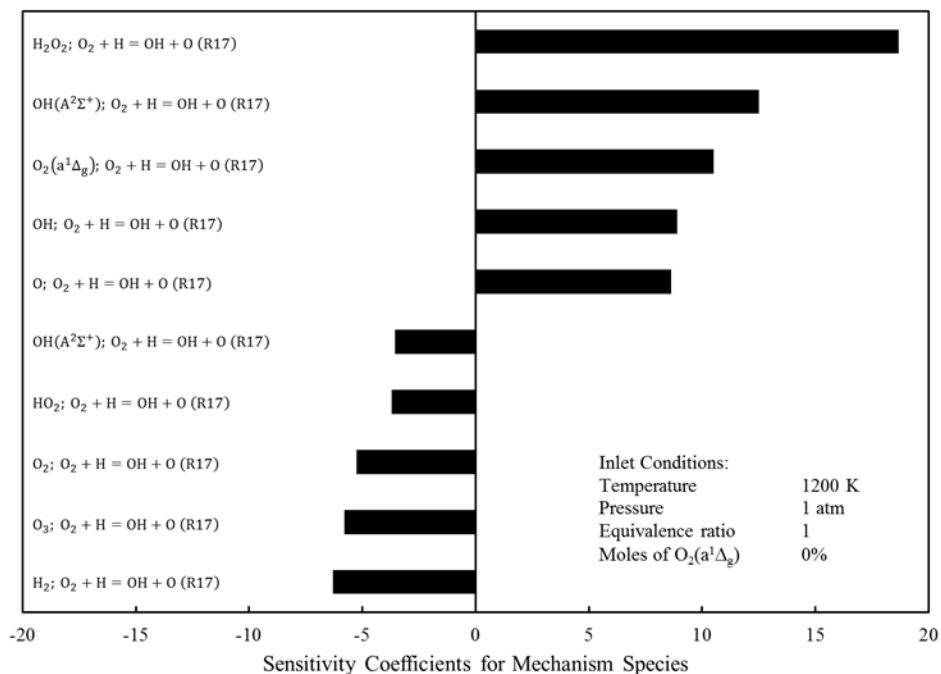


Figure 4.16 Global sensitivity analysis of the overall mechanism for 0% inlet O₂(a¹Δ_g), Φ = 1, and T_{in} = 1200 K

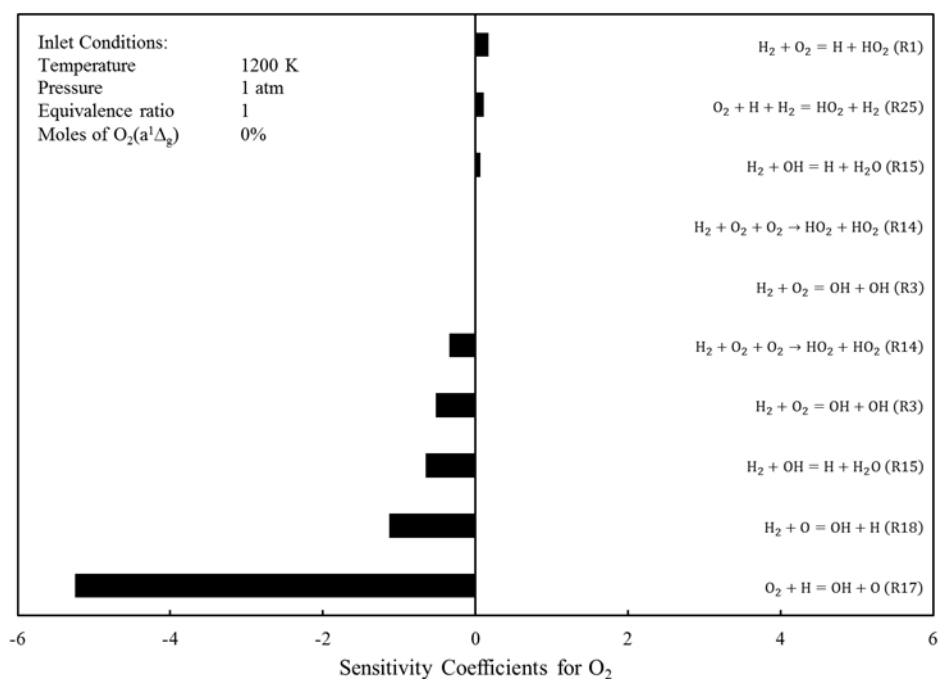


Figure 4.17 Global sensitivity analysis of O₂ for 0% inlet O₂(a¹Δ_g), Φ = 1, and T_{in} = 1200 K

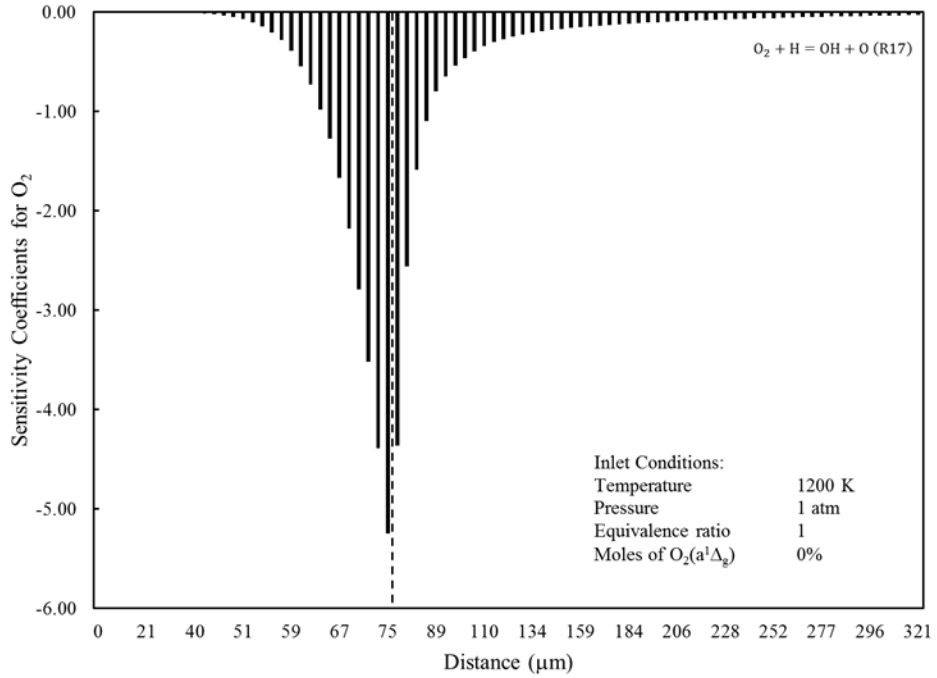


Figure 4.18 Local sensitivity analysis of O₂ for 0% inlet O₂(a¹Δ_g), Φ = 1, and T_{in} = 1200 K

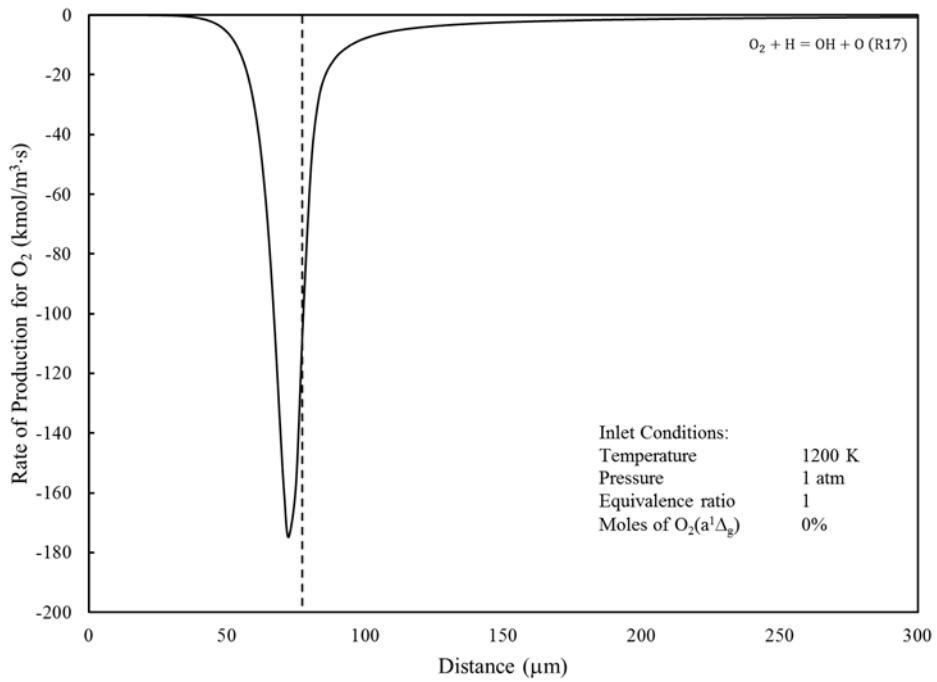


Figure 4.19 Local rate of production of O₂ for 0% inlet O₂(a¹Δ_g), Φ = 1, and T_{in} = 1200 K

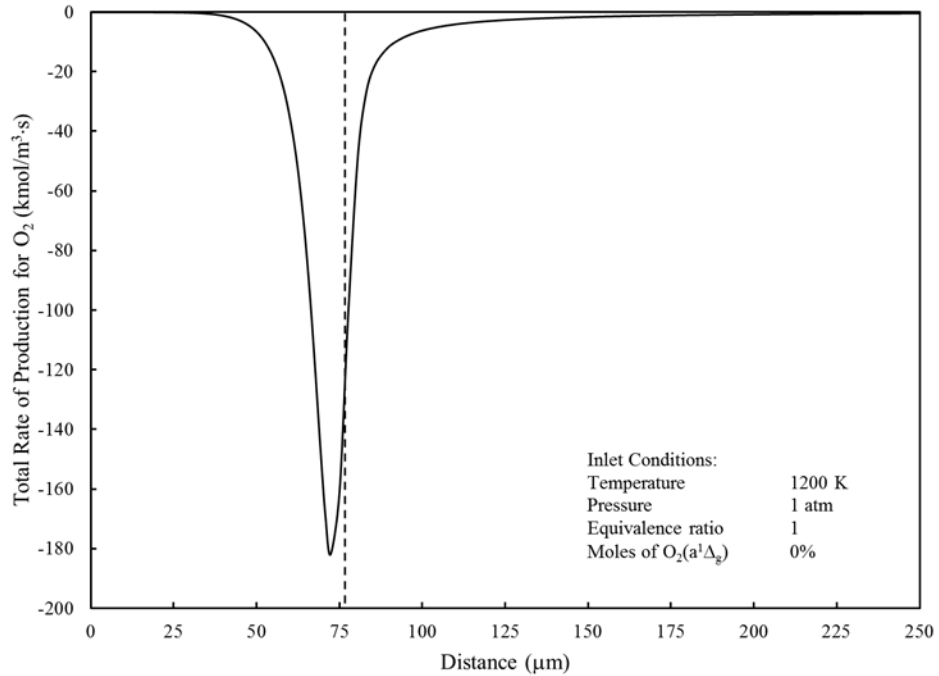


Figure 4.20 Total rate of production of O_2 for 0% inlet $O_2(a^1\Delta_g)$, $\Phi = 1$, and $T_{in} = 1200$ K

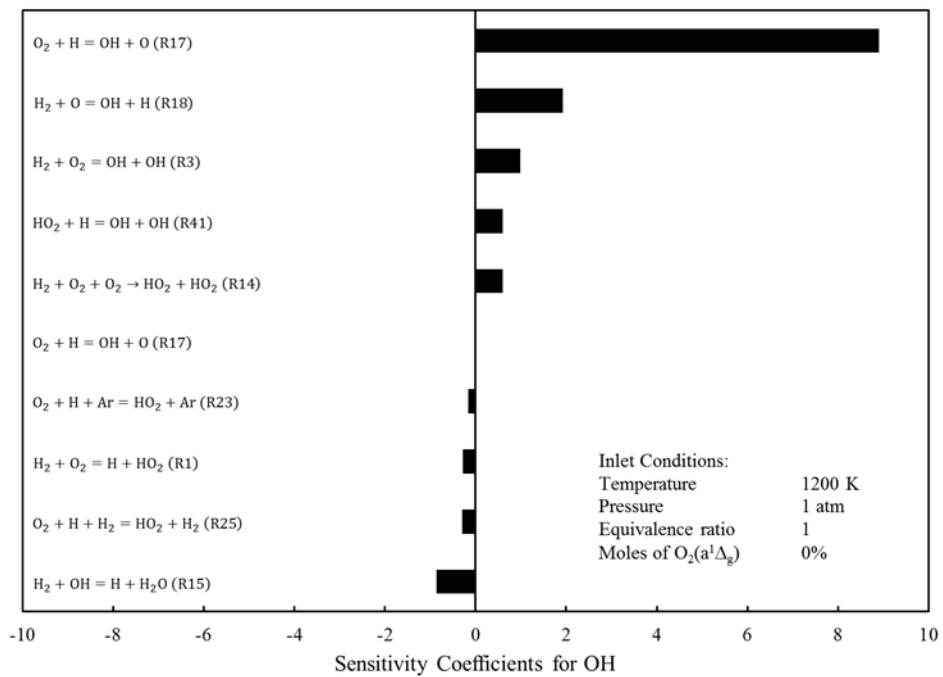


Figure 4.21 Global sensitivity analysis of OH for 0% inlet $O_2(a^1\Delta_g)$, $\Phi = 1$, and $T_{in} = 1200$ K

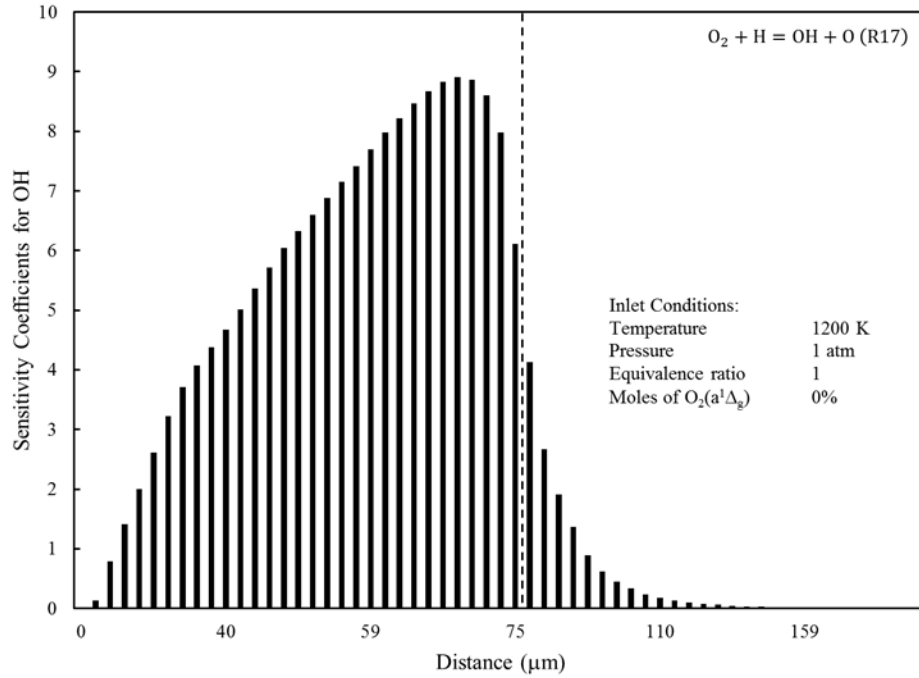


Figure 4.22 Local sensitivity analysis of OH for 0% inlet $O_2(a^1\Delta_g)$, $\Phi = 1$, and $T_{in} = 1200$ K

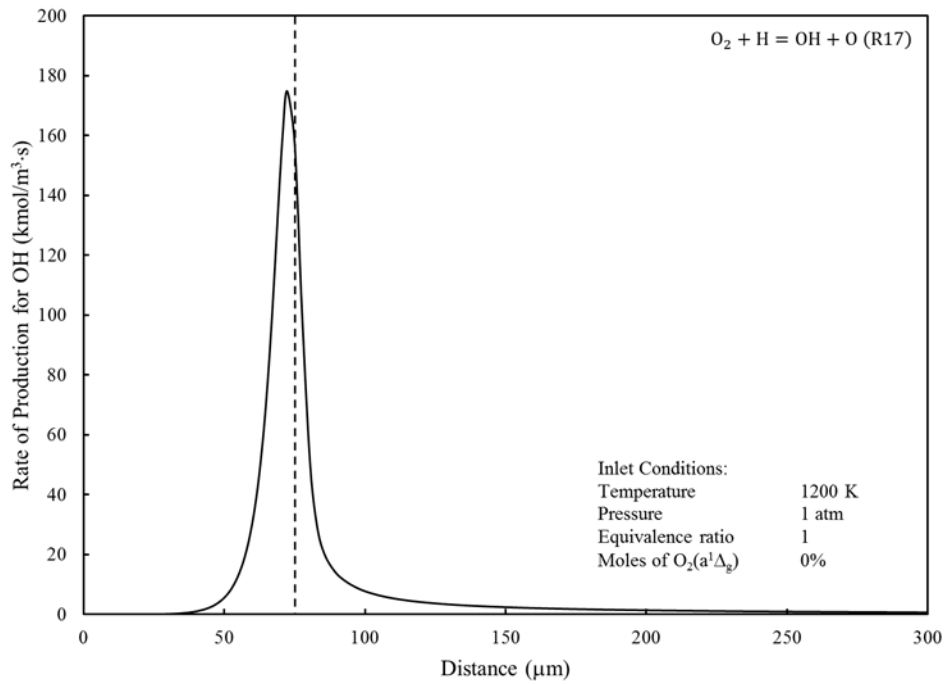


Figure 4.23 Local rate of production of OH for 0% inlet $O_2(a^1\Delta_g)$, $\Phi = 1$, and $T_{in} = 1200$ K

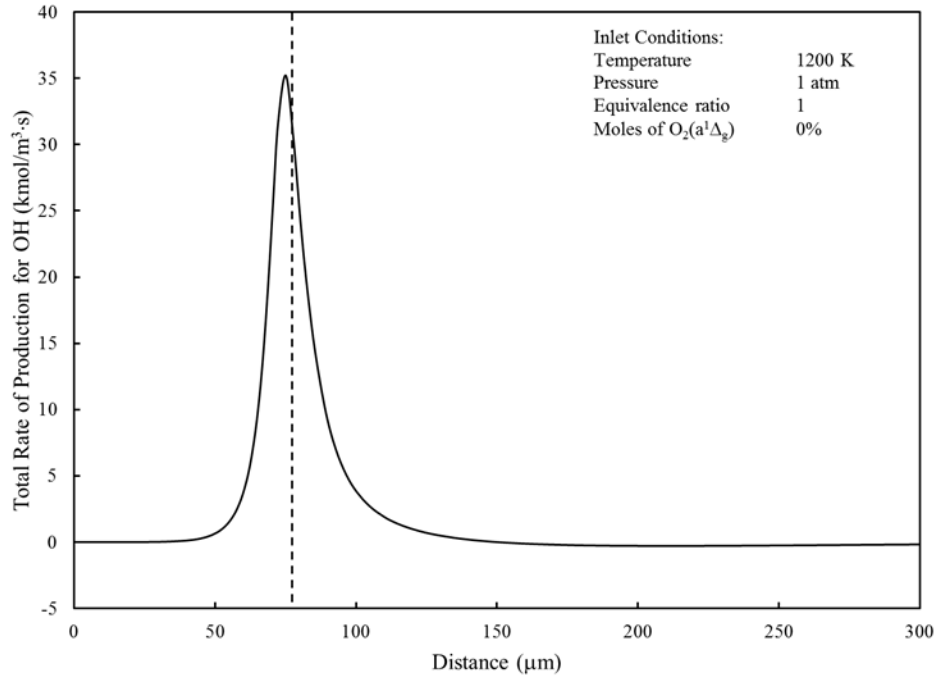


Figure 4.24 Total rate of production of OH for 0% inlet $O_2(a^1\Delta_g)$, $\Phi = 1$, and $T_{in} = 1200$ K

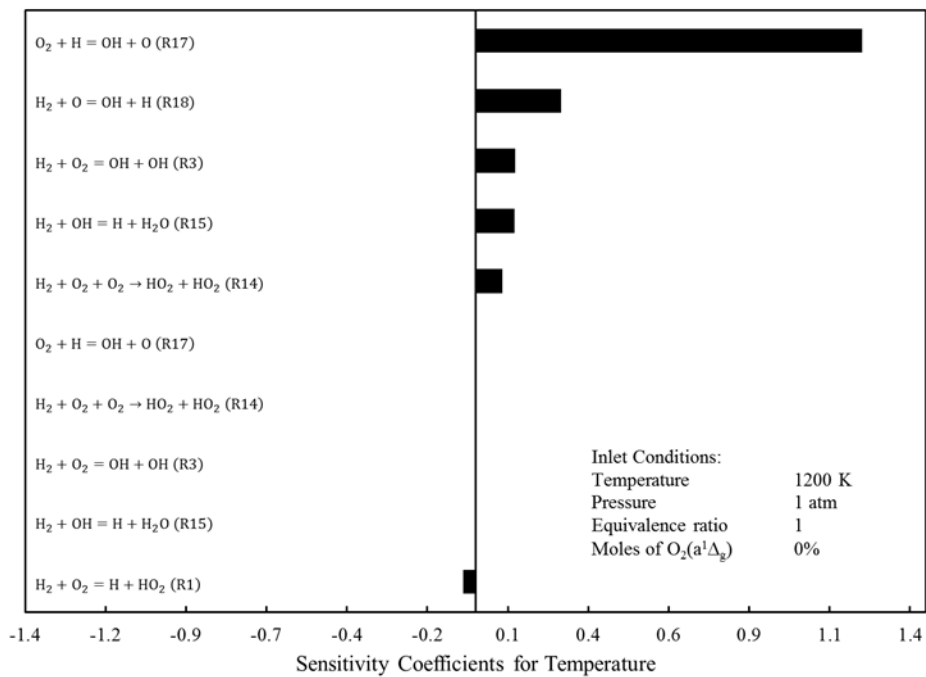


Figure 4.25 Global sensitivity analysis of temperature for 0% inlet $O_2(a^1\Delta_g)$, $\Phi = 1$, and $T_{in} = 1200$ K

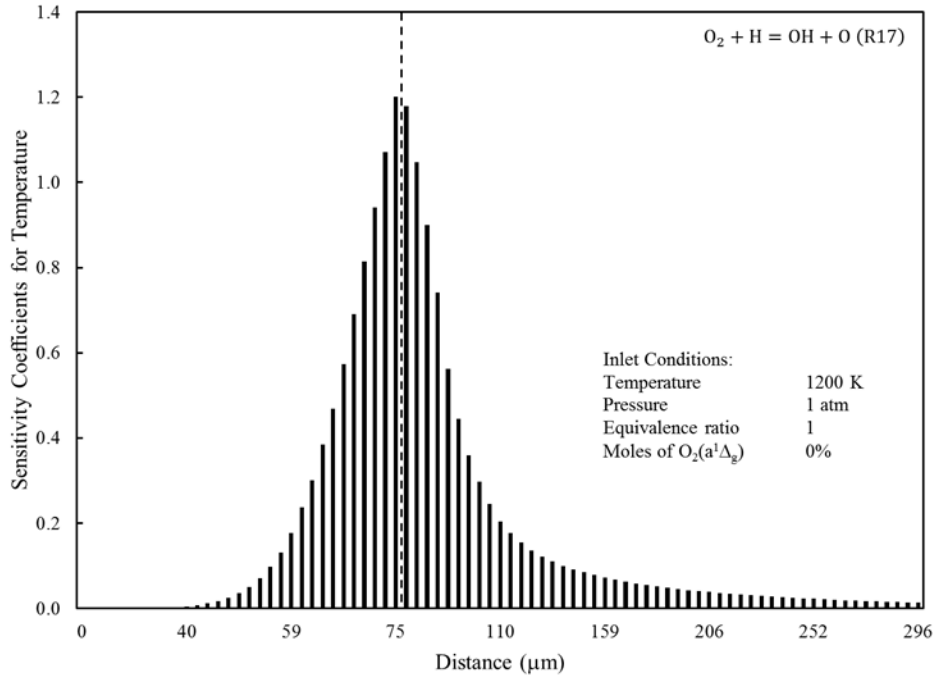


Figure 4.26 Local sensitivity analysis of temperature for 0% inlet $O_2(a^1\Delta_g)$, $\Phi = 1$, and $T_{in} = 1200$ K

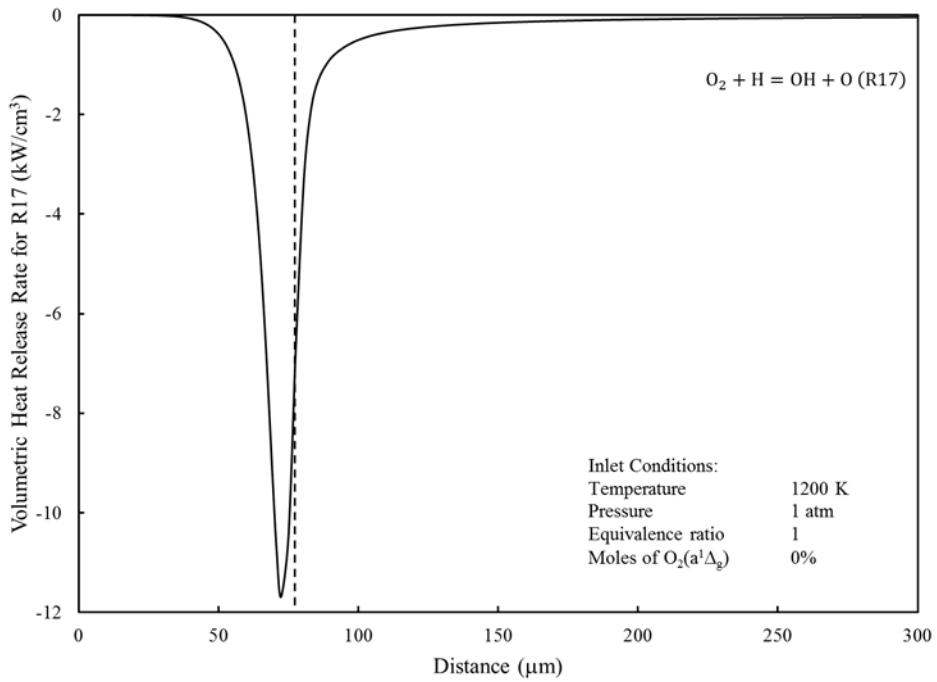


Figure 4.27 Volumetric heat release rate for R17 for 0% inlet $O_2(a^1\Delta_g)$, $\Phi = 1$, and $T_{in} = 1200$ K

This implies that even though R17 contributes a great deal to the formation of hydroxyl, there are several other competing reactions which consume it, lending to sustained combustion. Both trends peak just before ignition.

Figure 4.25 shows the global sensitivities for temperature. Again R17 appears as the dominate reaction with the largest sensitivity coefficient, followed by R18. Figure 4.26 displays the local sensitivity coefficients for temperature, which peak at ignition.

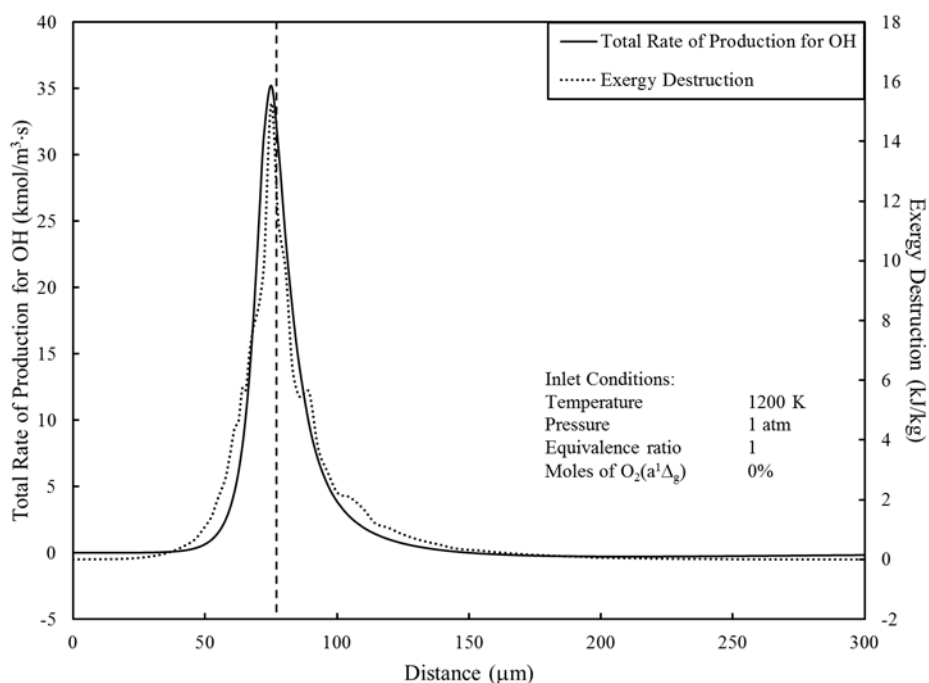


Figure 4.28 Total rate of production for OH and exergy destruction vs. distance for 0% inlet O₂(a¹Δ_g), $\Phi = 1$, and $T_{in} = 1200$ K

Figure 4.27 gives the volumetric heat release rate for R17; it implies that R17 is endothermic. The maximum rate of heat absorption occurs just before ignition. This fact will be useful later in the discussion in helping to explain trends in exergy destruction. Figure 4.28 shows the strong relationship between exergy destruction and the total rate of production for hydroxyl. This trend underscores the influence hydroxyl has on oxidation and its ability to drive

combustion. In the next section, once trends are discussed for cases where excited oxygen is included, a more complete discussion is presented.

To summarize the primary insights gained from the results and analysis in this section; R17 is indeed the dominant rate limiting reaction for the mechanism for the base case. Hydroperoxyl plays an important role initiating radical buildup in the chemical induction zone. The consumption of triplet oxygen is completely driven to R17. With the exception of hydroxyl, most sensitivity coefficients are symmetric about the ignition point; whereas, hydroxyl's maximum sensitivity occurs before ignition, this is important. R17 is an endothermic reaction, which has implications for the trends regarding molar conversion of fuel and exit temperature. Finally, trends in exergy destruction coincide almost perfectly with the total rate of production for hydroxyl. In closing, the nuances of the Moscow State University mechanism have been established for conditions associated with Model IA. In the next section this understanding will be expanded slightly to include the Model IB case of 10% singlet oxygen.

4.3.2.2 10% Inlet $O_2(a^1\Delta_g)$

From the base case, several aspects of the mechanism were established. Here

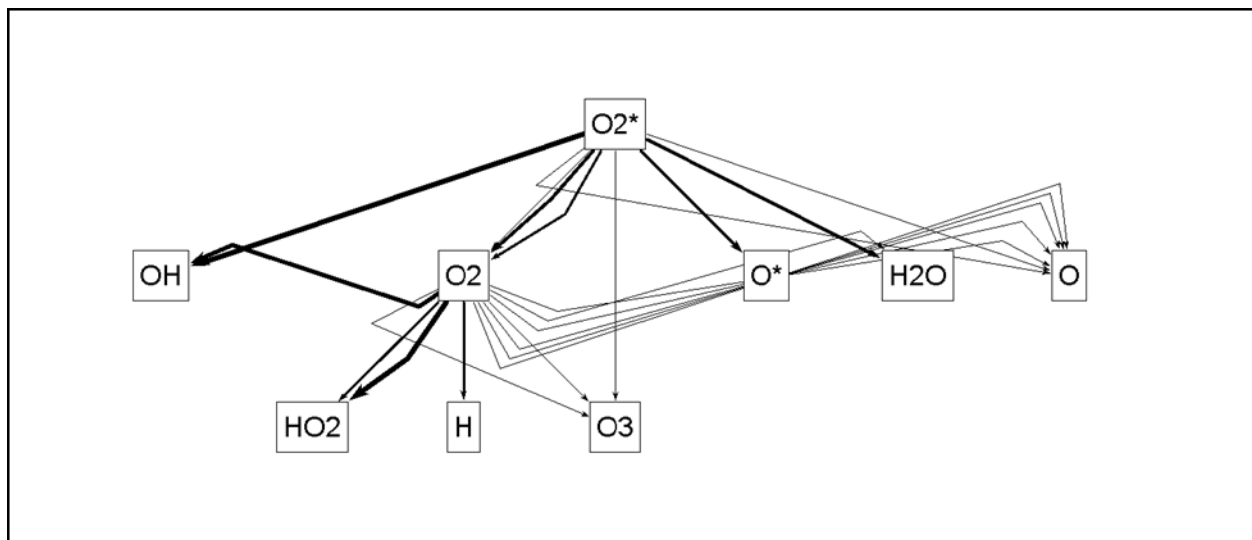


Figure 4.29 Reaction flow diagram for 10% inlet $O_2(a^1\Delta_g)$, $\Phi = 1$, and $T_{in} = 1200$ K [59]

consideration is given to gaining a fuller understanding of the mechanism kinetics when 10% singlet oxygen is introduced into the charge. Comparing Figures 4.12 and 4.29 there is a dramatic difference in the reaction flow paths indicating that excited oxygen has substantially impacted the mechanism. The presence of excited oxygen opens new pathways for the production of key radicals; for instance the pathway to electronically excited atomic oxygen was not present in Figure 4.12. There were only three meager pathways for the production of triplet atomic oxygen in Figure 4.12; however, in Figure 4.29 that number has doubled.

The moles fraction trends for the primary mechanism species in Figures 4.13 and 4.30 are analogous to what was seen in the exergy plots, with ignition occurring much sooner. However,

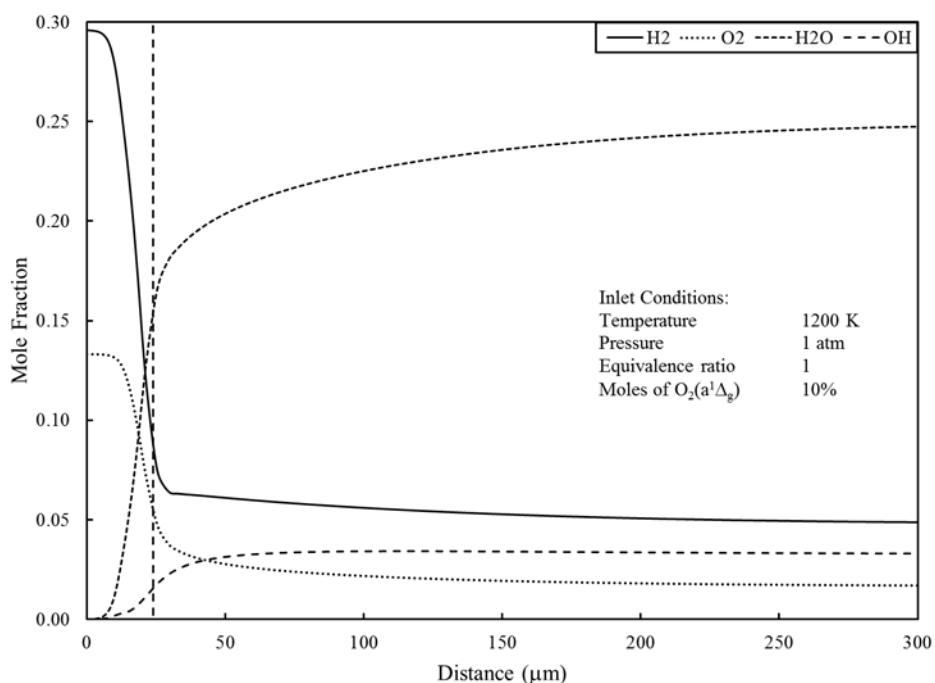


Figure 4.30 Mole fractions of primary species vs. distance for 10% inlet $O_2(a^1\Delta_g)$, $\Phi = 1$, and $T_{in} = 1200$ K

the trends for the mole fractions of the radicals and reactive species depicted in Figure 4.31 show that the slopes are much steeper than those in Figure 4.14. This is indicative of rapid radical buildup in the chemical induction zone.

In Figure 4.14, very little triple oxygen reacted in the chemical induction zone, which resulted in a relatively long ignition delay distance. In Figure 4.31 the singlet oxygen is consumed quickly, accelerating the formation of all the other reactive species. The chemical induction zone is much shorter and more active for this case.

In Figure 4.32 the temperature gradient and volumetric heat release rate are relatively unaffected by the addition of excited oxygen, except for a notable horizontal shift to the left. The magnitude of the volumetric heat release rate is virtually unchanged. A key point to note is that, even though the reaction is initiated much sooner the rate at which heat is released is effectively unchanged.

From Figure 4.33, R17 is no longer the dominant rate limiting reaction for the mechanism. In the presence of singlet oxygen, R88 assumes this role. In Figure 4.16 the largest sensitivity coefficient was associated with the formation of hydrogen peroxide. In the case of Figure 4.33, the largest sensitivity coefficient corresponds to the consumption of singlet oxygen, whose importance during induction spans both the chemical and thermal zones. The trend shown in Figure 4.34 is similar to the one presented for its triplet counterpart in Figure 4.17. However, the major difference is that the sensitivity coefficients for the excited case are approximately double in magnitude.

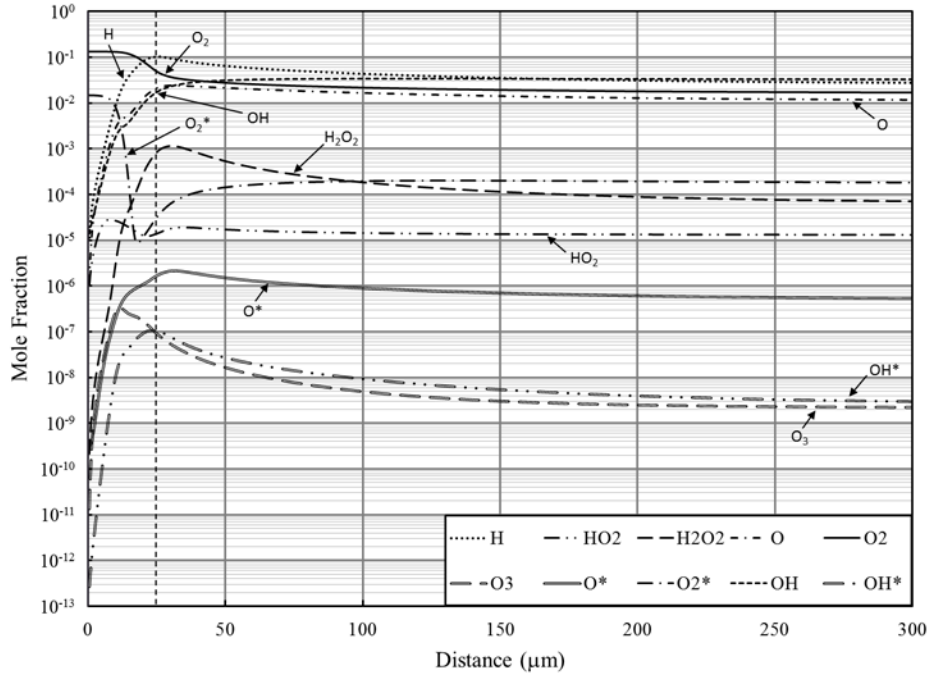


Figure 4.31 Mole fractions of radicals and chain carriers vs. distance for 10% inlet $\text{O}_2(a^1\Delta_g)$, $\Phi = 1$, and $T_{\text{in}} = 1200 \text{ K}$

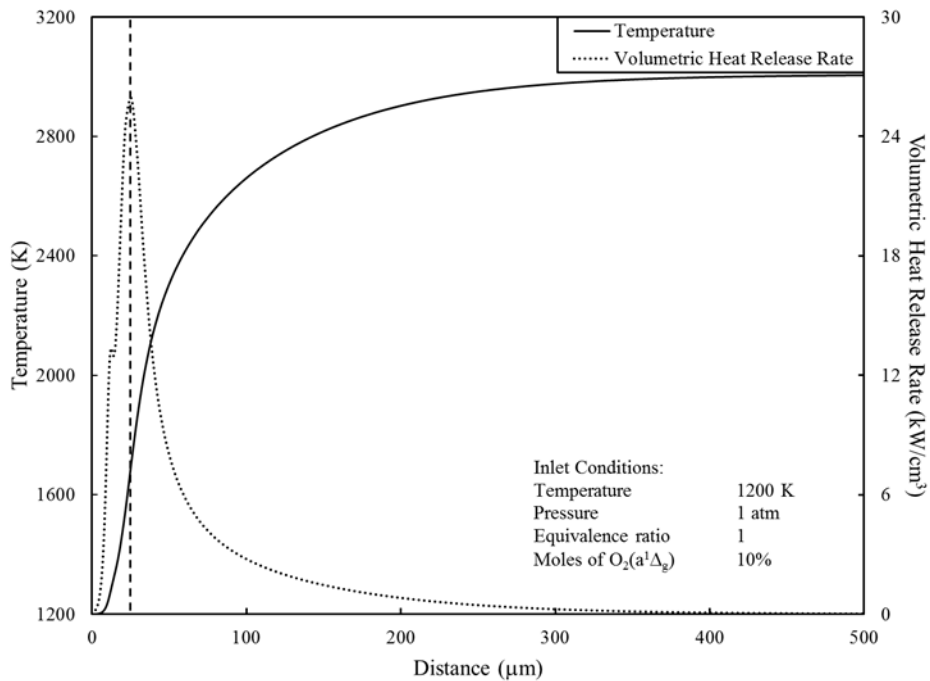


Figure 4.32 Temperature and volumetric heat release rate vs. distance for 10% inlet $\text{O}_2(a^1\Delta_g)$, $\Phi = 1$, and $T_{\text{in}} = 1200 \text{ K}$

The local sensitivity for singlet oxygen in Figure 4.35 is significantly different from the local sensitivity for triplet oxygen in Figure 4.18. The two primary differences are the coefficients for singlet oxygen are much larger and the maximum sensitivity occurs before ignition. Additionally, after ignition there is some formation of excited oxygen. This does not occur with R17.

Like Figures 4.19 and 4.20, Figures 4.36 and 4.37 are similar. This is attributed to the fact that R88 is the dominant reaction of all the reactions involving excited oxygen. The most notable feature for both of these plots is the maximum rate of consumption happens well before ignition.

By comparison, Figure 4.38 has the same trend as Figure 4.21, but the sensitivity coefficients are smaller by almost an order of magnitude. This implies that in the presence of excited oxygen there is not as much impedance to the formation of hydroxyl.

Figure 4.39 is very different from Figure 4.22. It has a bimodal shape with the largest peak emerging well in advance of ignition, and much earlier in the thermal zone.

The maximum rate of production of hydroxyl relative to R88 in Figure 4.40 is about a third of what it was relative to R17; however, excited oxygen composes only 10% of the oxygen in the oxidizer.

Figures 4.41 and 4.24 achieve approximately the same maximum rates of production. What differentiates them is the production which occurs associated with the first peak of Figure 4.41, which is reflected in the Figure 4.39 where the bimodal sensitivity coefficients were observed.

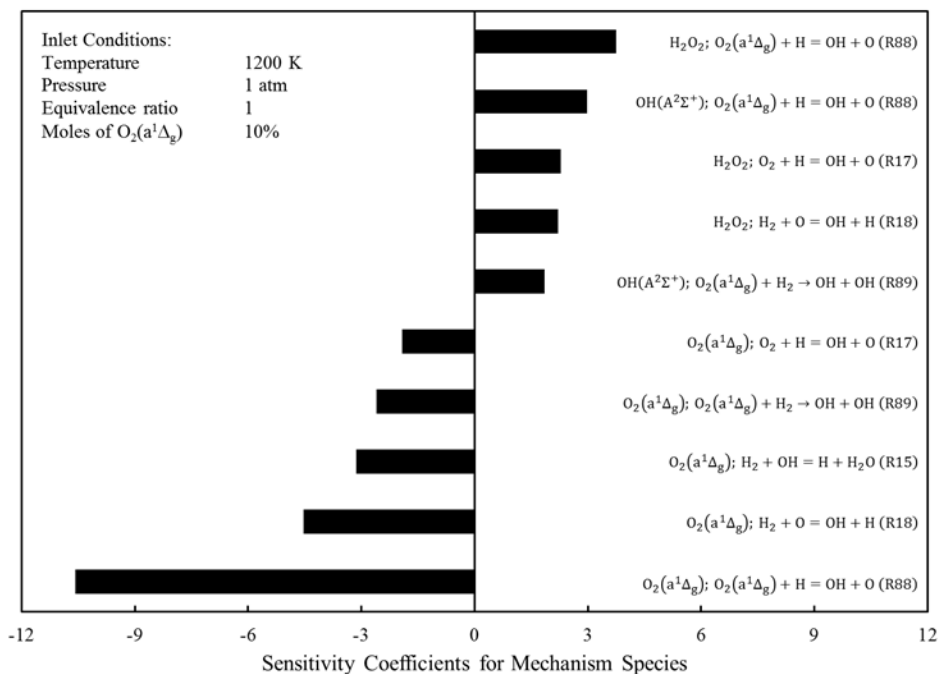


Figure 4.33 Global sensitivity analysis of the overall mechanism for 10% inlet $O_2(a^1\Delta_g)$, $\Phi = 1$, and $T_{in} = 1200$ K

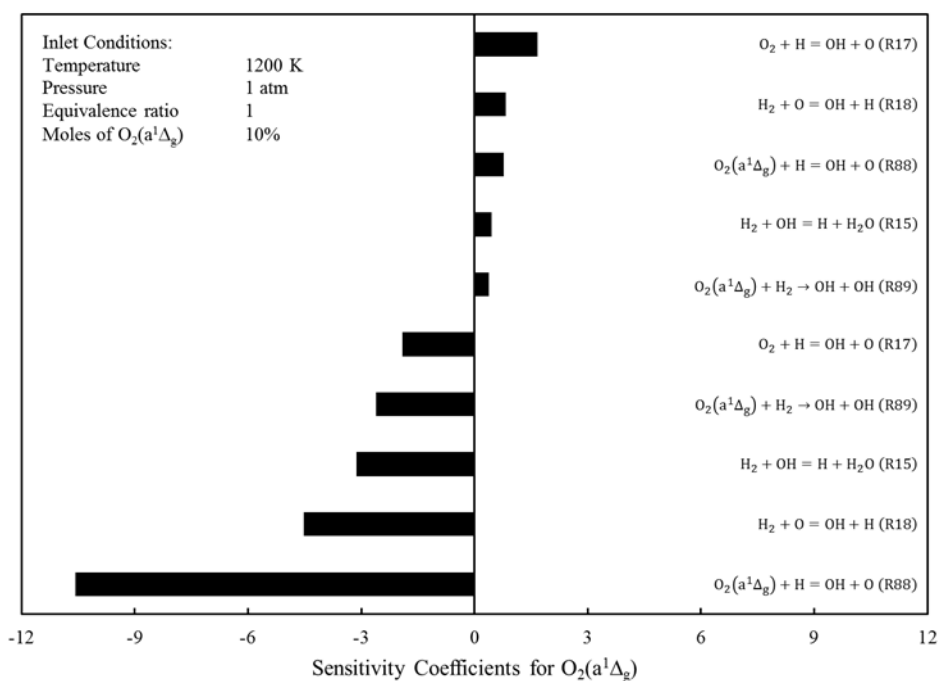


Figure 4.34 Global sensitivity analysis of $O_2(a^1\Delta_g)$ for 10% inlet $O_2(a^1\Delta_g)$, $\Phi = 1$, and $T_{in} = 1200$ K

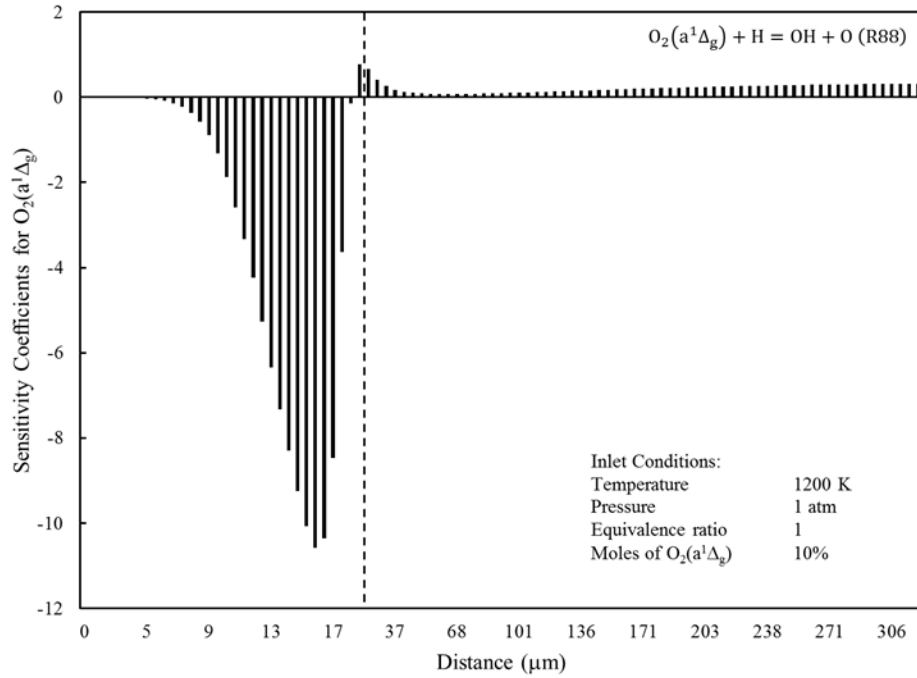


Figure 4.35 Local sensitivity analysis of $O_2(a^1\Delta_g)$ for 10% inlet $O_2(a^1\Delta_g)$, $\Phi = 1$, and $T_{in} = 1200$ K

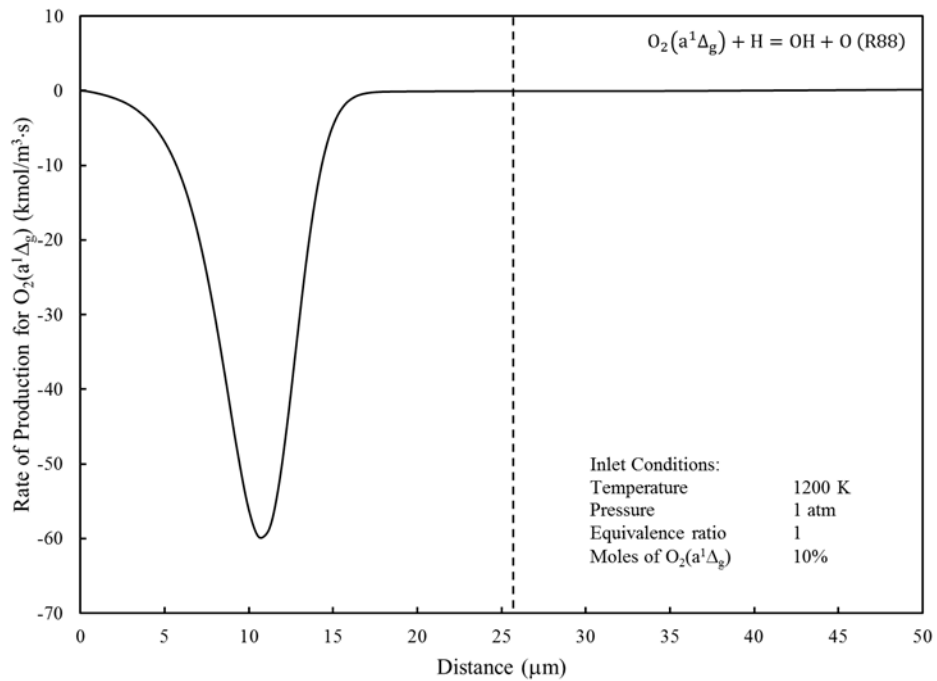


Figure 4.36 Local rate of production of $O_2(a^1\Delta_g)$ for 10% inlet $O_2(a^1\Delta_g)$, $\Phi = 1$, and $T_{in} = 1200$ K

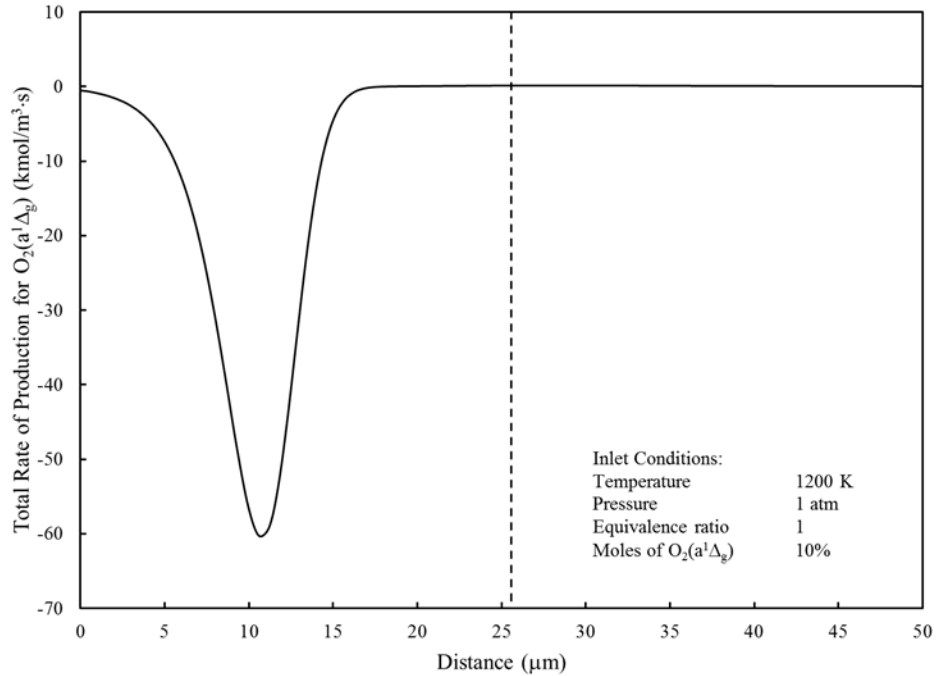


Figure 4.37 Total rate of production of $O_2(a^1\Delta_g)$ for 10% inlet $O_2(a^1\Delta_g)$, $\Phi = 1$, and $T_{in} = 1200$ K

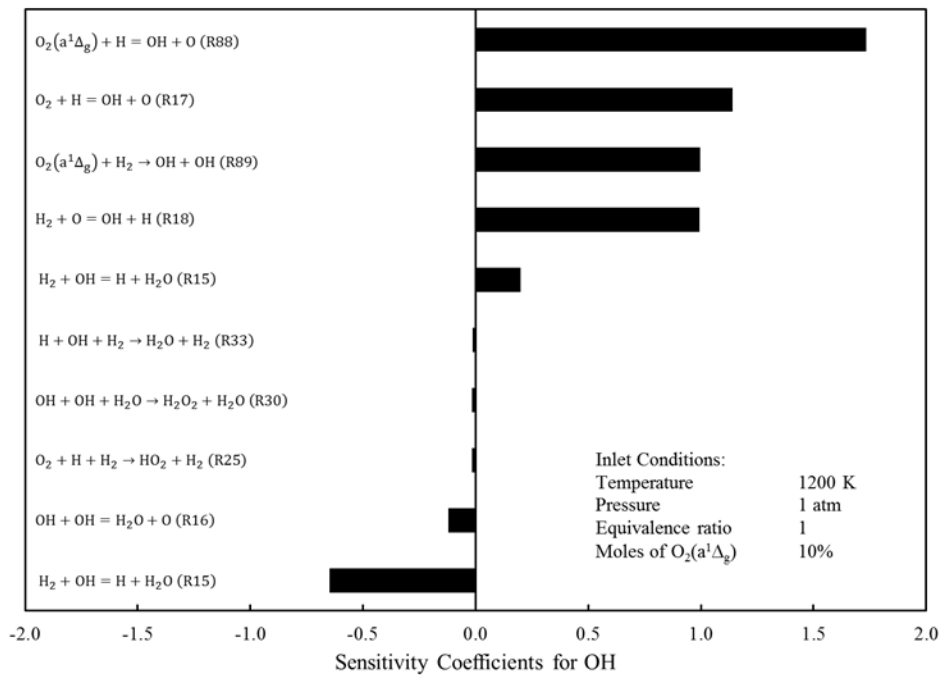


Figure 4.38 Global sensitivity analysis of OH for 10% inlet $O_2(a^1\Delta_g)$, $\Phi = 1$, and $T_{in} = 1200$ K

Figure 4.42 is the global sensitivity for temperature. Although 10% excited oxygen has been added to the charge, the temperature is still more sensitive to R17; R88 is third. The local sensitivity for temperature shown in Figure 4.43 still gives a symmetric trend around the ignition coordinate. Figure 4.44 essentially gives the same trend as Figure 4.27, with exception of the horizontal shift to the left. Figure 4.45 demonstrates again that the trend in exergy destruction corresponds with the trend of the total rate of production for hydroxyl.

There were several points of interests learned about the kinetics of the mechanism, regarding the addition of excited oxygen. The reaction pathways were affected significantly. This is illustrated with reaction path diagrams. Radical buildup in the chemical zone occurs much more rapidly, and its length is reduced significantly. A rapid increase could be observed in all of the reactive species. This is due to the immediate consumption of excited oxygen in the charge. Although the ignition delay distance is shortened, there is no real impact on the rate at which heat is released. R88 assumes the role as the dominate chain branching reaction for the mechanism, even though the excited oxygen only makes up 10% of the incoming oxygen. All sensitivity coefficients and rates of production achieved their maximums before ignition, with the exception of temperature and the total rate of production of hydroxyl. Temperature is still more sensitive to R17. The sensitivity coefficients for the rate of formation of hydroxyl are approximately an order of magnitude less than the base case.

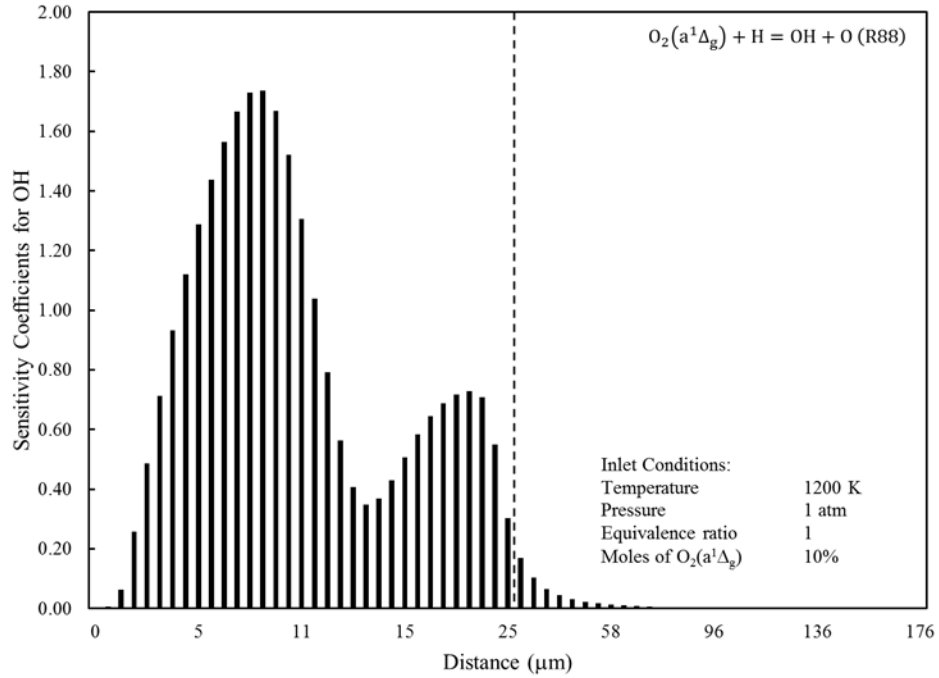


Figure 4.39 Local sensitivity analysis of OH for 10% inlet $\text{O}_2(\text{a}^1\Delta_g)$, $\Phi = 1$, and $T_{\text{in}} = 1200 \text{ K}$

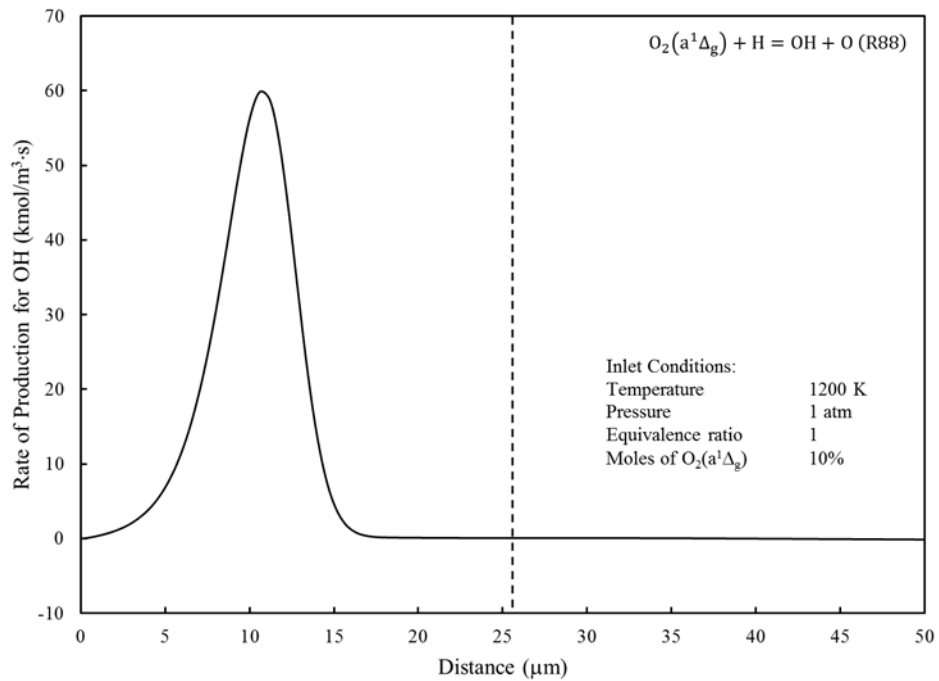


Figure 4.40 Local rate of production of OH for 10% inlet $\text{O}_2(\text{a}^1\Delta_g)$, $\Phi = 1$, and $T_{\text{in}} = 1200 \text{ K}$

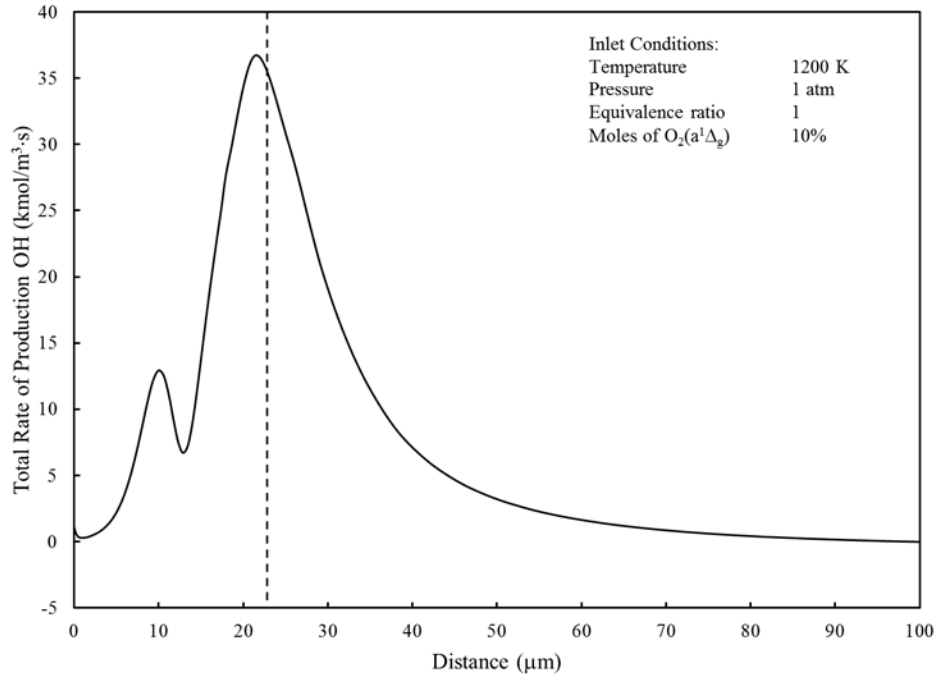


Figure 4.41 Total rate of production of OH for 10% inlet $O_2(a^1\Delta_g)$, $\Phi = 1$, and $T_{in} = 1200$ K

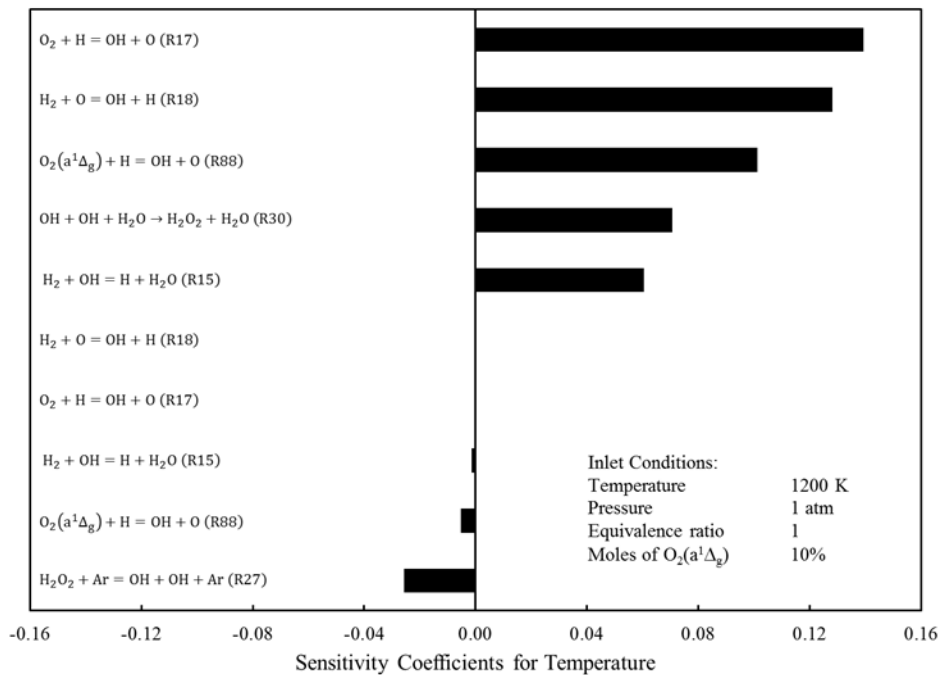


Figure 4.42 Global sensitivity analysis of temperature for 10% inlet $O_2(a^1\Delta_g)$, $\Phi = 1$, and $T_{in} = 1200$ K

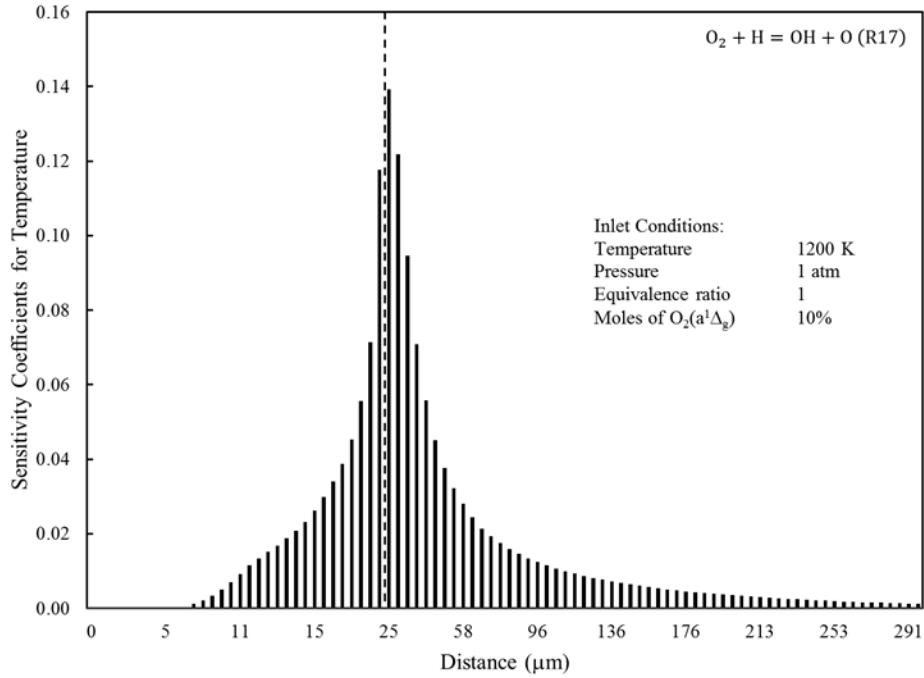


Figure 4.43 Local sensitivity analysis of temperature for 10% inlet $O_2(a^1\Delta_g)$, $\Phi = 1$, and $T_{in} = 1200$ K

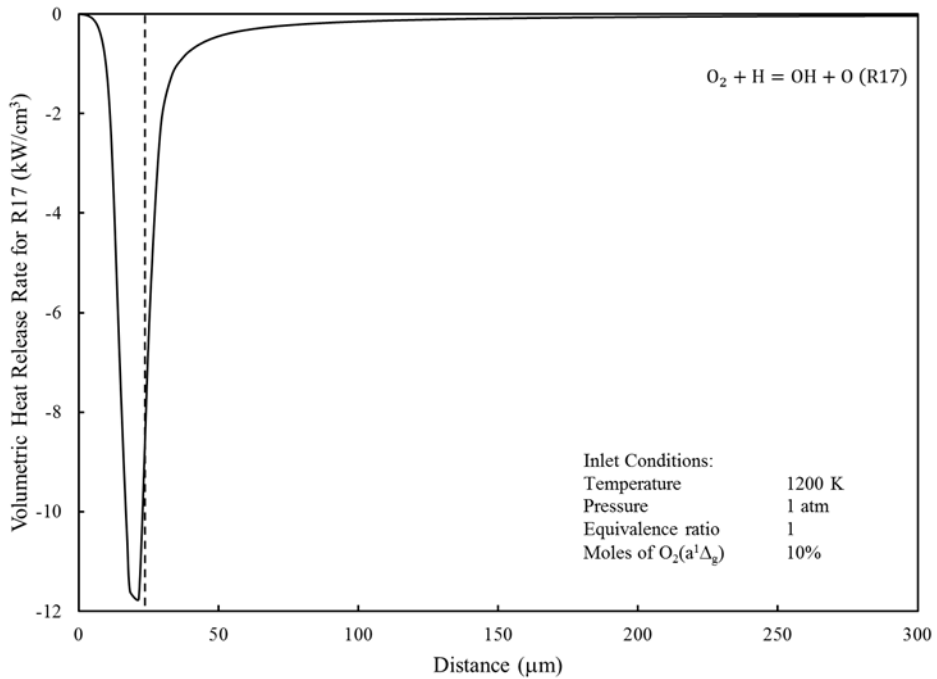


Figure 4.44 Volumetric heat release rate for R17 for 10% inlet $O_2(a^1\Delta_g)$, $\Phi = 1$, and $T_{in} = 1200$ K

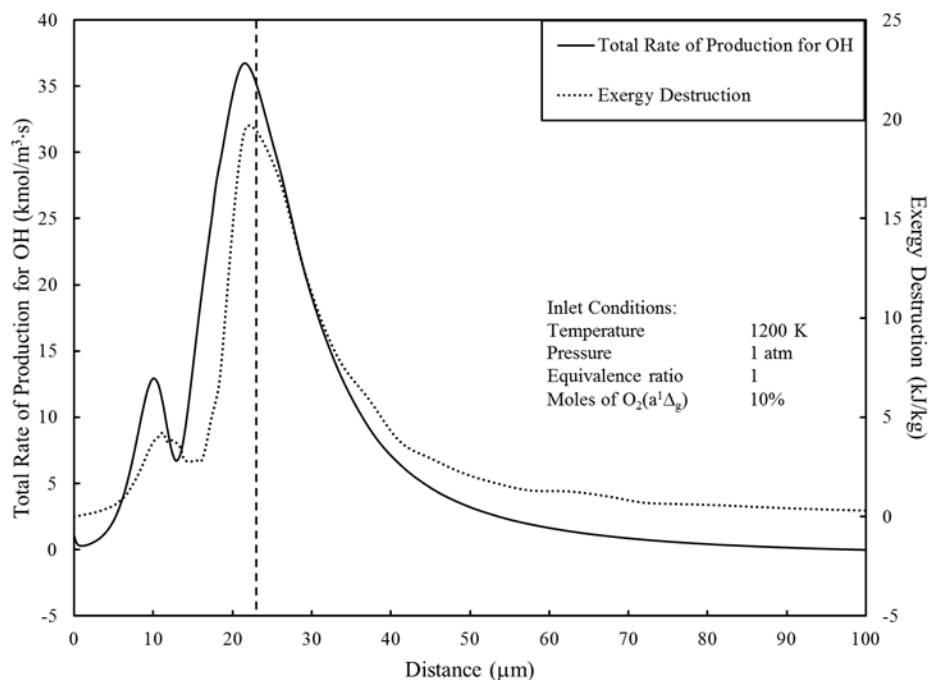


Figure 4.45 Total rate of production for OH and exergy destruction vs. distance for 10% inlet $O_2(a^1\Delta_g)$, $\Phi = 1$, and $T_{in} = 1200$ K

4.3.2.3 25% Inlet $O_2(a^1\Delta_g)$

With excited oxygen composing 25% of the oxygen in the charge there has been very little change in the available reaction flow paths; however, it is expected the kinetics will change.

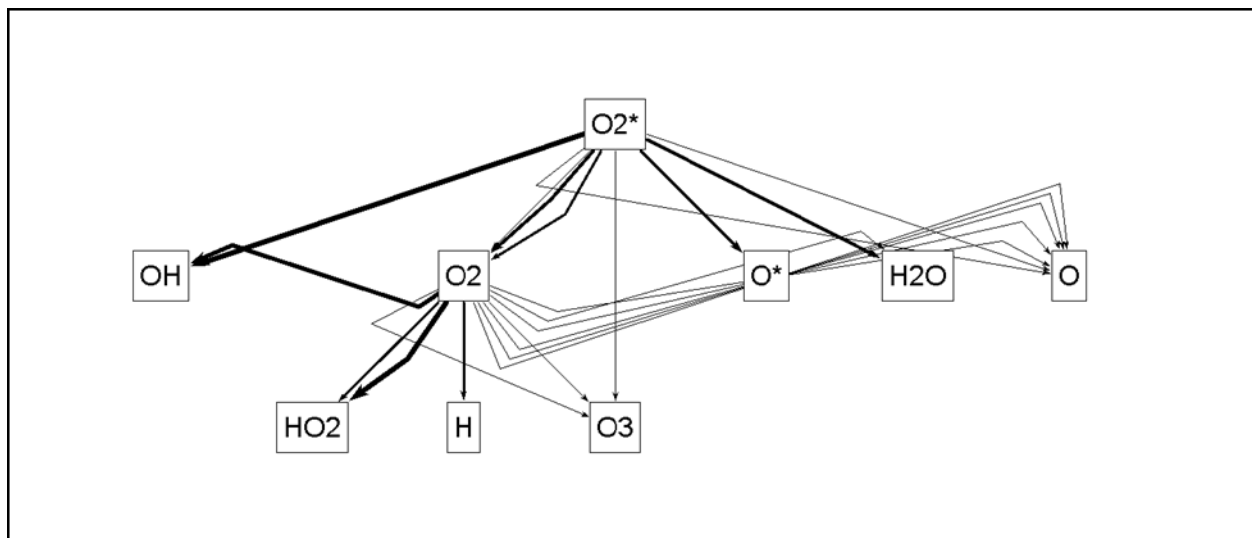


Figure 4.46 Reaction flow diagram for 25% inlet $O_2(a^1\Delta_g)$, $\Phi = 1$, and $T_{in} = 1200$ K

Figure 4.47 is drastically different from Figures 4.13 and 4.30. In the previous two cases the bulk of the primary species were consumed before ignition, but here the consumption occurs after ignition. Additionally, the ignition delay distance has decreased even further.

A similar trend is seen in Figure 4.48 when compared to Figure 4.31; in Figure 4.31 most of the excited oxygen is consumed before ignition late in the thermal induction zone. However, in Figure 4.48 the vast majority of the excited oxygen is consumed after ignition, in the primary reaction zone. The trends in the species mole fractions between the two graphs are comparable, but ignition occurs much sooner, and at a much lower temperature, seen in Figure 4.49. This is directly related to the reduction in energy required to sustain various endothermic reactions.

In contrast to Figures 4.15 and 4.32, the contour of the volumetric heat release rate curve in Figure 4.49 has been altered considerably. In the previous two figures, the differences in the heat release rates before and after ignition were more symmetric, with the rates in the primary reaction zone being slightly greater. However, in Figure 4.49 the heat release rates in the reaction zone are notably favored. There is also a significant reduction of the overall induction zone, but with the thermal zone being reduced significantly when compared to Figure 4.32. As was the case for Figure 4.33, R88 is the dominant chain branching reaction when looking at the overall mechanism, the same is true in Figure 4.50. The sensitivity coefficients have approximately the same magnitudes. The global sensitivity coefficients for excited oxygen in Figure 4.51 also exhibit a similar trend as in Figure 4.34, the magnitudes of the sensitivity coefficients are similar and R88 is still the dominant chain branching reaction with respect to consumption.

Comparing Figure 4.52 and Figure 4.35, the trends are similar as well as the magnitudes; however, in Figure 4.52 a horizontal shift of the sensitivity coefficients to the right of ignition has occurred. This trend is instrumental in developing a deeper understanding of the exergy analysis data.

Figure 4.53 shows a large increase in the local rate of consumption when compared to Figure 4.36; hence, lending itself to the reduction in ignition delay distance. The magnitudes exceed the consumption rates for ground state oxygen shown in Figure 4.19, the base case, which is significant because the rate of production is related to the concentration of species involved in the reaction. In all cases there are significantly larger quantities of triplet oxygen compared with singlet oxygen. For singlet oxygen's rate of consumption to exceed that of triplet oxygen speaks to its enhanced reactive qualities.

From Figure 4.53 it is apparent that R88 drives the trend observed in Figure 4.54, and is the dominant contributor to the overall consumption of excited oxygen. Figure 4.55 shows hydroxyl is still most sensitive to R88. Figure 4.56 exhibits a similar bimodal shape as Figure 4.39; however, a pronounced horizontal shift to the right of the point ignition has occurred. This shift supports the concept that less reaction is occurring in the induction zone with increasing amounts of singlet oxygen, and is being pushed into the primary reaction zone. The magnitudes of the sensitivity coefficients in both graphs are the same order.

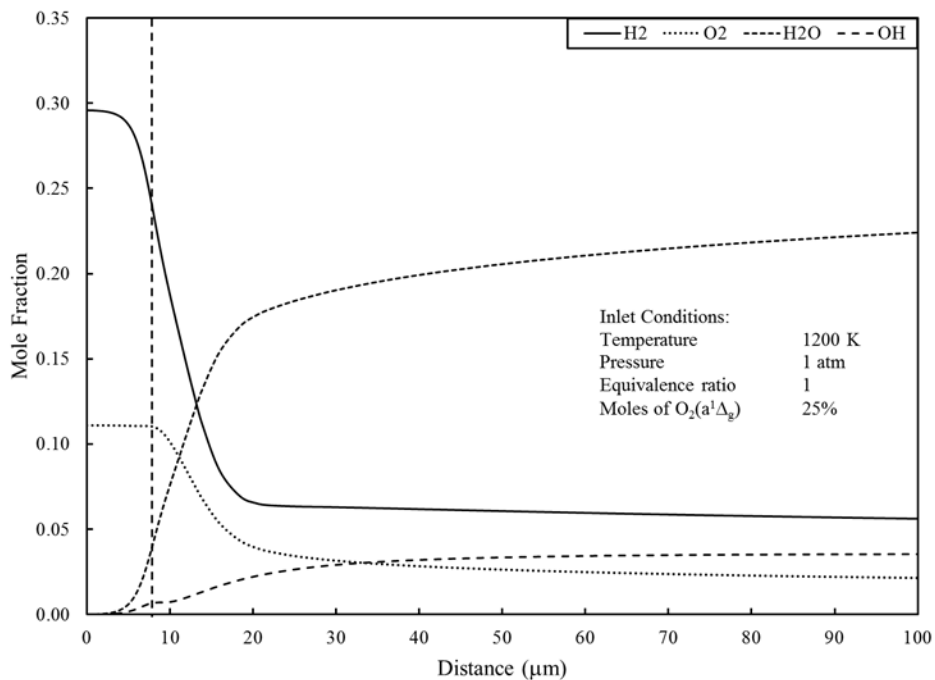


Figure 4.47 Mole fractions of primary species vs. distance for 25% inlet $O_2(a^1\Delta_g)$, $\Phi = 1$, and $T_{in} = 1200$ K

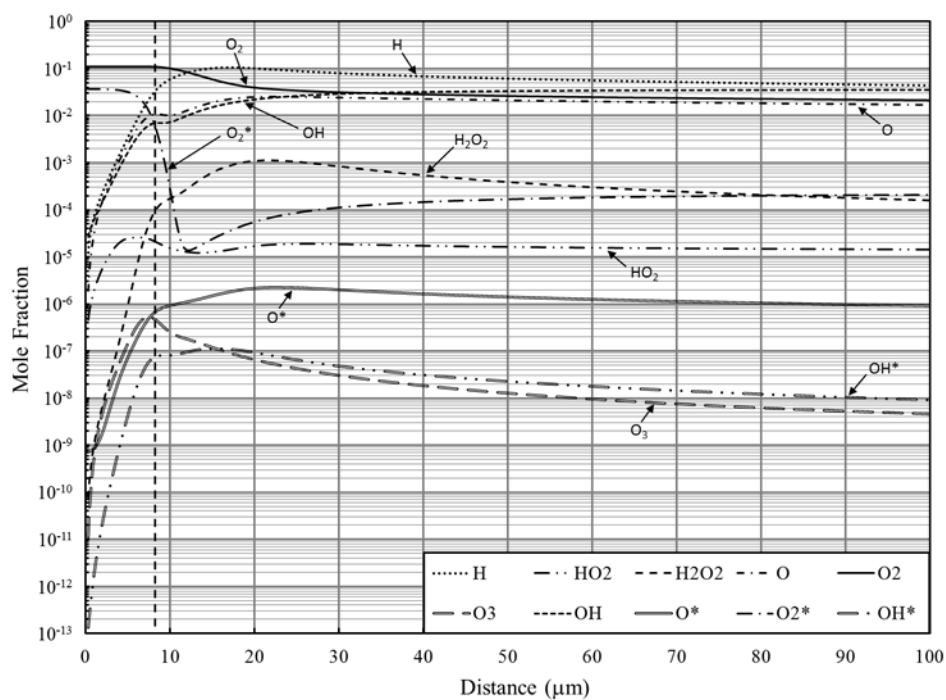


Figure 4.48 Mole fractions of radicals and chain carriers vs. distance for 25% inlet $O_2(a^1\Delta_g)$, $\Phi = 1$, and $T_{in} = 1200$ K

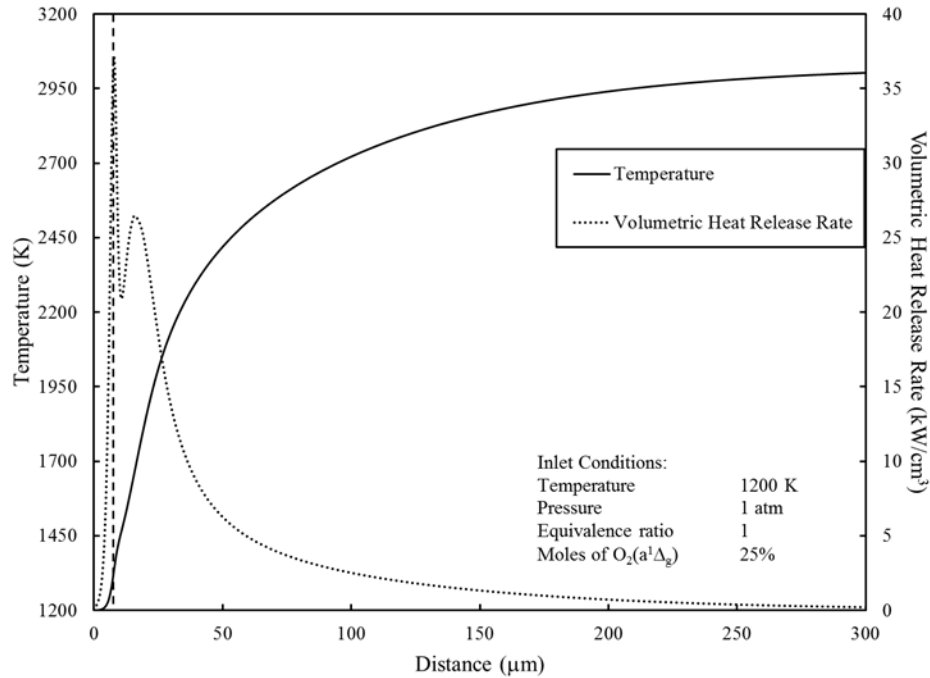


Figure 4.49 Temperature and volumetric heat release rate vs. distance for 25% inlet $O_2(a^1\Delta_g)$, $\Phi = 1$, and $T_{in} = 1200$ K

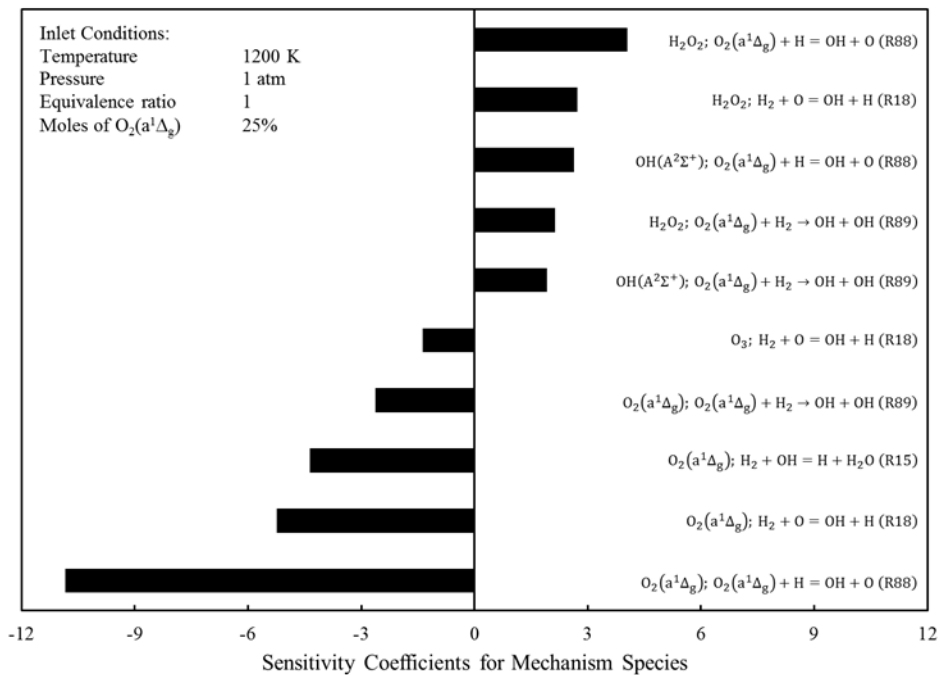


Figure 4.50 Global sensitivity analysis of the overall mechanism for 25% inlet $O_2(a^1\Delta_g)$, $\Phi = 1$, and $T_{in} = 1200$ K

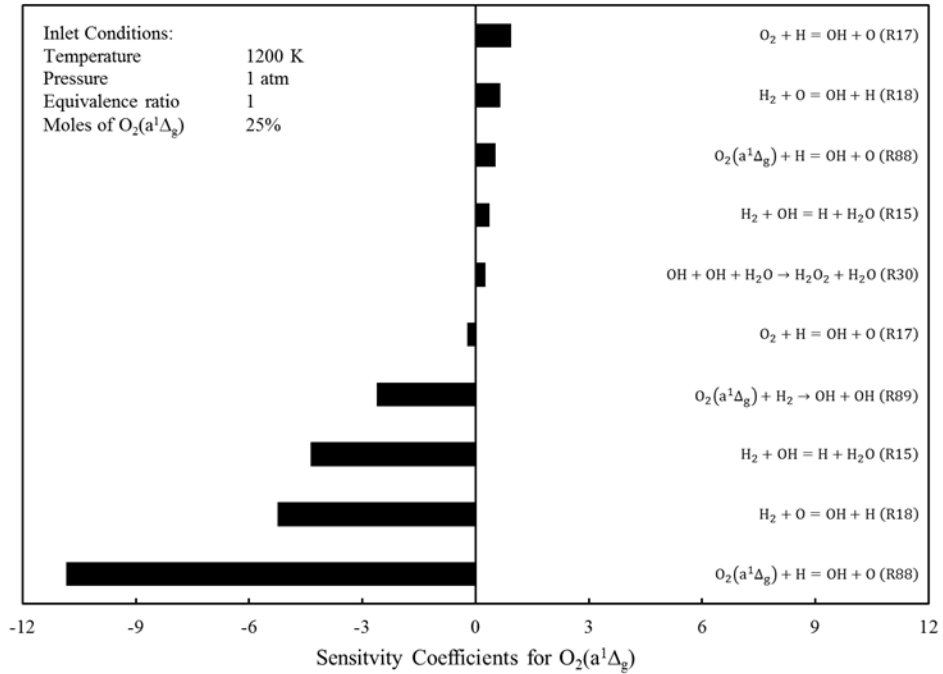


Figure 4.51 Global sensitivity analysis of $O_2(a^1\Delta_g)$ for 25% inlet $O_2(a^1\Delta_g)$, $\Phi = 1$, and $T_{in} = 1200$ K

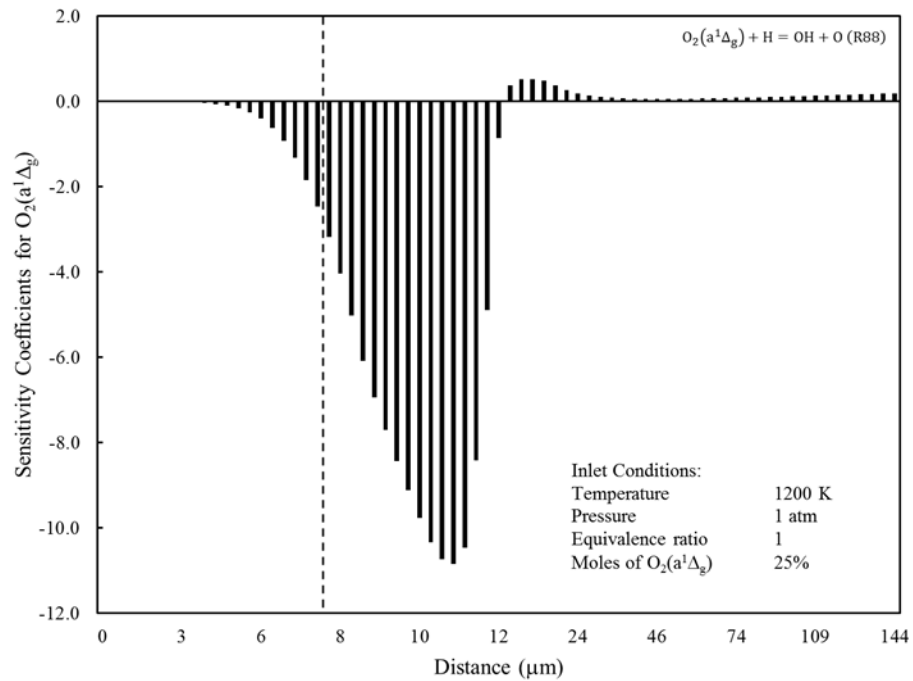


Figure 4.52 Local sensitivity analysis of $O_2(a^1\Delta_g)$ for 25% inlet $O_2(a^1\Delta_g)$, $\Phi = 1$, and $T_{in} = 1200$ K

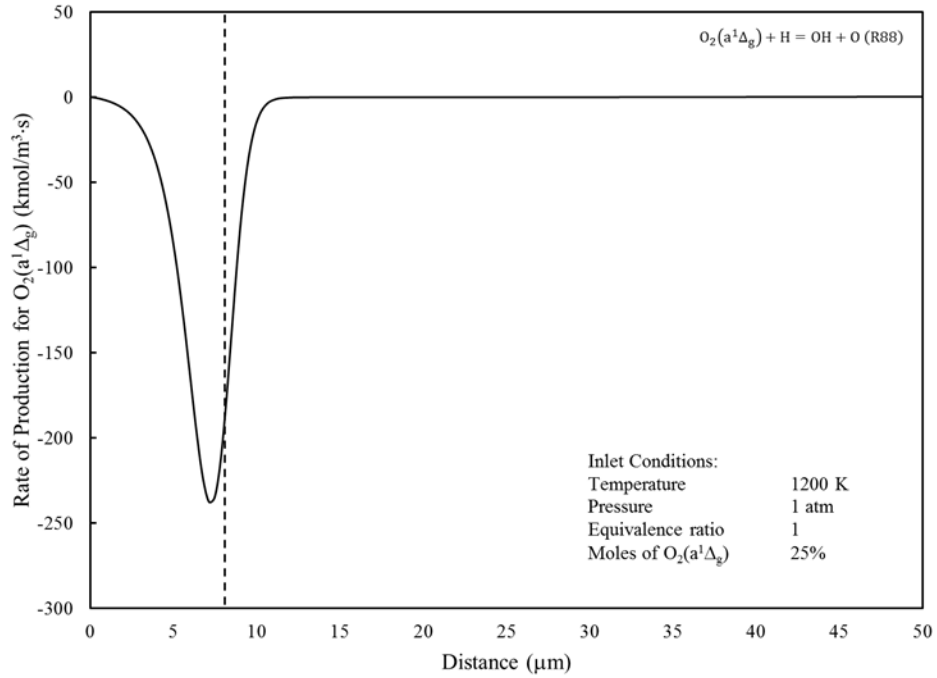


Figure 4.53 Local rate of production of $O_2(a^1\Delta_g)$ for 25% inlet $O_2(a^1\Delta_g)$, $\Phi = 1$, and $T_{in} = 1200$ K

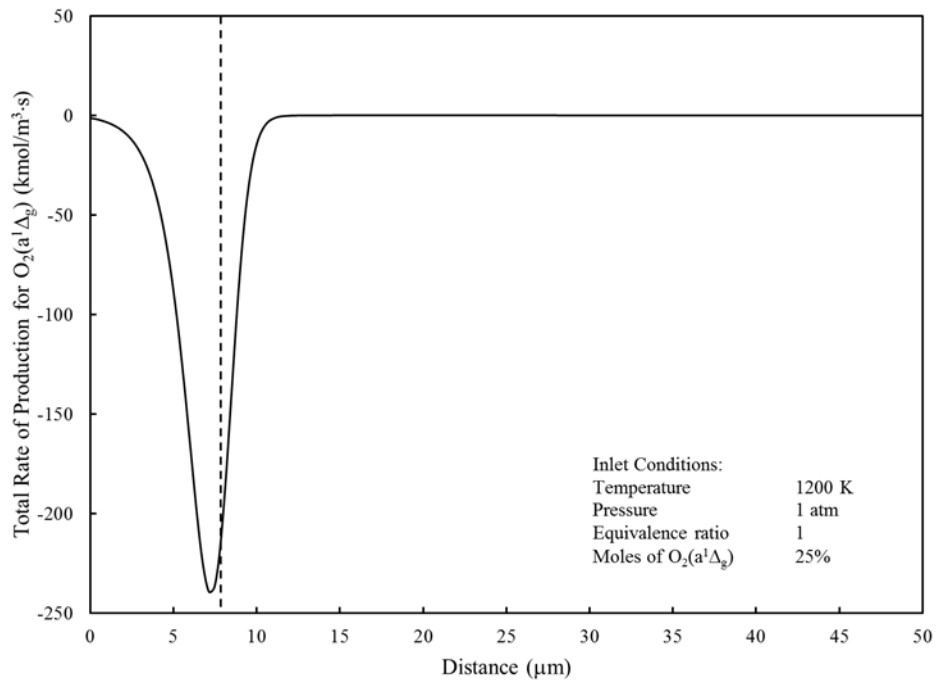


Figure 4.54 Total rate of production of $O_2(a^1\Delta_g)$ for 25% inlet $O_2(a^1\Delta_g)$, $\Phi = 1$, and $T_{in} = 1200$ K

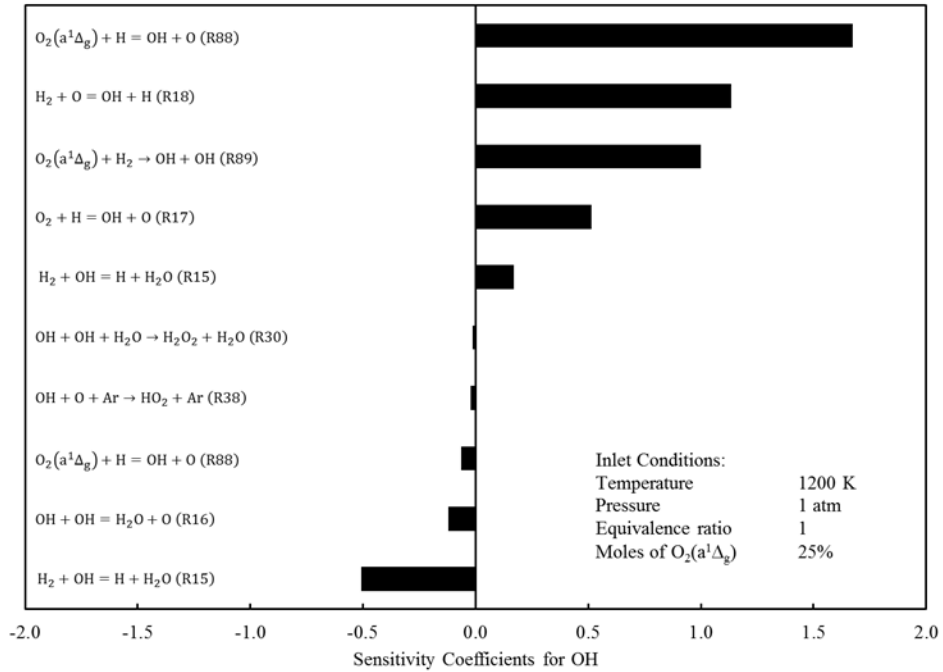


Figure 4.55 Global sensitivity analysis of OH for 25% inlet $O_2(a^1\Delta_g)$, $\Phi = 1$, and $T_{in} = 1200$ K

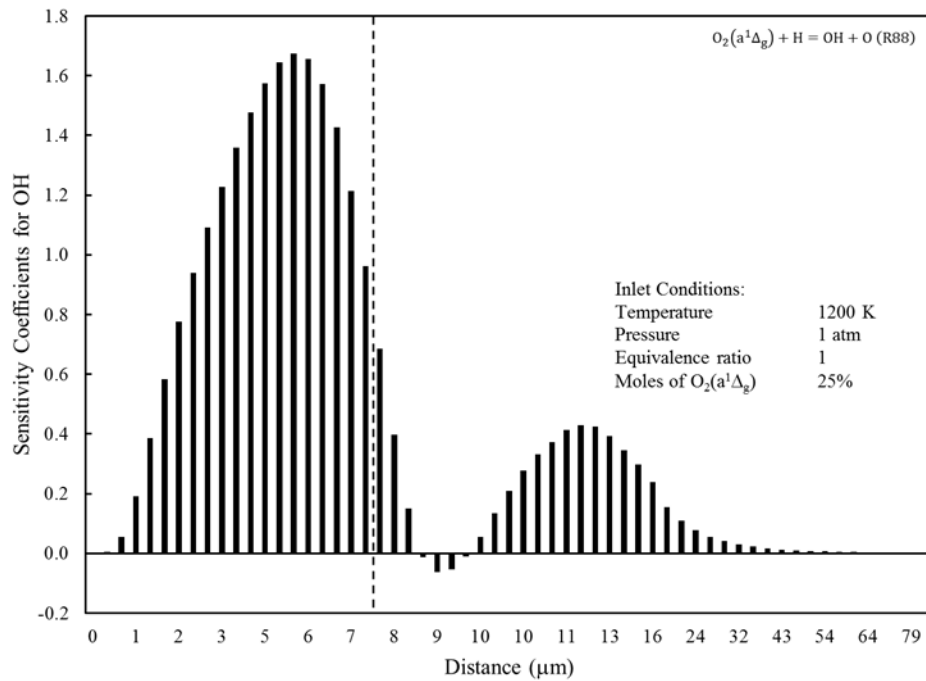


Figure 4.56 Local sensitivity analysis of OH for 25% inlet $O_2(a^1\Delta_g)$, $\Phi = 1$, and $T_{in} = 1200$ K

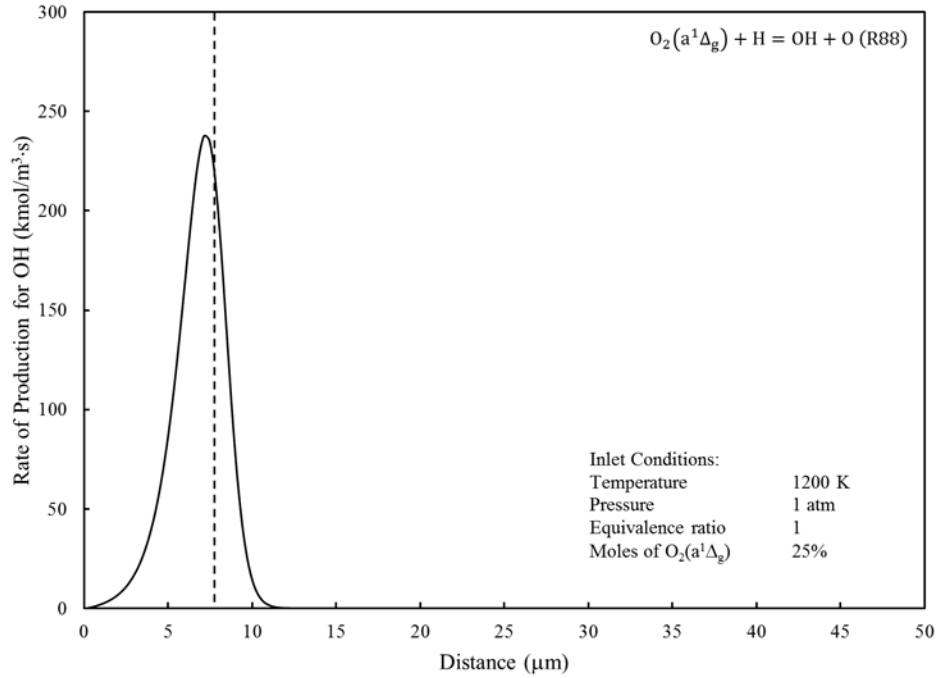


Figure 4.57 Local rate of production of OH for 25% inlet $O_2(a^1\Delta_g)$, $\Phi = 1$, and $T_{in} = 1200$ K

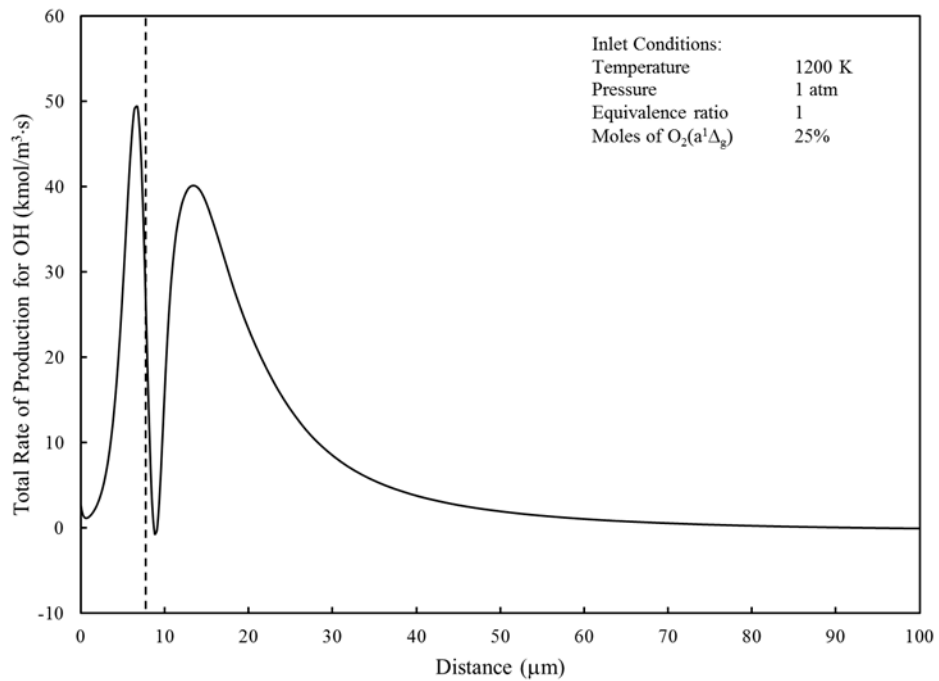


Figure 4.58 Total rate of production of OH for 25% inlet $O_2(a^1\Delta_g)$, $\Phi = 1$, and $T_{in} = 1200$ K

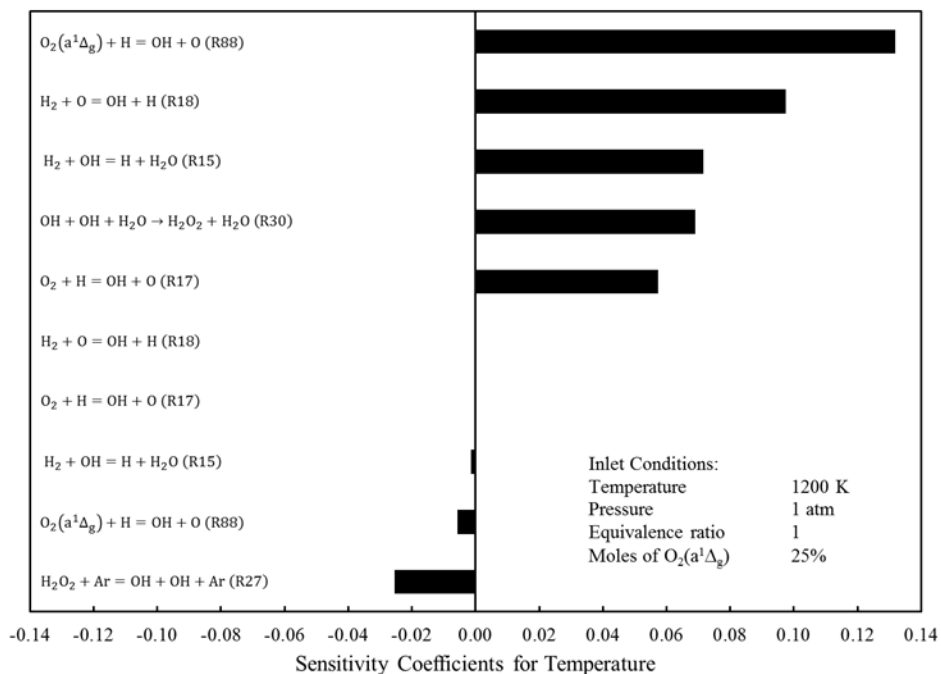


Figure 4.59 Global sensitivity analysis of temperature for 25% inlet $O_2(a^1\Delta_g)$, $\Phi = 1$, and $T_{in} = 1200$ K

The rate of production of hydroxyl shown in Figure 4.57 greatly exceeds the rates displayed in Figure 4.40. This can be traced back to the substantial increase in the rate of consumption experienced in Figure 4.54 for singlet oxygen over the rates for the 10% case. The maximum still occurs near ignition. The total rate of production of hydroxyl shown in Figure 4.58 takes on a bimodal shape as well. The onset of this occurred in Figure 4.41. The primary difference between Figures 4.58 and 4.41 is that a bigger portion of the larger rates of hydroxyl production now occur after ignition.

There has been enough excited oxygen introduced in to the process that now temperature is most sensitive to R88 as shown in Figure 4.59. For the 10% case, represented in Figure 4.42, temperature was still more sensitive to reaction R17. Even more interesting is the trend in the local distribution of the sensitivity coefficients given in Figure 4.60. Previously, they were clustered symmetrically around the ignition coordinate. However, they are no longer clustered

about the ignition coordinate and have also assumed a bimodal distribution, which is shifted to the right of ignition. They are still close in magnitude relative to those in Figure 4.42.

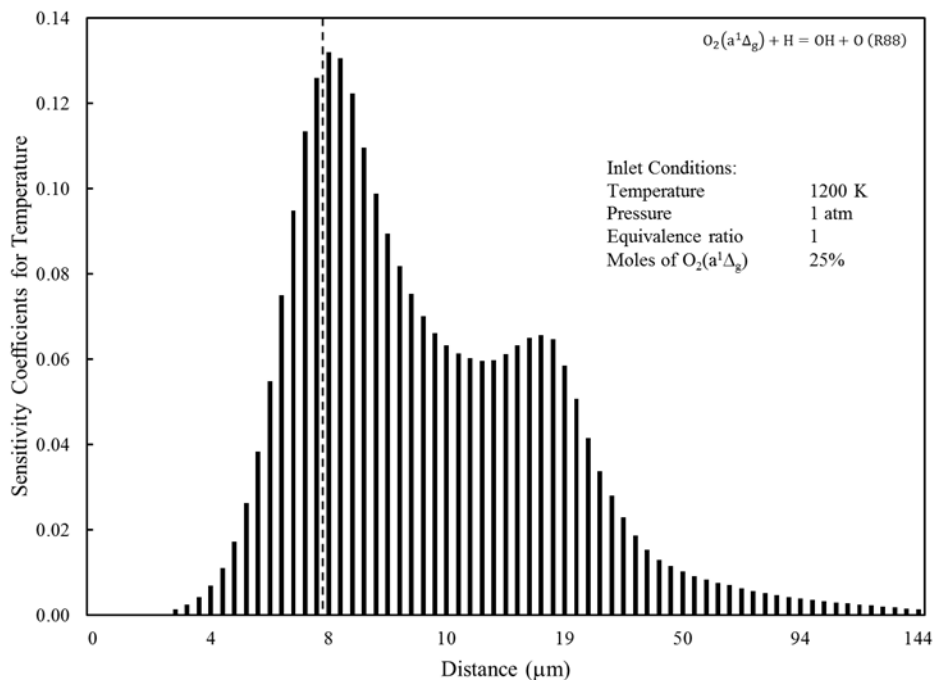


Figure 4.60 Local sensitivity analysis of temperature for 25% inlet $O_2(a^1\Delta_g)$, $\Phi = 1$, and $T_{in} = 1200$ K

Figure 4.61 shows the volumetric heat release rate for R88 along the reactor; unlike R17 it is exothermic. Figure 4.62 shows the same trend as the previous two other cases with regard to exergy destruction being closely related to the rate of production of hydroxyl. Just like most of the other trends for the 25% case, a larger fraction of the exergy destruction now occurs after ignition. This is explained in more detail in the chapter summary.

Figure 4.63 provides a direct comparison between R17 and R88. Their respective natures are apparent. As mentioned previously, R17 is endothermic and for this case is more active after ignition; whereas, R88 is exothermic and more active near ignition. Figure 4.63 provides direct insight into the rate at which energy needs to be provided to sustain R17. Figure 4.64 provides

additional information on the relationship between hydroxyl and the addition of singlet oxygen. As more singlet oxygen is added, the amount of hydroxyl increases as well as the rate of its production.

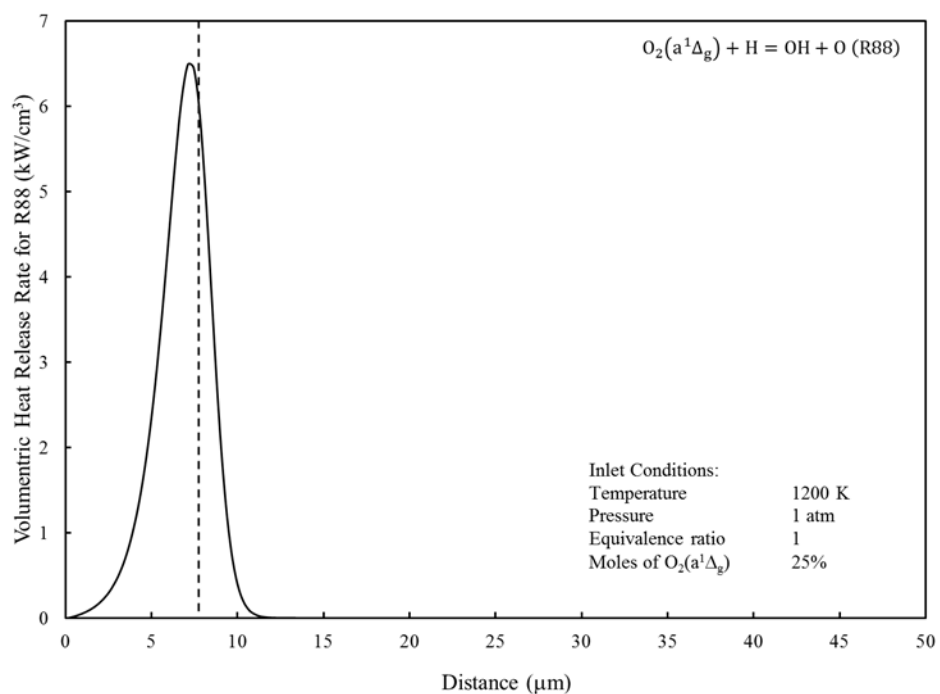


Figure 4.61 Volumetric heat release rate for R88 for 25% inlet $O_2(a^1\Delta_g)$, $\Phi = 1$, and $T_{in} = 1200$ K

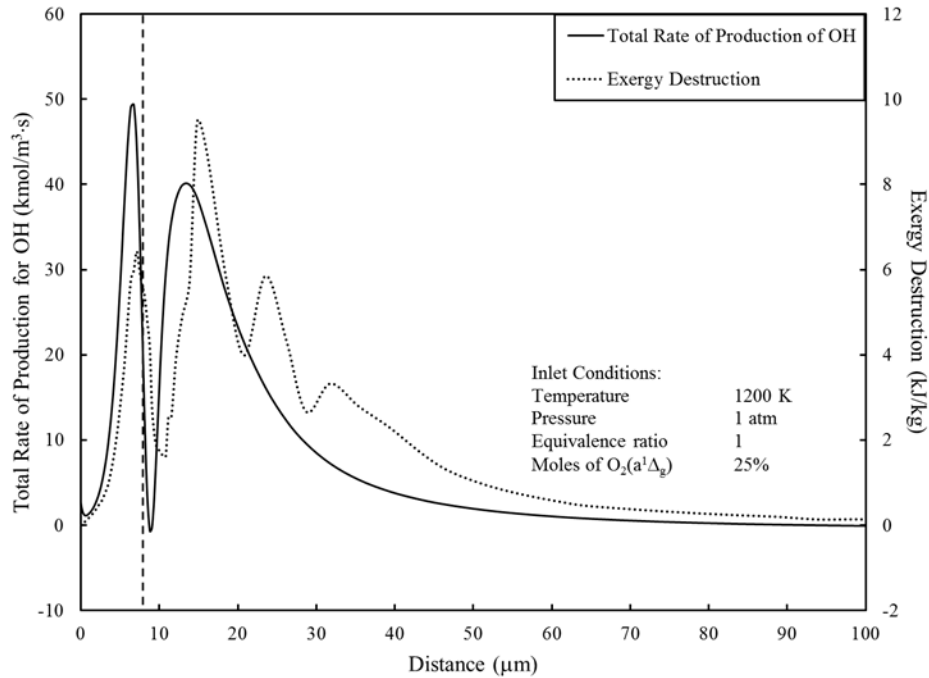


Figure 4.62 Total rate of production for OH and exergy destruction vs. distance for 25% inlet $O_2(a^1\Delta_g)$, $\Phi = 1$, and $T_{in} = 1200$ K

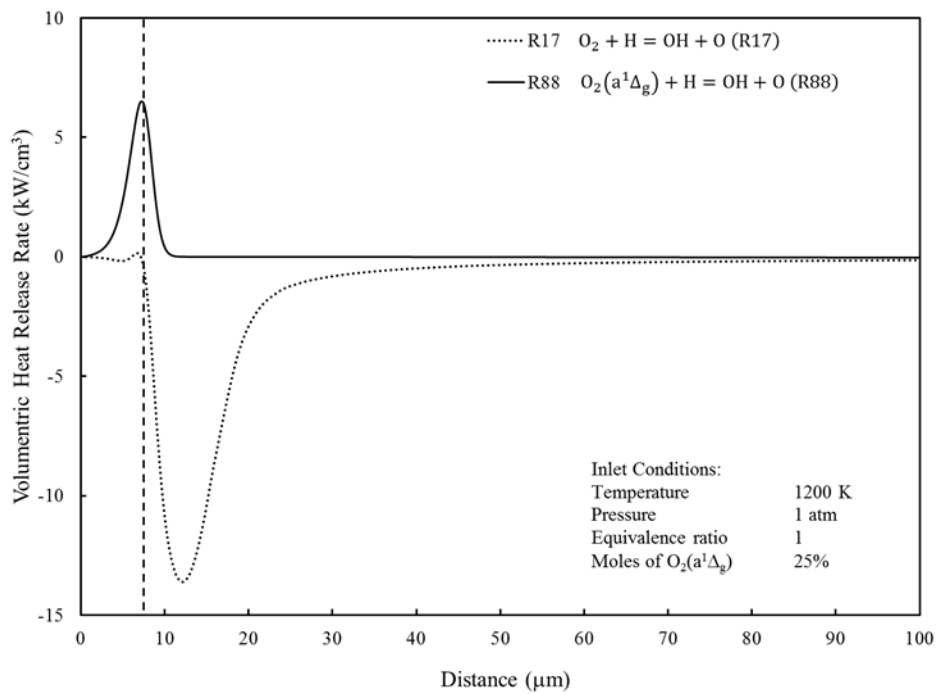


Figure 4.63 Volumetric heat release rate for R17 and R88 for 25% inlet $O_2(a^1\Delta_g)$, $\Phi = 1$, and $T_{in} = 1200$ K

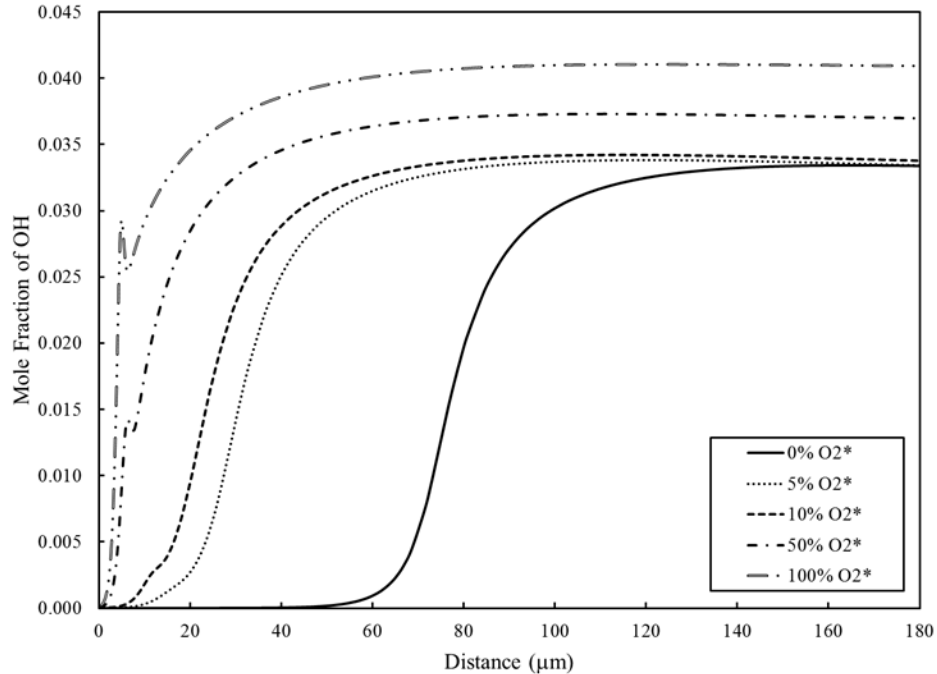


Figure 4.64 Mole fractions of OH for 0%, 5%, 10%, 50%, and 100% inlet $O_2(a^1\Delta_g)$, $\Phi = 1$, and $T_{in} = 1200$ K

4.4 Summary of Findings

4.4.1 Exergy Analysis Findings

4.4.1.1 Model Overview

Two cases were investigated. Model IA which was the base case with no excited oxygen in the charge, and Model IB, which represented a series of extended model runs where excited oxygen was added in increasing amounts while maintaining a stoichiometric fuel-oxidizer ratio. The following is a summary of the key results from the exergy analysis.

4.4.1.2 Exergetic Efficiency of Combustion

There is an optimal region of exergetic efficiency of combustion which exists between 0% - 20%, with the maximum occurring at 10%. After 20% efficiency drops off in a parabolic fashion, decreasing by approximately 1% out to 100% inlet excited oxygen.

4.4.1.3 Total Exergy Destruction before Ignition

The total exergy destruction before ignition was calculated to assess what fraction of the exergy destruction occurred in which combustion zone; thereby providing some insight into what mode of combustion is more irreversible (e.g. induction or primary reaction). It was determined that for the optimal region, 0% - 20%, up to 60% of the exergy destruction occurred before ignition. From 25% - 100%, approximately 30% - 55% of the exergy destruction occurred before ignition. In this region there was a significant reduction in the ignition temperature, ranging from 150 K - 450 K, with 25% showing the most significant reduction.

4.4.1.4 Exergy and Energy Performance Parameters

Several exergy, energy and thermodynamic parameters were analyzed to assess the general performance of the reactor and mechanism. The results are given here: (1) there was a 6% increase in the exit thermomechanical flow exergy, (2) a 4% increase in the reactor exit temperature, (3) a 24% increase in the exit chemical flow exergy, (4) a 3% reduction in the molar conversion of fuel, and (5) a 7% reduction in the completeness of combustion.

Based on the results presented from the exergy analysis and recalling that the only phenomenon responsible for these trends is chemical reaction, the next section presents the results from a detailed mechanism analysis to provide insight into the trends observed.

4.4.2 Reaction Mechanism Findings

4.4.2.1 Approach Overview

Two techniques were employed to analysis the kinetics of the system, sensitivity analysis and reaction flow analysis. Additionally, various other thermochemical parameters were included to provide supplemental insight.

Based on the results of the exergy analysis three data points were of primary interest, the percentages of inlet singlet oxygen of 0%, 10%, and 25%. These values were selected because they coincide with the most significant trends in the model behavior. The base case needed to be examined to establish a kinetic baseline for the mechanism. The 10% case coincides with the best exergetic efficiency of combustion. For 25% inlet excited oxygen not only does the system efficiency decline, so does the ignition temperature.

4.4.2.2 Mechanism Analysis Findings 0% Inlet $O_2(a^1\Delta_g)$

For the baseline case using the Moscow State University mechanism, it was confirmed that R17 is the dominate chain reaction. The reaction path diagram, Figure 4.12, indicates that hydroperoxyl and hydroxyl have the largest relative rates of production associated with triplet oxygen. For the base case hydroperoxyl plays a key role in radical buildup in the induction zone. Most of the hydroxyl production occurs before ignition and is driven by R17. Exergy destruction trends correlate almost perfectly with the total rate of production of hydroxyl. The total rate of production of hydroxyl is directly linked to the rate of consumption of triplet oxygen.

4.4.2.3 Mechanism Analysis Findings 10% Inlet $O_2(a^1\Delta_g)$

The presence of excited oxygen dramatically alters the reaction pathways, establishing new paths and enhancing preexisting ones. R88, which involves excited oxygen, assumes the role as

dominate mechanism reaction. There is a significant reduction of the ignition delay distance. The induction zone is much shorter and singlet oxygen is the key species in the radical buildup process. The rate of hydroxyl production is now dictated by singlet oxygen, key trends begin to develop bimodal distributions. Exergy destruction is still driven by the total rate of production of hydroxyl.

4.4.2.4 Mechanism Analysis Findings 25% Inlet $O_2(a^1\Delta_g)$

With 25% of the inlet oxygen composed of singlet oxygen, several significant results were observed. The reaction flow paths were relatively unchanged. Most of the chemical conversion occurred after ignition; typically it happens before. The ignition delay distance was further reduced. With the increased presence of excited oxygen, rapid radical production occurs in the induction zone; however, not as much thermal energy is released sustaining chemical reaction at lower than normal temperatures. The key trends develop full bimodal distributions and they all experienced a significant horizontal shift to the right. This shift moves the distributions asymmetrically about the ignition point, favored toward the primary reaction zone. Further confirmation was provided that production rates of hydroxyl are closely linked to singlet oxygen consumption. The exergy destruction curve followed the total rate of production trend for hydroxyl to the right of ignition.

4.4.3 Comprehensive Review

Using the information from the previous section, explanations are provided which show how the presence of excited oxygen influences the mechanism, and hence drives the observed trends.

Upon reviewing all three cases, it was shown that the quantity of singlet oxygen present in the charge altered the structure of the reaction zones, by either shortening the chemical zone,

thermal zone, or both. For the 0% case, the induction zone possessed a typical structure as did both subsections. For the 25% case, the overall induction zone was significantly shortened. The reactive nature of the singlet oxygen allowed for radical buildup to occur very rapidly in the induction zone, the resulting concentration of radicals induced chemical reaction which initially released less heat. This can be observed by examining the volumetric heat release curve, which assumes a bimodal shape. The first mode corresponds to the rapid radical buildup which releases heat at rates comparable to the other two cases, but not with the same energy density which is reflected in the temperature gradient. This is followed by another increase in the heat release rate, which occurs in the primary reaction zone where a larger than normal portion of the heat is released. This bimodal trend is also seen in other key parameters. The 10% case is the one that strikes the best balance under these conditions, between purely chemical and thermal aspects of oxidation, resulting in the most efficient use of the fuel exergy. This discussion addresses not only the observed trend in efficiency, but also the reduction in ignition temperature for percentages of inlet singlet oxygen at 25% or greater. The reduction in the molar conversion of fuel with increased exit temperatures is explained by that fact that singlet oxygen reduces the energy required for various endothermic reactions; the net effect is slightly higher exit temperatures.

CHAPTER 5 PARAMETRIC STUDY OF PAC SYSTEMS

5.1 Aspects of the Parametric Study

5.1.1 Overview of Study Objectives

In Phase I of this research project an exergetic analysis was performed on the results of a single-parameter parametric study for the purpose of understanding how varying the concentration of singlet oxygen in the charge affects exergy destruction associated exclusively with oxidation. The results from Phase I provide considerable insight into how singlet oxygen alters the chemical kinetics and production of key chain carriers, thereby indirectly influencing how the destruction of exergy evolves.

Phase II of the project is focused on determining how the observed phenomena from Phase I are impacted by varying other combustion parameters. The objectives for Phase II are to: (1) acquire more understanding of the observed phenomena from Phase I under a broader range of operating conditions, (2) determine if there are more opportunities for optimization of the combustion environment, and (3) develop recommendations for additional research.

5.2 Selection of Combustion Parameters

The results from Phase I were used to define the range of parameters for Phase II of the study. Since the primary interest is the improvement of combustion efficiency, Phase II honed in on the range of excited oxygen that produced the best exergetic efficiencies from Phase I. In

$$\Phi = \frac{n_{fuel}/n_{ox}}{(n_{fuel}/n_{ox})_{st}} \quad (5.1)$$

addition to varying what fraction of the incoming oxygen is at the triplet or singlet state, it was also determined that more knowledge of this effect under non-stoichiometric fuel-oxidizer conditions would also provide valuable insight; therefore, equivalence ratio (Equation 5.1) was considered as a parameter. The production of electronically excited oxygen by electric discharge occurs in the presence of inert diluents, various species have been studied [80]. These species each have different thermodynamic properties; hence diluent type was included as a parameter. Finally, the kinetics associated with combustion is sensitive to the initial temperature of the reactants, especially the chemistry related to ignition. Therefore, inlet temperature was included as well¹¹.

5.3 Parametric Study Results

The results presented here use argon as a diluent. All trends for the no diluent and nitrogen cases were the same. The no diluent cases were an upper bound and the nitrogen cases were a lower bound across all trends.

5.3.1 Present Model Results

The data presented in Figures 5.1 - 5.6 contain the results of the parametric study. Each figure is divided into six parts; parts A - E are plots with fixed concentrations of excited oxygen, while other parameters of interested are varied. Part F provides a statistical summary of the results, which allows high-level comparisons of the datasets to be made.

5.3.1.1 Exergetic Efficiency of Combustion – Figure 5.1

Figure 5.1 displays trends in the exergetic efficiency of combustion. The cases for 1300 K and $\Phi = 1.3$ at 5% and 10% excited oxygen gave the largest exergetic efficiency, 96.06%. The

¹¹ See Table 3.3

case for 1100 K and $\Phi = 0.7$ at 0% excited oxygen gave the lowest efficiency, 93.89%. The difference between the highest and lowest efficiencies is 2.17%. Along any particular contour of equivalence ratio, spanning the temperature range (1100 K - 1300 K) the difference in efficiency is approximately 1%. Over all the ranges of temperatures and equivalence ratios the 5% and 10% excited oxygen cases continually gave the highest efficiencies.

Statistically there is a tight correlation between the data over the range of parameters, which is confirmed by a correlation coefficient of nearly unity when comparing data across datasets for increasing percentages of singlet oxygen to the 0% case. This implies that for the exergetic efficiency of combustion over the optimal range (0% - 20%), exergetic efficiency is relatively insensitive to changes in other combustion parameters. Additionally, comparing the trends in data within each dataset gave a mean average deviation of approximately 0.4, which was fairly consistent across all datasets.

5.3.1.2 Total Exergy Destruction before Ignition – Figure 5.2

Since the optimal range of excited oxygen was selected as the starting point for the study, the total exergy destruction before ignition fluctuates between 55% - 70%, which is in agreement with the results from Phase I. The fluctuating data is reflected in the relatively high mean average deviation values and low correlation coefficient values. This is due to the sensitivity of ignition to inlet conditions [86]. However, the main feature in Figure 5.2 is the dramatic reduction of the total exergy destruction before ignition for the 20% case. This is the same phenomena which occurred at 25% inlet singlet oxygen, presented in Figure 4.7 for stoichiometric inlet conditions. As inlet temperature is increased, this phenomena occurs, impacting each equivalence ratio starting with $\Phi = 0.7$ at 1100K up through $\Phi = 1.15$ at 1300 K. This is driven by the same phenomena discussed in Phase I.

5.3.1.3 Molar Conversion of H_2 – Figure 5.3

Figure 5.3 shows the molar conversion of fuel versus inlet temperature. The largest value is 94.65% at 0% excited oxygen for 1100 K, and decreases to 93.99% at 20% excited oxygen for 1100 K. Therefore, the presence of excited oxygen reduced the molar conversion of fuel by 0.65%, which translates to approximately a 9% increase in the exit chemical flow exergy. By comparison, the case for $\Phi = 1.3$ and 1100 K at 0% excited oxygen has a molar conversion of fuel value of 74.93% and 74.76% at 20% excited oxygen and 1100 K, for a difference of 0.17%. The increase in the exit chemical flow exergy here is only 2.3%. This result underscores trends observed in Phase I.

5.3.1.4 Exit Gas Temperature – Figure 5.4

The exit gas temperature data clearly shows the effects of introducing singlet oxygen into the charge. Comparing the plots, the increasing excited oxygen affects the exit temperature for every equivalence ratio and inlet temperature over the entire range in a systematic fashion; increasing the exit gas temperature. The maximums that occur for $\Phi = 1.15$ are expected for slightly fuel rich combustion, and is not an effect of the excited oxygen.

5.3.1.5 Ignition Temperature – Figure 5.5

Like Figure 5.2, the data regarding ignition temperature in Figure 5.5 fluctuates between 1590 K - 1740 K, which is due to its sensitivity to inlet conditions [86]. This is also the same phenomena identified in Phase I. This is revisited in the review section of this chapter.

5.3.1.6 Ignition Distance – Figure 5.6

The ignition delay data also clearly exhibits the effects of singlet oxygen. A reduction occurs over every inlet temperature and equivalence ratio, as expected.

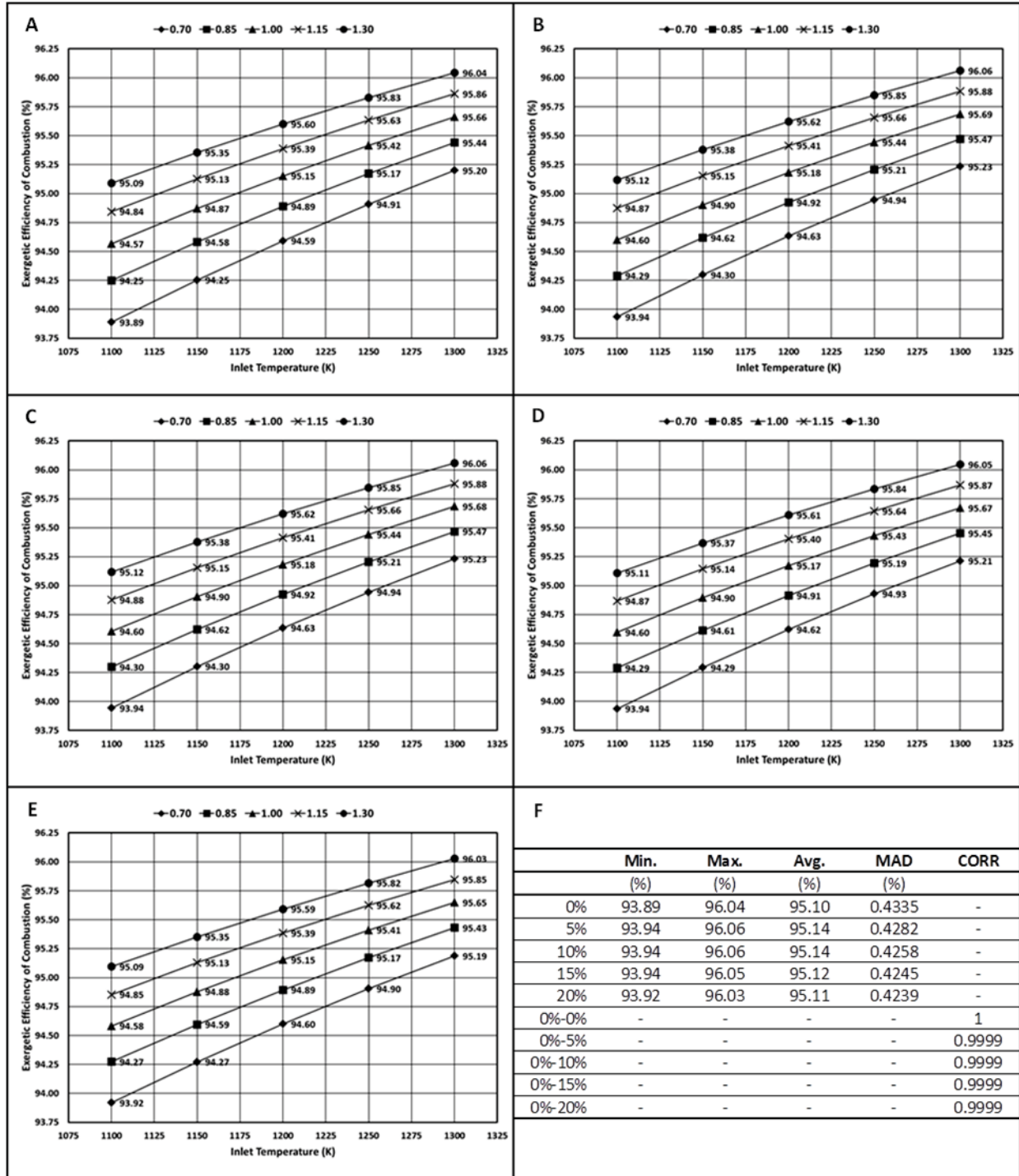


Figure 5.1 Exergetic efficiency of combustion vs. inlet temperature – (A) 0% inlet $O_2(a^1\Delta_g)$, (B) 5% inlet $O_2(a^1\Delta_g)$, (C) 10% inlet $O_2(a^1\Delta_g)$, (D) 15% inlet $O_2(a^1\Delta_g)$, (E) 20% inlet $O_2(a^1\Delta_g)$, (F) Statistical summary. Data in Figures 1A-1F range equivalence ratios $0.7 \leq \Phi \leq 1.3$.

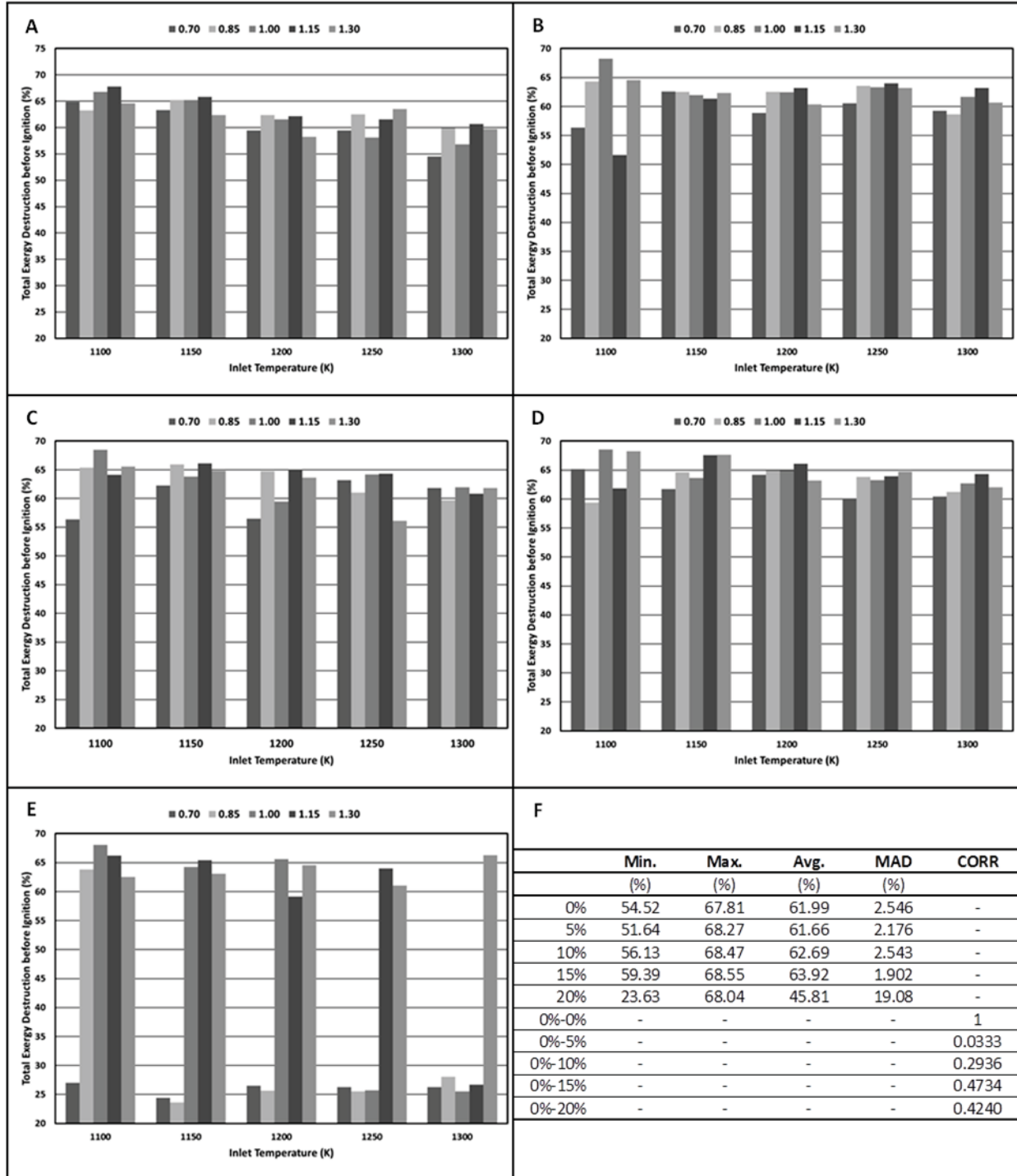


Figure 5.2 Total energy destruction before ignition vs. inlet temperature – (A) 0% inlet $O_2(a^1\Delta_g)$, (B) 5% inlet $O_2(a^1\Delta_g)$, (C) 10% inlet $O_2(a^1\Delta_g)$, (D) 15% inlet $O_2(a^1\Delta_g)$, (E) 20% inlet $O_2(a^1\Delta_g)$, (F) Statistical summary. Data in Figures 1A-1F range equivalence ratios $0.7 \leq \Phi \leq 1.3$.

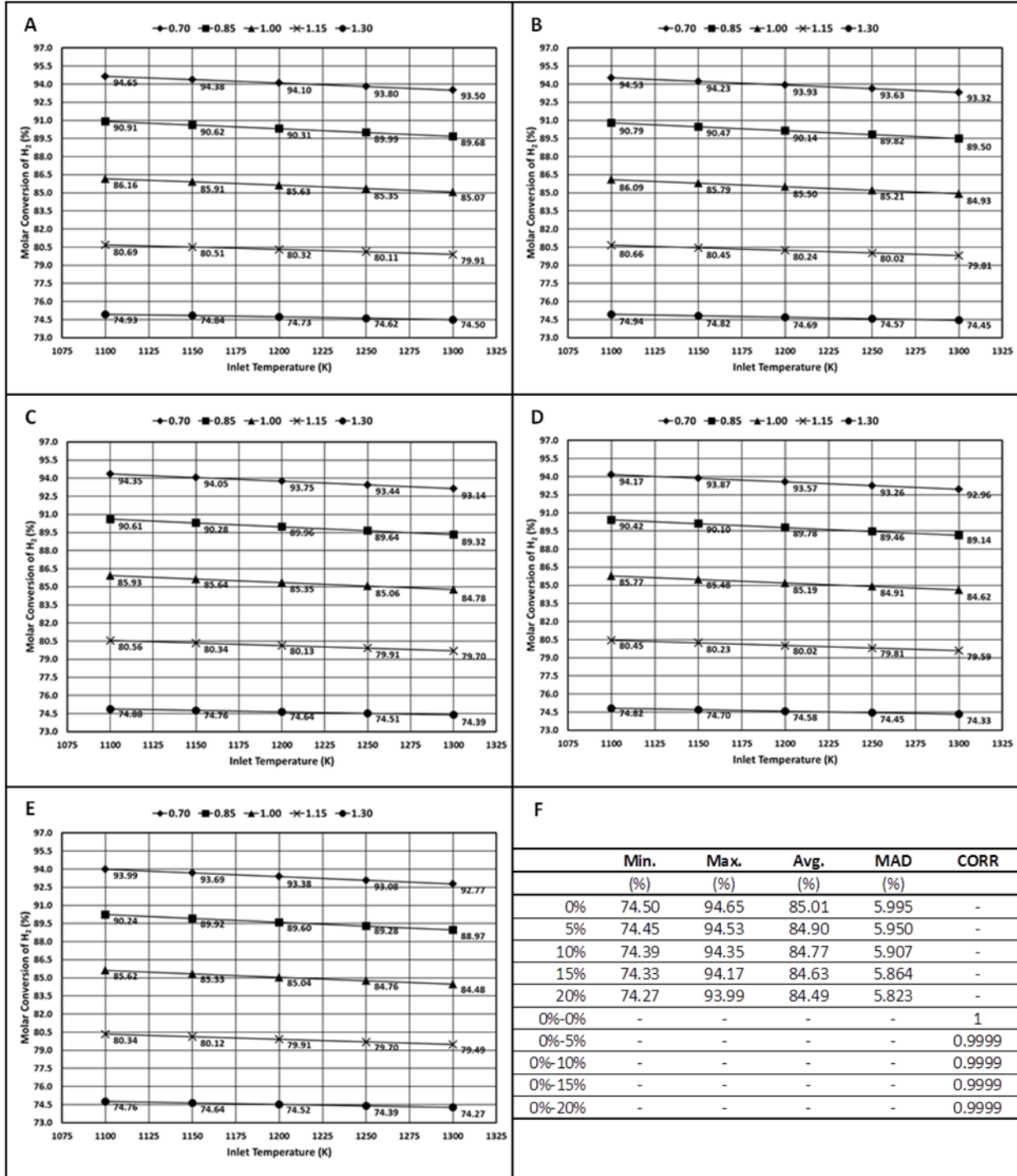


Figure 5.3 Molar conversion of H₂ vs. inlet temperature – (A) 0% inlet O₂(a¹Δ_g), (B) 5% inlet O₂(a¹Δ_g), (C) 10% inlet O₂(a¹Δ_g), (D) 15% inlet O₂(a¹Δ_g), (E) 20% inlet O₂(a¹Δ_g), (F) Statistical summary. Data in Figures 1A-1F range equivalence ratios 0.7 ≤ Φ ≤ 1.3.

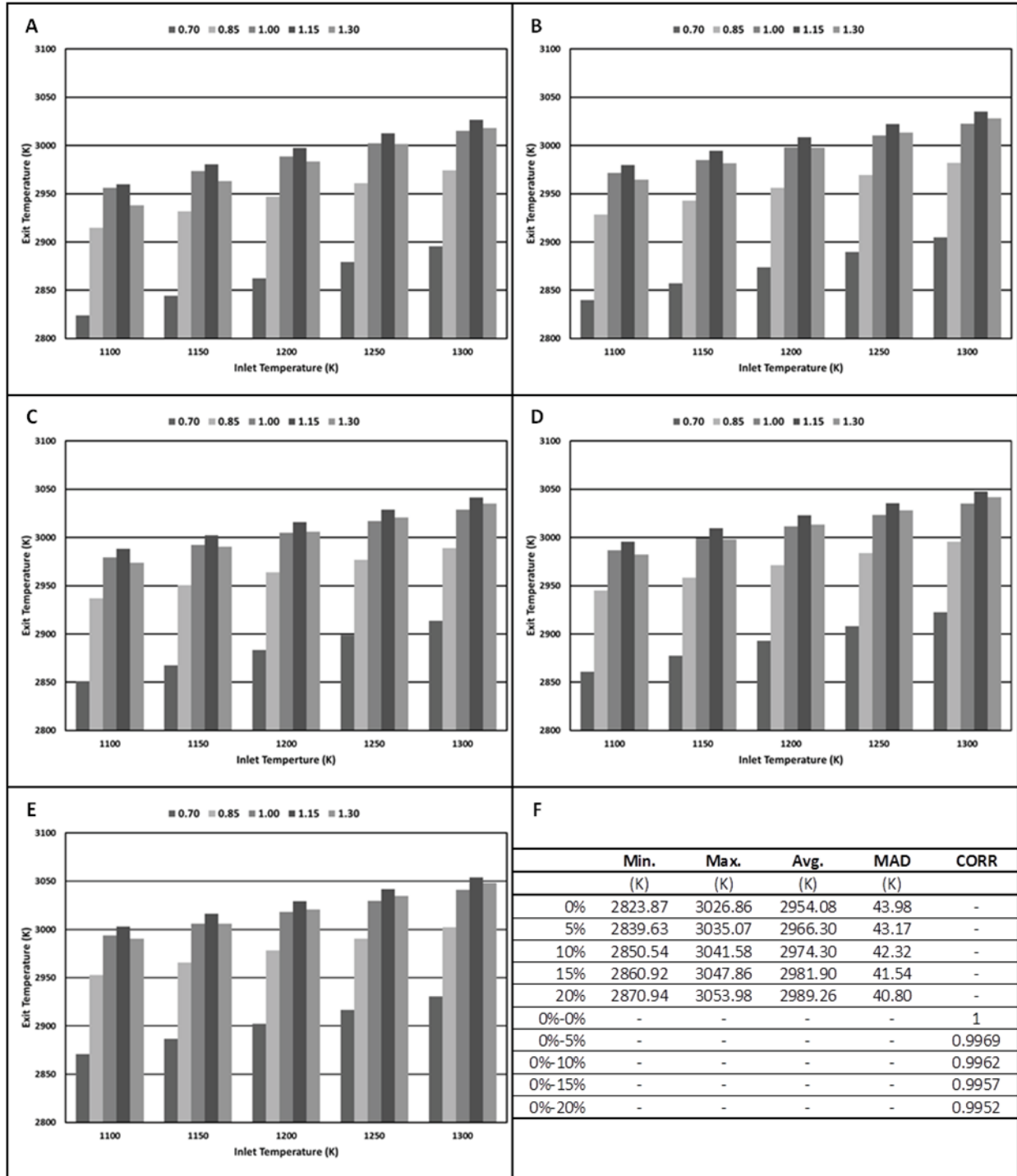


Figure 5.4 Exit temperature vs. inlet temperature – (A) 0% inlet $O_2(a^1\Delta_g)$, (B) 5% inlet $O_2(a^1\Delta_g)$, (C) 10% inlet $O_2(a^1\Delta_g)$, (D) 15% inlet $O_2(a^1\Delta_g)$, (E) 20% inlet $O_2(a^1\Delta_g)$, (F) Statistical summary.

Data in Figures 1A-1F range equivalence ratios $0.7 \leq \Phi \leq 1.3$.

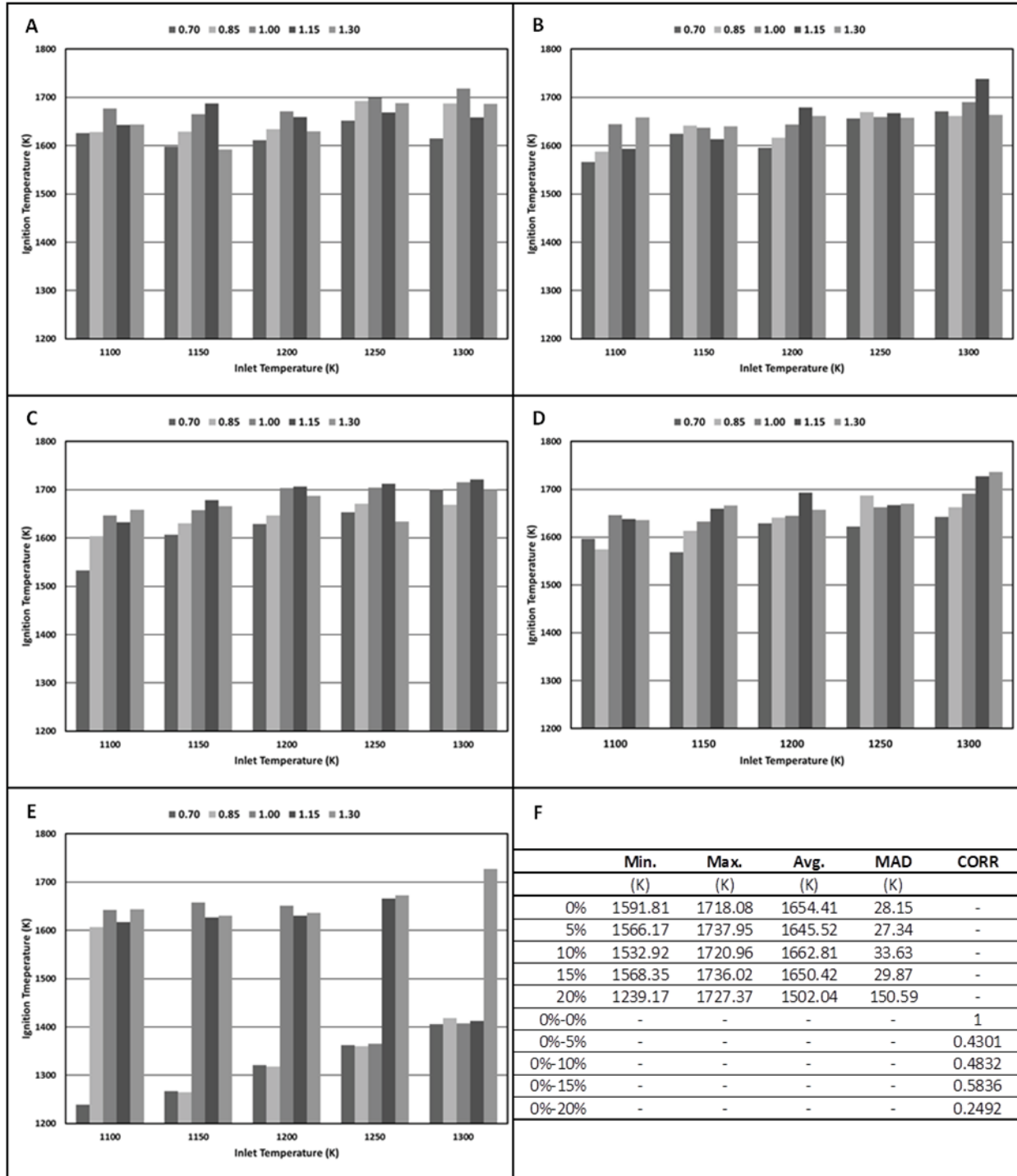


Figure 5.5 Ignition temperature vs. inlet temperature – (A) 0% inlet $O_2(a^1\Delta_g)$, (B) 5% inlet $O_2(a^1\Delta_g)$, (C) 10% inlet $O_2(a^1\Delta_g)$, (D) 15% inlet $O_2(a^1\Delta_g)$, (E) 20% inlet $O_2(a^1\Delta_g)$, (F) Statistical summary. Data in Figures 1A-1F range equivalence ratios $0.7 \leq \Phi \leq 1.3$.

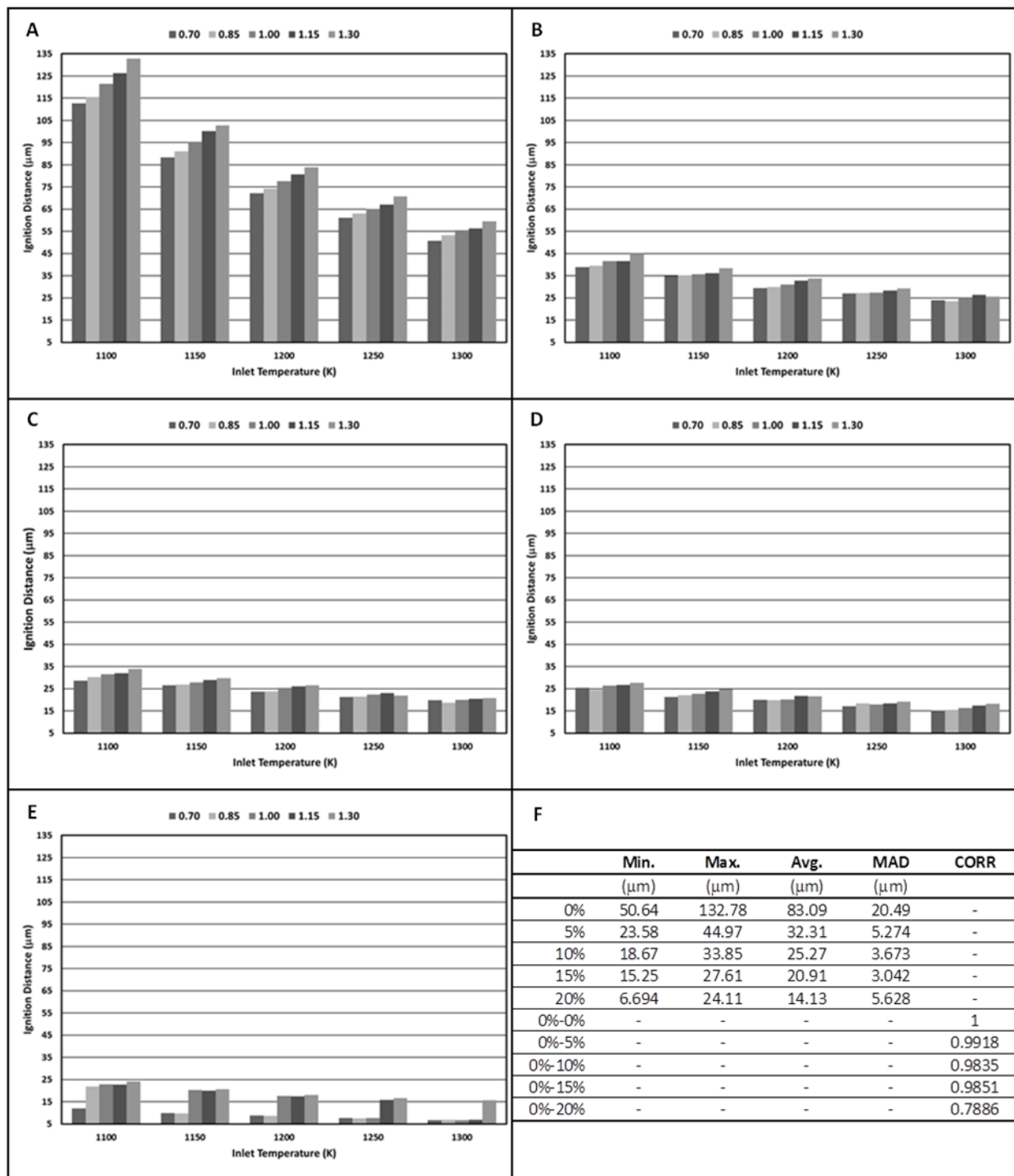


Figure 5.6 Ignition distance vs. inlet temperature – (A) 0% inlet O₂(a¹Δ_g), (B) 5% inlet O₂(a¹Δ_g), (C) 10% inlet O₂(a¹Δ_g), (D) 15% inlet O₂(a¹Δ_g), (E) 20% inlet O₂(a¹Δ_g), (F) Statistical summary.

Data in Figures 1A-1F range equivalence ratios $0.7 \leq \Phi \leq 1.3$.

5.3.2 Literature Model Results

In this section results from this study are compared to work published by Dunbar and Lior [2] of a exergy analysis they conducted for a similar flow reactor model.

5.3.2.1 *Dunbar and Lior Model*

Dunbar and Lior conducted an exergetic analysis of hydrogen combustion using a flow reactor model; the oxidizer used was ideal combustion air (21% O₂ and 79% N₂). The following assumptions and inlet conditions were imposed: (1) adiabatic walls, (2) steady flow, (3) fuel and combustion air enter at standard state (unmixed), (4) products exit reactor under chemical equilibrium conditions, and (5) all flows are at atmospheric pressure. The primary objective of their study was to investigate what fraction of the irreversibility of combustion comes from mixing, oxidation, and internal heat transfer between products and reactants. The model used in the current study is an adiabatic plug flow reactor model, as shown previously the assumptions used to define the model only permit changes in the system due to oxidation, which is the express goal of this study.

5.3.2.2 *Model Comparisons*

The primary differences between the two models are: (1) the fuel and oxidizer enter this model at 1200 K and are premixed, and (2) there no assumption of chemical equilibrium of the products. However, of the two differences only the second difference is significant when evaluating the exergy destruction associated with oxidation. This is due to the fact the reactants have to be heated to their auto-ignition temperature, whether that happens before the reactor or in it make no difference when studying the effects of oxidation exclusively, which is the focus here. For purposes of comparison, data from the current model using nitrogen as a diluent were used.

Examining Figure 5.7, which is the most important comparison, trends in the exergetic

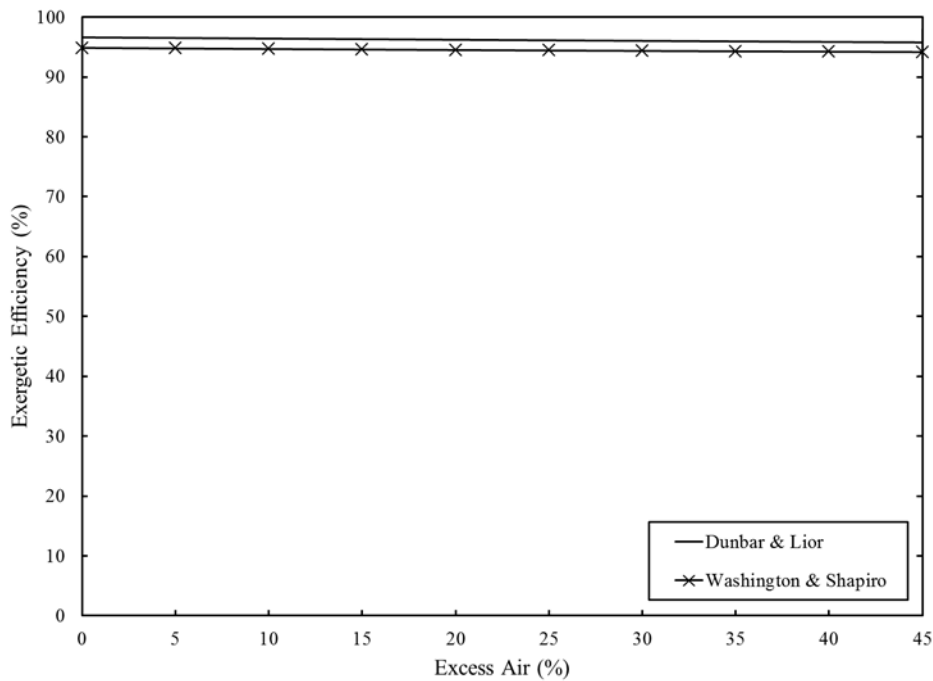


Figure 5.7 Exergetic efficiency vs. excess air

efficiency differ at most by 1.8% over the entire range of excess air.

Figure 5.8 compares the product gas temperatures of both models. At stoichiometric conditions, for the current model the product temperature is approximately 400 K higher than for the Dunbar and Lior model. This is almost the exact difference between the auto-ignition temperature for hydrogen (773.15 K) and the inlet temperature used here (1200 K). As the excess air is increased, the product gas temperature decreases for both models as expected for fuel-lean combustion. However, the Dunbar and Lior model decreases at a faster rate causing a slight divergence between the two trends. This is likely due to the fact that in the Dunbar and Lior model heat is transferred from the products to the reactants. In a plug flow reactor model, this is accounted for indirectly.

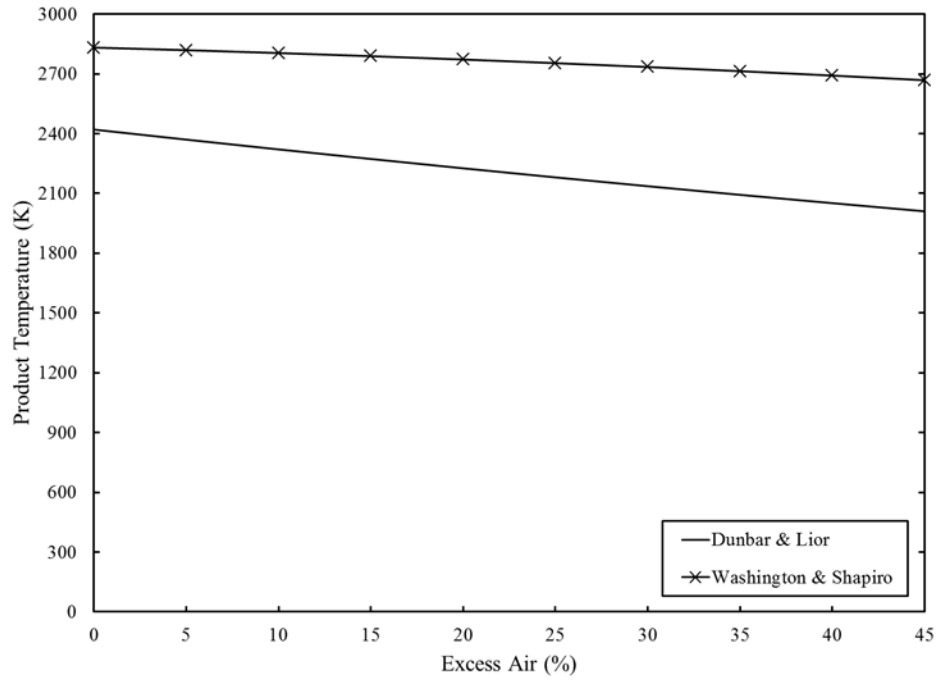


Figure 5.8 Product temperature vs. excess air

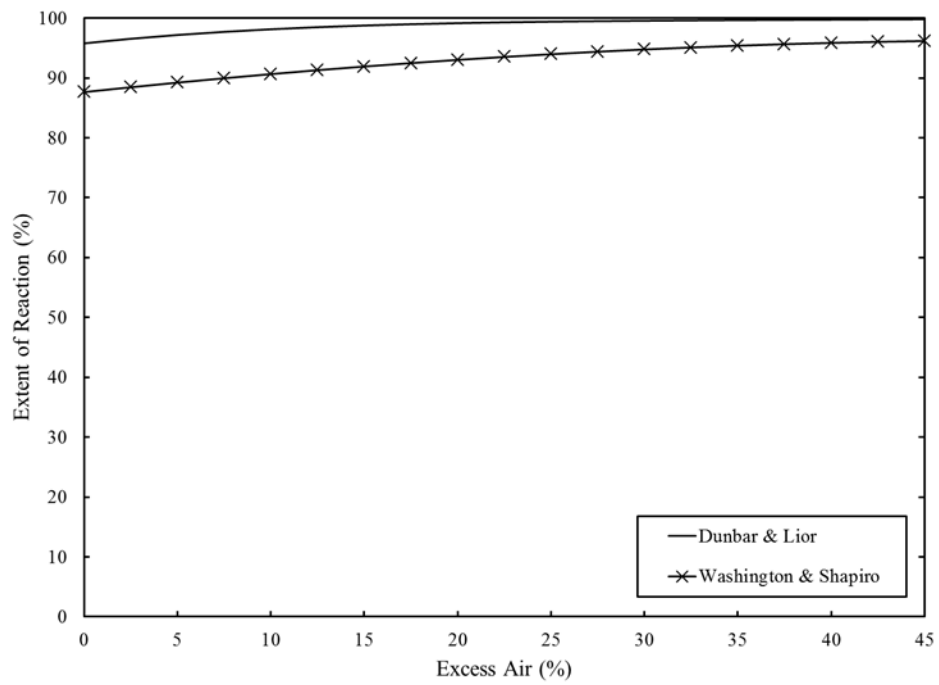


Figure 5.9 Extent of reaction vs. excess air

Figure 5.9 compares the extent of reaction for both models. Here, extent of reaction is viewed as the molar conversion of hydrogen to products. At stoichiometric conditions the trends differ by 8%; out to 45% excess air the trends converge to a difference of 3%. The differences between the molar conversions of fuel trends are likely due to the imposed chemical equilibrium exit boundary condition, but the overall trends are in good agreement.

5.4 Summary of Findings

5.4.1 Comprehensive Review

From the Phase I portion of the project it was established that the optimal range of excited oxygen is 0% - 20%, this was further confirmed by the results of the parametric study. The changes in exergetic efficiency shown in the parametric study data are related primarily to other combustion parameters, implying there is no further enhancement or optimization to make using electronically excited oxygen.

The total exergy destruction before ignition and the ignition temperature, exhibited the behavior identified in Phase I for the 25% excited oxygen case. The phenomena is attributed to rapid radical buildup which occurs in the chemical induction zone, resulting in a chemical reaction that produces less than normal heat output; resulting in less efficient combustion. Its occurrence is marked by a reduction in ignition temperature and percent total exergy destruction before ignition. The remainder of the parameters displayed the expected trends and produced results consistent with PAC systems and traditional modes of combustion.

CHAPTER 6 CONCLUSIONS

6.1 Summary

The objective of this research project was to determine how the presence of electronically excited oxygen affects exergy destruction during oxidation. To accomplish this, the project was divided into two phases.

Phase I consisted of a detailed exergy analysis of a single-parameter parametric study which varied the inlet concentration of singlet oxygen while maintaining a stoichiometric fuel-oxidizer ratio with hydrogen as the fuel. An adiabatic plug flow reactor model was developed using CHEMKIN-PRO[®] to model the kinetics of hydrogen combustion. The model assumptions and resulting governing equations were selected such that the phenomena surrounding the irreversibility associated with oxidation could be isolated and studied. In order to be able to carry out the exergy analysis, an Excel based post processing algorithm was developed to calculate exergy and other thermodynamic properties as well as exergetic efficiency. First-order sensitivity analysis and reaction flow analysis were used to assess the results of the chemical kinetics of the model.

The Phase I study revealed several important findings. An optimal range of exergetic efficiency exists between 0% - 20% excited oxygen. After 20% the exergetic efficiency drops off parabolically from 25% - 100%. From the trends in ignition temperature, it was discovered that for the optimal range of exergetic efficiencies, approximately 60% or more of the total exergy destruction occurred before ignition. After 25% excited oxygen, there was a significant reduction in the ignition temperature and the amount of exergy destruction that occurred before ignition. Through analyzing the chemical kinetics it was determined that for 25% excited

oxygen and above there was rapid radical buildup in the chemical induction zone, which leads to accelerated reaction that produces less than normal heat output but still sustains reaction. This effect drives the conversion of reactants that would normally happen in the induction zone into the primary reaction zone. Eventually enough thermal energy is released to sustain normal chemical reaction. Evidence of this was seen in the sensitivity analysis; there were three major components that were observed. First, at 0% excited oxygen all local distributions of the sensitivity coefficients were symmetric and well structured, and occurred to the left of the ignition coordinate in the induction zone. Second, at 10% excited oxygen the sensitivity coefficients began to develop partial bimodal distributions; however, they were still to the left of the ignition coordinate. Finally, at 25% excited oxygen full bimodal distributions developed for all major combustion metrics, as well as being shifted to the right of the ignition coordinate. The 10% excited oxygen case also corresponded to very active induction zones, with rapid radical buildup.

The sensitivity analysis also demonstrated that when excited oxygen is introduced into the combustion process it becomes the primary driver for the production of hydroxyl, even in very small quantities. The reaction path diagrams showed that the presence of excited oxygen creates new pathways for radical formation and enhances preexisting ones.

It was observed that singlet oxygen reduces the molar conversion of fuel, but this is accompanied by a slight increase in the exit gas temperature. This can be explained by the fact that singlet oxygen reduces the energy required to sustain various endothermic reactions. The net effect is that, although less fuel is being converted to product because of the reduction in energy absorbed by endothermic reactions, a slight temperature rise occurs. Another effect

which accompanies this phenomenon is an increase in the exit chemical flow exergy due to unused fuel exiting the reactor.

The objectives for Phase II were to gain additional understanding of the observed phenomena from Phase I under a broader range of operating conditions, determine if further optimization is possible by varying other combustion parameters, and develop new potential directions for future research.

The results from Phase I were used to guide the efforts for Phase II. The plug flow reactor model was used, but the following combustion parameters were also considered in addition to varying excited oxygen: (1) inlet temperature, (2) equivalence ratio, (3) diluent type. The range of the excited oxygen used was the optimal range defined from Phase I.

It was determined that for the optimal range of excited oxygen defined in Phase I, the exergetic efficiency was relatively insensitive to variations in the other combustion parameters. The total exergy destruction before ignition and the ignition temperature are very sensitive to the inlet conditions, but from 0% - 15% excited oxygen the total exergy destruction fluctuated around values observed in Phase I. However, at 20% excited oxygen there was a significant reduction in the ignition temperature and total exergy destruction before ignition. This was attributed to the phenomena observed at 25% excited oxygen in Phase I. There were systematic reductions in the ignition distance over the whole range of data consistent with trends from Phase I. The exit temperature exhibited an increasing trend in line with results from Phase I. The reduction in the molar conversion of fuel by excited oxygen was still present in the parametric study data; it was more prevalent in the fuel-lean cases.

Finally, the use of nitrogen as a diluent and case of no dilution were also considered. All the trends were the same. Nitrogen exhibited lower values in all categories establishing a lower boundary, and no dilution yields higher values in all cases form an upper boundary. The lower values for nitrogen can be traced to a higher specific heat. Since it is a diatomic molecule, nitrogen has more modes to store energy than argon. When there is no dilution, the result is pure hydrogen combustion; therefore, there are no species involved that are not directly active in the combustion process at some level.

6.2 Conclusions

The introduction of excited oxygen into combustion has several benefits and in the proper amounts enhances the chemical kinetics. The goal here was to determine its impact on exergy destruction associated exclusively with oxidation, with the goal of trying to understand if it might be possible to enhance combustion efficiency. The work carried out in Phase I determined that there is a mild increase in the exergetic efficiency between 0% - 20%. It was also determined that the presence of excited oxygen reduces the molar conversion of fuel, while sustaining a small increase in the exit gas temperature. The result of this is an increase in the exit chemical flow exergy which presents an opportunity to extract additional work. From Phase II it was concluded that the impact excited oxygen has on the exergetic efficiency is relatively insensitive to variations in the other combustion parameters. All the other metrics carried over roughly the same tendencies over the range of combustion parameters. With further study involving more detailed models it may be possible to use these characteristics to further enhance combustion in a number of important applications.

6.3 Accomplishments

As the first exergy analysis of a PAC system, this research effort resulted in several contributions to both the fields of exergy analysis and PAC. In order to perform an exergy analysis of a PAC system the chemical exergy of the electronically excited species must be determined. A novel method for establishing the chemical exergy of electronically excited species was developed, allowing for the accurate evaluation of exergy, exergy destruction, and exergetic efficiency.

Most PAC studies only examine the presence of excited oxygen up to 5%, because the current technology can only support this level of production. However, during this study the use of electronically excited oxygen was explored all the way out to 100%. Establishing the behavior of the mechanism kinetics and trends in the metrics of exergy performance, this research will be critical in helping facilitate future design efforts and research directions.

The model used for this study was developed to isolate the phenomena of exergy destruction associated with oxidation. Typically, most combustion irreversibility models lump all modes of exergy destruction together, preventing a detailed study of phenomena related specifically with oxidation. Using this model, a detailed sensitivity analysis and reaction flow analysis was conducted to establish a more fundamental understanding of the behavior of mechanisms involving electronically excited species. The combination of these contributions will help build a bridge between the exergy and PAC communities to advance technology and research.

6.4 Future Work

In order to advance this line of research there are several things that need to be investigated. Most of the current research regarding the use of electronically excited oxygen in combustion is for pressures up to 1 atm [87, 88]. To extend this research to a broader range of energy conversion devices involving chemical reaction, more attention needs to be given to the effects of pressure on the order of magnitude encountered in internal combustion engines. This should include both experimental and computational efforts [40].

To facilitate the development of more robust reaction mechanisms and detailed models, more effort needs to be directed toward the inclusion of nonequilibrium effects on reaction rates [89], as well as transport properties [90-92]. Currently, there is very little data readily accessible for engineering modeling efforts [3].

To calculate the chemical exergy associated with radiant emission, additional work needs to be done on the development of radiant exchange with the exergy reference environment. There is well established theory and work regarding the exergy of radiation [93]; however, very little has been done regarding its application to combustion chemistry.

Finally, this model needs to be applied to simple hydrocarbons to determine if the trends observed for hydrogen carryover to hydrocarbons, or if new trends emerge. The combination of the aforementioned tracks of research will allow for more robust exergetic modeling of PAC systems while advancing each of the respective fields of study.

APPENDIX A: REACTION MECHANISM

Table A.1 Moscow State University mechanism [3, 5]

No.	Reaction*	A	n	E _a (K)	Δlog k
1.	$\text{H}_2 + \text{O}_2 \rightleftharpoons \text{H} + \text{HO}_2$	1.94E+14	0.00	29770	0.20
		2.39E+13	0.10	711	0.20
2.	$\text{H}_2 + \text{O}_2 \rightarrow \text{O} + \text{H}_2\text{O}$	3.00E+13	0.00	35000	-
3.	$\text{H}_2 + \text{O}_2 \rightleftharpoons \text{OH} + \text{OH}$	4.47E+11	0.00	17338	0.50
		1.70E+13	0.00	24100	0.80
4.	$\text{H}_2 + \text{Ar} \rightleftharpoons \text{H} + \text{H} + \text{Ar}$	2.23E+14	0.00	48350	0.20
		6.48E+17	-1.00	0	0.50
5.	$\text{H}_2 + \text{H}_2 \rightleftharpoons \text{H} + \text{H} + \text{H}_2$	3.46E+14	0.00	48350	0.24
		9.72E+16	-0.60	0	0.50
6.	$\text{H}_2 + \text{H}_2\text{O} \rightleftharpoons \text{H} + \text{H} + \text{H}_2\text{O}$	8.48E+19	-1.10	52530	0.70
		1.00E+19	-1.00	0	0.70
7.	$\text{H}_2 + \text{O}_2 \rightarrow \text{H} + \text{H} + \text{O}_2$	3.46E+14	0.00	48350	0.50
8.	$\text{H} + \text{H} + \text{H} \rightarrow \text{H}_2 + \text{H}$	3.20E+15	0.00	0	0.50
9.	$\text{O}_2 + \text{Ar} \rightleftharpoons \text{O} + \text{O} + \text{Ar}$	1.50E+18	-1.00	59380	0.17
		1.89E+13	0.00	-900	0.11
10.	$\text{O}_2 + \text{O}_2 \rightleftharpoons \text{O} + \text{O} + \text{O}_2$	9.80E+24	-2.50	59380	0.30
		1.50E+16	-0.41	0	0.23
11.	$\text{O}_2 + \text{O} \rightleftharpoons \text{O} + \text{O} + \text{O}$	3.50E+25	-2.50	59380	0.40
		5.34E+16	-0.41	0	0.20
12.	$\text{O}_2 + \text{O}_3 \rightleftharpoons \text{O} + \text{O} + \text{O}_3$	1.20E+19	-1.00	59380	1.00
		1.30E+14	0.00	-900	0.80
13.	$\text{O}_2 + \text{H}_2\text{O} \rightarrow \text{O} + \text{O} + \text{H}_2\text{O}$	1.20E+19	-1.00	59380	1.00
14.	$\text{H}_2 + \text{O}_2 + \text{O}_2 \rightarrow \text{HO}_2 + \text{HO}_2$	2.00E+17	0.00	13000	-
15.	$\text{H}_2 + \text{OH} \rightleftharpoons \text{H} + \text{H}_2\text{O}$	2.53E+08	1.48	1700	0.50

Continued on next page

No.	Reaction*	A	n	E _a (K)	Δlog k
		1.87E+14	0.00	10433	0.30
16.	OH + OH ⇌ H ₂ O + O	1.50E+09	1.14	50	0.20
		5.75E+13	0.00	9052	0.20
17.	O ₂ + H ⇌ OH + O	8.65E+14	-0.24	8200	0.10
		8.91E+12	0.00	-251	0.30
18.	H ₂ + O ⇌ OH + H	5.10E+04	2.67	3160	0.50
		4.88E+03	2.80	1950	0.30
19.	O ₂ + O + Ar ⇌ O ₃ + Ar	4.30E+12	0.00	-1050	0.60
		2.48E+14	0.00	11430	0.10
20.	O ₂ + O + O ₂ ⇌ O ₃ + O ₂	3.26E+19	-2.06	0	0.60
		1.54E+14	0.00	11600	-
21.	O ₂ + O + O ⇌ O ₃ + O ₂	2.28E+15	-0.50	-700	0.30
		2.48E+15	0.00	11430	-
22.	O ₂ + O + O ₃ ⇌ O ₃ + O ₃	1.67E+15	-0.51	-700	0.36
		4.40E+14	0.00	11600	0.20
23.	O ₂ + H + Ar ⇌ HO ₂ + Ar	6.10E+17	-0.80	0	0.50
		2.10E+15	0.00	2300	0.20
24.	O ₂ + H + O ₂ ⇌ HO ₂ + O ₂	2.70E+18	-1.00	0	0.70
		2.80E+15	0.00	23000	0.30
25.	O ₂ + H + H ₂ → HO ₂ + H ₂	2.09E+18	-0.80	0	0.50
26.	O ₂ + H + H ₂ O → HO ₂ + H ₂ O	1.56E+18	-0.80	0	0.50
27.	H ₂ O ₂ + Ar ⇌ OH + OH + Ar	6.00E+16	0.00	22900	0.30
		6.33E+23	-2.53	42	-
28.	H ₂ O ₂ + H ₂ → OH + OH + H ₂	3.20E+17	0.00	23820	-
29.	H ₂ O ₂ + H ₂ O ₂ → OH + OH + H ₂ O ₂	2.51E+18	0.00	24154	-
30.	OH + OH + H ₂ O → H ₂ O ₂ + H ₂ O	1.44E+18	0.00	0	0.40
31.	H + OH + Ar ⇌ H ₂ O + Ar	8.30E+21	-2.00	0	0.30

Continued on next page

No.	Reaction*	A	n	E _a (K)	Δlog k
		4.00E+23	-2.20	59000	0.60
32.	H + OH + H ₂ O ⇌ H ₂ O + H ₂ O	1.40E+23	-2.00	0	0.50
		1.60E+17	0.00	57491	0.30
33.	H + OH + H ₂ → H ₂ O + H ₂	2.00E+20	-1.00	0	-
34.	H + OH + OH → H ₂ O + OH	8.34E+15	0.00	0	-
35.	H ₂ O + O ₂ → H + OH + O ₂	3.50E+15	0.00	52920	-
36.	H + O + Ar ⇌ OH + Ar	4.71E+18	-1.00	0	0.70
		2.41E+15	0.00	50000	0.70
37.	H + O + O ₂ ⇌ OH + O ₂	4.71E+18	-1.00	0	0.70
		2.41E+15	0.00	50000	0.70
38.	OH + O + Ar → HO ₂ + Ar	8.00E+16	0.00	0	2.00
39.	OH + H ₂ O → H ₂ + HO ₂	7.90E+09	0.43	36100	1.40
40.	O ₂ + OH ⇌ O + HO ₂	2.23E+13	0.00	26500	0.50
		1.75E+13	0.00	-200	0.30
41.	HO ₂ + H ⇌ OH + OH	1.69E+14	0.00	-440	0.40
		1.20E+13	0.00	20200	1.00
42.	OH + HO ₂ ⇌ H ₂ O + O ₂	2.85E+13	0.00	-250	0.13
		5.60E+13	0.17	36600	1.50
43.	OH + O ₃ → O ₂ + HO ₂	9.60E+11	0.00	1000	0.60
44.	O ₂ + O ₂ ⇌ O ₃ + O	1.20E+12	0.00	50500	0.60
		4.82E+12	0.00	20600	0.30
45.	O ₂ + OH ⇌ H + O ₃	4.40E+07	1.44	38600	2.00
		6.87E+13	0.00	437	0.70
46.	HO ₂ + O ₃ → OH + O ₂ + O ₂	1.66E+11	-0.28	1000	0.45
47.	H ₂ + HO ₂ ⇌ H ₂ O ₂ + H	3.01E+13	0.00	13100	0.50
		1.69E+12	0.00	1890	0.30
48.	H ₂ + H ₂ O ₂ → H ₂ O + OH + H	8.69E+12	0.50	18347	-

Continued on next page

No.	Reaction*	A	n	E _a (K)	Δlog k
49.	$\text{H}_2\text{O}_2 + \text{O}_2 \rightleftharpoons \text{HO}_2 + \text{HO}_2$	5.42E+13	0.00	20000	0.70
		1.80E+12	0.00	0	0.50
50.	$\text{H} + \text{H}_2\text{O}_2 \rightleftharpoons \text{H}_2\text{O} + \text{OH}$	1.02E+13	0.00	1800	0.30
		2.40E+14	0.00	40500	1.00
51.	$\text{H}_2\text{O} + \text{HO}_2 \rightleftharpoons \text{OH} + \text{H}_2\text{O}_2$	2.80E+13	0.00	16500	0.30
		4.46E+12	0.00	477	0.50
52.	$\text{H}_2\text{O} + \text{O}_2 \rightleftharpoons \text{O} + \text{H}_2\text{O}_2$	3.40E+10	0.52	44800	1.40
		8.40E+11	0.00	2130	1.00
53.	$\text{H}_2\text{O}_2 + \text{O} \rightarrow \text{OH} + \text{HO}_2$	1.08E+12	0.00	2000	0.35
54.	$\text{OH}(\text{A}^2\Sigma^+) + \text{H}_2 \rightarrow \text{H}_2\text{O} + \text{H}$	1.00E+14	0.00	276	-
55.	$\text{OH}(\text{A}^2\Sigma^+) + \text{Ar} \rightarrow \text{OH} + \text{Ar}$	2.90E+09	0.50	0	-
56.	$\text{OH}(\text{A}^2\Sigma^+) + \text{H}_2 \rightarrow \text{OH} + \text{H}_2$	2.90E+11	0.50	0	-
57.	$\text{OH}(\text{A}^2\Sigma^+) + \text{O}_2 \rightarrow \text{OH} + \text{O}_2$	2.90E+11	0.50	0	-
58.	$\text{OH}(\text{A}^2\Sigma^+) + \text{H}_2\text{O} \rightarrow \text{OH} + \text{H}_2\text{O}$	2.90E+13	0.50	0	-
59.	$\text{OH}(\text{A}^2\Sigma^+) \rightarrow \text{OH} + h\nu$	1.40E+06	0.00	0	-
60.	$\text{H}_2 + \text{HO}_2 \rightarrow \text{H}_2\text{O} + \text{OH}(\text{A}^2\Sigma^+)$	4.80E+19	-1.70	19000	-
61.	$\text{O} + \text{H} + \text{Ar} \rightarrow \text{OH}(\text{A}^2\Sigma^+) + \text{Ar}$	3.00E+18	-1.00	0	-
62.	$\text{O} + \text{H} + \text{H}_2 \rightarrow \text{OH}(\text{A}^2\Sigma^+) + \text{H}_2$	3.00E+18	-1.00	0	-
63.	$\text{O} + \text{H} + \text{O}_2 \rightarrow \text{OH}(\text{A}^2\Sigma^+) + \text{O}_2$	3.00E+18	-1.00	0	-
64.	$\text{O} + \text{H} + \text{OH} \rightarrow \text{OH}(\text{A}^2\Sigma^+) + \text{OH}$	1.50E+19	-1.00	0	-
65.	$\text{O}({}^1\text{D}_2) + \text{H} + \text{Ar} \rightarrow \text{OH}(\text{A}^2\Sigma^+) + \text{Ar}$	1.50E+18	-1.00	0	-
66.	$\text{O}({}^1\text{D}_2) + \text{H} + \text{H}_2 \rightarrow \text{OH}(\text{A}^2\Sigma^+) + \text{H}_2$	4.77E+18	-1.00	0	-
67.	$\text{O}({}^1\text{D}_2) + \text{H} + \text{O}_2 \rightarrow \text{OH}(\text{A}^2\Sigma^+) + \text{O}_2$	4.77E+18	-1.00	0	-
68.	$\text{OH}(\text{A}^2\Sigma^+) + \text{O}_2 \rightarrow +\text{O}_3 + \text{H}$	2.30E+12	0.50	0	-
69.	$\text{OH}(\text{A}^2\Sigma^+) + \text{O}_2 \rightarrow +\text{HO}_2 + \text{O}$	1.20E+12	0.50	0	-
70.	$\text{OH}(\text{A}^2\Sigma^+) + \text{H}_2\text{O} \rightarrow +\text{H}_2\text{O}_2 + \text{H}$	7.50E+12	0.00	276	-
71.	$\text{O}_2(\text{a}^1\Delta_g) + \text{M} \rightarrow \text{O} + \text{O} + \text{M}$	2.60E+18	0.00	48188	-

Continued on next page

No.	Reaction*	A	n	E _a (K)	Δlog k
72.	$O_3 + M \rightleftharpoons O_2(a^1\Delta_g) + O + M$	1.30E+14	0.00	11400	-
		6.90E+12	0.00	-1050	-
73.	$HO_2 + M \rightleftharpoons O_2(a^1\Delta_g) + H + M$	6.90E+14	0.00	23000	-
		1.50E+15	0.00	-500	-
74.	$O_2(a^1\Delta_g) + Ar \rightarrow O_2 + Ar$	5.00E+03	0.00	0	-
75.	$O_2(a^1\Delta_g) + H_2 \rightarrow O_2 + H_2$	2.70E+06	0.00	0	-
76.	$O_2(a^1\Delta_g) + O_2 \rightarrow O_2 + O_2$	1.60E+06	0.00	0	-
77.	$O_2(a^1\Delta_g) + H \rightarrow O_2 + H$	4.20E+08	0.00	0	-
78.	$O_2(a^1\Delta_g) + O \rightarrow O_2 + O$	4.20E+08	0.00	0	-
79.	$O_2(a^1\Delta_g) + H_2O \rightarrow O_2 + H_2O$	3.40E+06	0.00	0	-
80.	$O_2(a^1\Delta_g) + HO_2 \rightarrow O_2 + HO_2$	3.40E+06	0.00	0	-
81.	$O_2(a^1\Delta_g) + H_2O_2 \rightarrow O_2 + H_2O_2$	3.40E+06	0.00	0	-
82.	$O_2(a^1\Delta_g) + OH \rightarrow O_2 + OH$	3.40E+06	0.00	0	-
83.	$H + HO_2 \rightarrow O_2(a^1\Delta_g) + H_2$	4.80E+07	1.67	3162	-
84.	$O(^1D_2) + O_2(a^1\Delta_g) \rightarrow O + O_2$	6.03E+12	0.00	0	0.40
85.	$O_2(a^1\Delta_g) + O_3 \rightarrow O_2 + O_2 + O$	3.13E+13	0.00	2840	-
86.	$O_2(a^1\Delta_g) + H_2 \rightarrow H_2O + O(^1D_2)$	3.50E+13	0.00	20000	-
87.	$O_2(a^1\Delta_g) + O_2 \rightarrow O_3 + O$	1.20E+13	0.00	39604	-
88.	$O_2(a^1\Delta_g) + H \rightleftharpoons OH + O$	1.10E+14	0.00	3188	-
		5.80E+12	0.00	6224	-
89.	$O_2(a^1\Delta_g) + H_2 \rightarrow OH + OH$	1.70E+15	0.00	17000	-
90.	$O_2(a^1\Delta_g) + OH \rightarrow H + O_3$	4.40E+07	1.44	27225	-
91.	$O_2(a^1\Delta_g) + OH \rightarrow H + HO_2$	1.30E+13	0.00	17000	-
92.	$O_3 + OH \rightarrow HO_2 + O_2(a^1\Delta_g)$	4.80E+11	0.00	1000	-
93.	$O_3 + HO_2 \rightarrow OH + O_2 + O_2(a^1\Delta_g)$	1.00E+10	0.00	1000	-
94.	$HO_2 + HO_2 \rightarrow H_2O_2 + O_2(a^1\Delta_g)$	9.00E+12	0.00	500	-
95.	$O_2 + O(^1D_2) \rightarrow O_2(a^1\Delta_g) + O$	1.20E+13	0.00	0	-

Continued on next page

No.	Reaction*	A	n	E _a (K)	Δlog k
96.	$O(^1D_2) + H_2 \rightarrow OH + H$	8.70E+13	0.00	-14	-
97.	$HO_2 + H \rightarrow H_2O + O(^1D_2)$	1.70E+12	0.46	678	-
98.	$O(^1D_2) + Ar \rightarrow O + Ar$	3.00E+11	0.00	0	-
99.	$O(^1D_2) + O_2 \rightarrow O + O_2$	1.93E+13	0.00	67	-
100.	$O(^1D_2) + O \rightarrow O + O$	3.00E+12	0.00	0	0.30
101.	$O(^1D_2) + H_2O \rightarrow OH + OH$	1.30E+14	0.00	0	-
102.	$O(^1D_2) + O_3 \rightarrow O + O + O_2$	7.90E+13	0.00	0	-

*For reversible reactions, the Arrhenius parameters are given in the row immediately below the reaction [3, 5].

APPENDIX B: THERMODYNAMIC DATA

Table B.1 Thermodynamic polynomial curvefit coefficients [4, 52]

Species*	T(K)	a ₁	a ₂	a ₃	a ₄	a ₅	a ₆	a ₇
Ar	1000-6000	2.49881995E+00	0.00000000E+00	0.00000000E+00	0.00000000E+00	0.00000000E+00	-7.45023167E+02	4.37765397E+00
	200-1000	2.49881995E+00	0.00000000E+00	0.00000000E+00	0.00000000E+00	0.00000000E+00	-7.45023167E+02	4.37765397E+00
H	1000-6000	2.49881995E+00	0.00000000E+00	0.00000000E+00	0.00000000E+00	0.00000000E+00	2.54620513E+04	-4.46513534E-01
	200-1000	2.49881995E+00	0.00000000E+00	0.00000000E+00	0.00000000E+00	0.00000000E+00	2.54620513E+04	-4.46513534E-01
HO ₂	900-6000	3.99256693E+00	2.22481868E-03	-5.67738553E-07	6.65718526E-11	-3.07459025E-15	-1.12108039E+03	3.94579415E+00
	200-900	4.16383011E+00	-3.43837341E-03	1.70409522E-05	-1.90287823E-08	6.98226808E-12	-9.53375857E+02	4.24054770E+00
H ₂	1100-6000	2.85258591E+00	9.44377886E-04	-2.03613290E-07	2.68059598E-11	-1.48773572E-15	-7.80512408E+02	-5.77472709E-01
	200-1100	2.68288593E+00	4.87289378E-03	-1.00762600E-05	8.74694314E-09	-2.60531776E-12	-9.43519627E+02	-6.53236135E-01
H ₂ O	1000-5000	2.67214600E+00	3.05629300E-03	-8.73026000E-07	1.20099600E-10	-6.39161800E-15	-2.98992100E+04	6.86281700E+00
	300-1000	3.38684200E+00	3.47498200E-03	-6.35469600E-06	6.96858100E-09	-2.50658800E-12	-3.02081100E+04	2.59023300E+00
H ₂ O ₂	1000-5000	4.57316700E+00	4.33613600E-03	-1.47468900E-06	2.34890400E-10	-1.43165400E-14	-1.80069600E+04	5.01137000E-01
	300-1000	3.38875400E+00	6.56922600E-03	-1.48501300E-07	-4.62580600E-09	2.47151500E-12	-1.76631500E+04	6.78536300E+00
N ₂	1000-5000	2.92664000E+00	1.48797700E-03	-5.68476100E-07	1.00970400E-10	-6.75335100E-15	-9.22797700E+02	5.98052800E+00
	300-1000	3.29867700E+00	1.40824000E-03	-3.96322200E-06	5.64151500E-09	-2.44485500E-12	-1.02090000E+03	3.95037200E+00
O	800-6000	2.56605152E+00	-6.26117046E-05	1.31091484E-08	1.53338374E-12	-2.43718941E-16	2.92017210E+04	4.78475663E+00
	200-800	3.09088643E+00	-2.58436395E-03	4.54935271E-06	-3.61863467E-09	1.08104789E-12	2.91144699E+04	2.34936059E+00
O ₂	1000-5000	3.69757800E+00	6.13519700E-04	-1.25884200E-07	1.77528100E-11	-1.13643500E-15	-1.23393000E+03	3.18916600E+00
	300-1000	3.21293600E+00	1.12748600E-03	-5.75615000E-07	1.31387700E-09	-8.76855400E-13	-1.00524900E+03	6.03473800E+00
O ₃	1000-6000	5.57468421E+00	1.51163453E-03	-5.65785740E-07	9.65022298E-11	-6.00028261E-15	1.51776289E+04	-4.05539668E+00
	200-1000	3.09404274E+00	5.22486249E-03	3.17837919E-06	-8.60894565E-09	3.72269617E-12	1.59842241E+04	9.46459896E+00
O(¹ D ₂)	1000-6000	2.49368475E+00	1.37617903E-05	-1.00401058E-08	2.76012182E-12	-2.01597513E-16	5.19986304E+04	4.65050950E+00
	200-1000	2.49993786E+00	1.71935346E-07	-3.45215267E-10	3.71342028E-13	-1.70964494E-16	5.19965317E+04	4.61684555E+00
O ₂ (a ¹ Δ _g)	1000-6000	3.45852381E+00	1.04045351E-03	-2.79664041E-07	3.11439672E-11	-8.55656058E-16	1.02229063E+04	4.15264119E+00
	200-1000	3.78535371E+00	-3.21928540E-03	1.12323443E-05	-1.17254068E-08	4.17659585E-12	1.02922572E+04	3.27320239E+00
OH	1000-5000	2.88273000E+00	1.01397400E-03	-2.27687700E-07	2.17468400E-11	-5.12630500E-16	3.88688800E+03	5.59571200E+00
	300-1000	3.63726600E+00	1.85091000E-04	1.67616500E-06	2.38720300E-09	-8.43144200E-13	3.60678200E+03	1.35886000E+00
OH(A ² Σ ⁺)	1000-6000	2.75582920E+00	1.39848756E-03	-4.19428493E-07	6.33453282E-11	-3.56042218E-15	5.09751756E+04	5.62581429E+00
	200-1000	3.46084428E+00	5.01872172E-04	-2.00254474E-06	3.18901984E-09	-1.35451838E-12	5.07349466E+04	1.73976415E+00

*The thermodynamic polynomial curvefit coefficients for the electronically excited species were obtained from the work of Burcat *et al.* [53, 54, 94]. The remaining curvefit coefficients were acquired from the NASA/CHEMKIN-PRO[®] database [4, 95].

APPENDIX C: POST PROCESSING ALGORITHM

Overview

The algorithm described in Chapter 3 utilizes the thermodynamic output data from CHEMKIN-PRO[®] to calculate the following variables: (1) species enthalpy, (2) species entropy, (3) mixture entropy, (4) entropy generation, (7) exergy, (8) chemical exergy (8) thermomechanical flow exergy, (9) chemical flow exergy, (10) total mixture flow exergy, (11) exergy destruction, (12) exergetic efficiency, and (13) completeness of combustion. Exergy destruction was calculated two different ways as a means of validating the results. The first method is a direct calculation of the exergy destruction for each plug from the differential form of the exergy balance. The second involves calculating entropy generation for each plug from the differential form of the entropy balance and multiplying by the temperature of the reference environment; this is the definition of exergy destruction (Equation 4.10). Both results should be equal, based on the definitions. The results showed excellent agreement, and any differences were attributed solely to round-off. This method of validation was also used by Dunbar and Lior to confirm their results [2].

Finite-Difference Approximation

Since the governing equations for the plug flow reactor are a set of ordinary differential equations, the first step is to derive a differential expression for entropy generation and exergy destruction for this model. This is accomplished by applying the integral form of the entropy rate balance and exergy rate balance (Equation 4.1) to a differential plug, along with the aforementioned assumptions in Chapter 3.

$$\frac{dS_{cv}}{dt} = \sum_{cs} \frac{\dot{Q}}{T} + \sum_{in} (\dot{m}s)_{in} - \sum_{out} (\dot{m}s)_{out} + \dot{S}_g \quad (C.1)$$

Proper application of the entropy rate balance gives the following expression:

$$\dot{s}'_g \Delta x = \dot{m}_{out} s_{out}(x + \Delta x) - \dot{m}_{in} s_{in}(x) \quad (C.2)$$

Using the result from the mass rate balance (Equation 3.7), dividing through by the mass flow rate and taking the limit, Equation C.2 can be re-expressed as:

$$s'_g = \frac{\dot{s}'_g}{\dot{m}} = \lim_{\Delta x \rightarrow 0} \frac{s_{out}(x + \Delta x) - s_{in}(x)}{\Delta x} = \frac{ds}{dx} \quad (C.3)$$

, or simply

$$s'_g = \frac{ds}{dx} \quad (C.4)$$

Since mass specific entropy is a thermodynamic state variable, it can be expressed as a Taylor Series [96, 97]:

$$s_{i+1} = s_i + \left(\frac{\partial s}{\partial x}\right)_i \Delta x + \left(\frac{\partial^2 s}{\partial x^2}\right)_i \frac{\Delta x^2}{2!} + \left(\frac{\partial^3 s}{\partial x^3}\right)_i \frac{\Delta x^3}{3!} + \dots \quad (C.5)$$

Truncating the higher order terms and leaving the first order term, gives:

$$s_{i+1} = s_i + \left(\frac{\partial s}{\partial x}\right)_i \Delta x \quad (C.6)$$

From Equation C.6, the derivative in Equation C.4 can be approximated by the forward difference method to develop the appropriate difference operators of first-order accuracy [96, 97]:

$$\frac{ds}{dx} \approx \left(\frac{\partial s}{\partial x}\right)_i = \frac{s_{i+1} - s_i}{\Delta x} \quad (C.7)$$

Therefore using this result and Equation C.4 shows that, the entropy generation for each plug can also be approximated as:

$$s'_g \approx \frac{s_{i+1} - s_i}{\Delta x} \Rightarrow s'_g \Delta x \approx s_{i+1} - s_i \quad (\text{C.8})$$

The expression on the right-hand side of Equation C.8 is the approximation of Equation C.2. This is the method used in the post processing algorithm to calculate the entropy generation in the streamwise direction. The same method was used to obtain an expression for exergy destruction, which is given in C.9. Equation C.9 is an approximation of Equation 4.2

$$e'_d \approx \frac{e_i - e_{i+1}}{\Delta x} \Rightarrow e'_d \Delta x \approx e_i - e_{i+1} \quad (\text{C.9})$$

The validation criterion is given as:

$$e'_d \Delta x \approx T_0 s'_g \Delta x \quad (\text{C.10})$$

This is a direct check of the method developed by Washington and Shapiro for calculating the chemical exergy of excited species as well as the overall model. All output variables were verified to a high degree of accuracy.

REFERENCES

- [1] U. S. Department of Energy, "International Energy Outlook 2011," DOE/EIA-0484 ed, 2011.
- [2] W. R. Dunbar and N. Lior, "Sources of Combustion Irreversibility," *Combustion Science and Technology*, vol. 103, pp. 41-61, 12/15/1994.
- [3] A. Bourig, D. Thévenin, J. P. Martin, G. Janiga, and K. Zähringer, "Numerical modeling of H₂-O₂ flames involving electronically-excited species O₂(a¹Δ_g), O(¹D) and OH(²Σ⁺)," *Proceedings of the Combustion Institute*, vol. 32, pp. 3171-3179, 2009.
- [4] "CHEMKIN-PRO," 15112 ed. San Diego: Reaction Design, 2011.
- [5] L. B. Ibraguimova, G. D. Smekhov, and O. P. Shatalov, "Recommended Rate Constants of Chemical Reactions in an H₂-O₂ Gas Mixture with Electronically Excited Species O₂(¹Δ), O(¹D), OH(²Σ) Involved," *Institute of Mechanics of Lomonosov, Moscow State University*, 2003.
- [6] K. K. Kuo, *Principles of Combustion*, 2nd ed. Hoboken: John Wiley & Sons, Inc., 2005.
- [7] M. J. Moran, H. N. Shapiro, D. D. Boettner, and M. B. Bailey, *Fundamentals of Engineering Thermodynamics*, 7th ed. Hoboken: John Wiley & Sons, Inc., 2011.
- [8] A. Starikovskiy and N. Aleksandrov, "Plasma-Assisted Ignition and Combustion," in *Aeronautics and Astronautics*, 1st ed. Rijeka: InTech, 2011.

- [9] M. J. Moran, *Availability Analysis: A Guide to Efficient Energy Use*. Englewood Cliffs: Prentice-Hall, Inc., 1982.
- [10] E. Sciubba and G. Wall, "A brief Commented History of Exergy From the Beginnings to 2004," *International Journal of Thermodynamics*, vol. 10, pp. 1-26, 3/2007.
- [11] C. D. Rakopoulos and E. G. Giakoumis, "Second-law analyses applied to internal combustion engines operation," *Progress in Energy and Combustion Science*, vol. 32, pp. 2-47, 2006.
- [12] J. A. Caton, "Results from the second-law of thermodynamics for a spark-ignition engine using an engine cycle simulation," in *Fall Technical Conference, ASMEICED, ASME*, 1999, pp. 35-49.
- [13] J. A. Caton, "On the destruction of availability (exergy) due to combustion processes — with specific application to internal-combustion engines," *Energy*, vol. 25, pp. 1097-1117, 2000.
- [14] J. A. Caton, "A Review of Investigations Using the Second Law of Thermodynamics to Study Internal-Combustion Engines," in *SAE 2000 World Congress*, Detroit, Michigan, 2000.
- [15] S. C. Kaushik, V. S. Reddy, and S. K. Tyagi, "Energy and exergy analyses of thermal power plants: A review," *Renewable and Sustainable Energy Reviews*, vol. 15, pp. 1857-1872, 2011.

- [16] E. T. Turgut, T. H. Karakoc, and A. Hepbasli, "Exergetic analysis of an aircraft turbofan engine," *International Journal of Energy Research*, vol. 31, pp. 1383-1397, 2007.
- [17] C. S. Daw, K. Chakravarthy, J. C. Conklin, and R. L. Graves, "Minimizing destruction of thermodynamic availability in hydrogen combustion," *International Journal of Hydrogen Energy*, vol. 31, pp. 728-736, 2006.
- [18] A. E. Lutz, R. S. Larson, and J. O. Keller, "Thermodynamic comparison of fuel cells to the Carnot cycle," *International Journal of Hydrogen Energy*, vol. 27, pp. 1103-1111, 2002.
- [19] S. K. Som and A. Datta, "Thermodynamic irreversibilities and exergy balance in combustion processes," *Progress in Energy and Combustion Science*, vol. 34, pp. 351-376, 2008.
- [20] F. P. Incroper and D. P. DeWitt, *Fundamentals of Heat and Mass Transfer*, 5th ed. Hoboken: John Wiley & Sons, Inc., 2002.
- [21] S. Kelly, G. Tsatsaronis, and T. Morosuk, "Advanced exergetic analysis: Approaches for splitting the exergy destruction into endogenous and exogenous parts," *Energy*, vol. 34, pp. 384-391, 2009.
- [22] G. Tsatsaronis and M.-H. Park, "On avoidable and unavoidable exergy destructions and investment costs in thermal systems," *Energy Conversion and Management*, vol. 43, pp. 1259-1270, 6/2002.

- [23] L. J. P. K. G, and W. F. J, "Flame-Arc Combination," *Nature*, vol. 193, pp. 736-738, 1962.
- [24] W. T. Brande, "The Bakerian Lecture: On Some New Electro-Chemical Phenomena," *Philosophical Transactions of the Royal Society of London*, vol. 104, pp. 51-61, 1814.
- [25] A. Ata, J. S. Cowart, A. Vranos, and B. M. Cetegen, "EFFECTS OF DIRECT CURRENT ELECTRIC FIELD ON THE BLOWOFF CHARACTERISTICS OF BLUFF-BODY STABILIZED CONICAL PREMIXED FLAMES," *Combustion Science and Technology*, vol. 177, pp. 1291-1304, 7/1/2005.
- [26] J. Lawton and F. J. Weinberg, *Electrical aspects of combustion* vol. 1: Clarendon Press Oxford, 1969.
- [27] F. J. Weinberg, "Advanced combustion methods," Imperial College of Science and Technology, London 1986.
- [28] I. B. Matveev and L. A. Rosocha, "Guest Editorial Classification of Plasma Systems for Plasma-Assisted Combustion," *Plasma Science, IEEE Transactions on*, vol. 38, pp. 3257-3264, 2010.
- [29] A. Y. Starikovskii, "Plasma supported combustion," *Proceedings of the Combustion Institute*, vol. 30, pp. 2405-2417, 2005.
- [30] A. S. Askarova, E. I. Karpenko, Y. I. Lavrishcheva, V. E. Messerle, and A. B. Ustimenko, "Plasma-Supported Coal Combustion in Boiler Furnace," *Plasma Science, IEEE Transactions on*, vol. 35, pp. 1607-1616, 2007.

- [31] I. B. Matveev, V. E. Messerle, and A. B. Ustimenko, "Investigation of Plasma-Aided Bituminous Coal Gasification," *Plasma Science, IEEE Transactions on*, vol. 37, pp. 580-585, 2009.
- [32] V. E. Messerle, E. I. Karpenko, A. B. Ustimenko, and O. A. Lavrichshev, "Plasma preparation of coal to combustion in power boilers," *Fuel Processing Technology*.
- [33] E. I. Karpenko, V. E. Messerle, and A. B. Ustimenko, "Plasma-aided solid fuel combustion," *Proceedings of the Combustion Institute*, vol. 31, pp. 3353-3360, 2007.
- [34] I. B. Matveev. (2004). *Applied Plasma Technologies, The New Millennium Tools*. Available: <http://www.plasmacombustion.com/index.html>
- [35] H. M. Mott-Smith, "History of "plasmas", " *Nature (London)*, vol. 233, p. 219, 9/17 1971.
- [36] J. E. Harry. (2011). *Introduction to Plasma Technology (1 ed.)*. Available: <http://WAYNE.ebib.com/patron/FullRecord.aspx?p=700925>
- [37] A. F. Aleksandrov, L. S. Bogdankevich, and A. A. Rukhadze, "Principles of plasma electrodynamics," *Moscow Izdatel Vysshaya Shkola*, vol. 1, 1978.
- [38] R. J. Goldston and P. H. Rutherford, *Introduction to plasma physics*: CRC Press, 2010.
- [39] M. Keidar and I. Beilis. (2013). *Plasma Engineering : Applications from Aerospace to Bio and Nanotechnology*. Available: <http://WAYNE.ebib.com/patron/FullRecord.aspx?p=1144217>
- [40] A. Starikovskiy and N. Aleksandrov, "Plasma-assisted ignition and combustion," *Progress in Energy and Combustion Science*, vol. 39, pp. 61-110, 2013.

- [41] A. Bourig, V. Lago, J. Martin, K. Pliavaka, F. Pliavaka, S. Gorbatov, *et al.*, "Generation of singlet oxygen in HV pulsed+ DC crossed discharge at atmospheric pressure for oxygen-enhanced combustion," *International Journal of Plasma Environmental Science and Technology*, vol. 1, pp. 57-63, 2007.
- [42] A. Dutta, Z. Yin, and I. V. Adamovich, "Cavity ignition and flameholding of ethylene–air and hydrogen–air flows by a repetitively pulsed nanosecond discharge," *Combustion and Flame*, vol. 158, pp. 1564-1576, 8/2011.
- [43] N. Popov, "Effect of a pulsed high-current discharge on hydrogen-air mixtures," *Plasma Physics Reports*, vol. 34, pp. 376-391, 2008.
- [44] H. Conrads and M. Schmidt, "Plasma generation and plasma sources," *Plasma Sources Science and Technology*, vol. 9, p. 441, 2000.
- [45] R. M. Badger, A. C. Wright, and R. F. Whitlock, "Absolute Intensities of the Discrete and Continuous Absorption Bands of Oxygen Gas at 1.26 and 1.065 μ and the Radiative Lifetime of the Δ State of Oxygen," *The Journal of Chemical Physics*, vol. 43, p. 4345, 1965.
- [46] R. J. Silbey, R. A. Alberty, and M. G. Bawendi, *Physical Chemistry*, 4th ed. Hoboken: John Wiley & Sons, Inc., 2005.
- [47] H. H. Wasserman and R. W. Murray, *Singlet Oxygen: Organic Chemistry, A Series of Monographs* vol. 40. London: Academic Press, 1979.

- [48] B. Halliwell and J. M. C. Gutteridge, *Free Radicals in Biology and Medicine*. Oxford: Clarendon Press, 1985.
- [49] E. P. Dougherty and H. Rabitz, "Computational kinetics and sensitivity analysis of hydrogen--oxygen combustion," *The Journal of Chemical Physics*, vol. 72, pp. 6571-6586, 1980.
- [50] T. Turányi, "Applications of sensitivity analysis to combustion chemistry," *Reliability Engineering & System Safety*, vol. 57, pp. 41-48, 7/1997.
- [51] M. W. Chase, "JANAF thermochemical tables, 1975 supplement," *Journal of physical and chemical reference data*, vol. 4, p. 1, 1975.
- [52] S. Gordon and B. J. McBride, *Computer program for calculation of complex chemical equilibrium compositions, rocket performance, incident and reflected shocks, and Chapman-Jouguet detonations* vol. 197: NASA, 1971.
- [53] A. Burcat and W. C. Gardiner, *Combustion chemistry*: Springer, 1984.
- [54] A. Burcat and B. Ruscic, *Third millenium ideal gas and condensed phase thermochemical database for combustion with updates from active thermochemical tables*: Argonne National Laboratory Argonne, IL, 2005.
- [55] S. R. Turns, *An Introduction to Combustion: Concepts and Applications*, 2nd ed. Boston: McGraw-Hill, 2000.
- [56] J. B. Butt, *Reaction kinetics and reactor design*: CRC Press, 2000.

- [57] K. G. Denbigh and J. C. R. Turner, *Chemical reactor theory: an introduction*: CUP Archive, 1984.
- [58] H. S. Fogler, "Elements of chemical reaction engineering," 1999.
- [59] D. A. Washington and H. N. Shapiro, "A Phenomenological Analysis of Exergy Destruction during Hydrogen Combustion with Electronically Excited Oxygen, Power2013-98169," presented at the ASME 2013 Power Conference, Boston, 2013.
- [60] A. Bejan, G. Tsatsaronis, and M. Moran, *Thermal Design and Optimization*, 1st ed. New York: John Wiley & Sons, Inc., 1996.
- [61] J. Etele and M. A. Rosen, "Sensitivity of exergy efficiencies of aerospace engines to reference environment selection," *Exergy, An International Journal*, vol. 1, pp. 91-99, 2001.
- [62] D. R. Morris and J. Szargut, "Standard chemical exergy of some elements and compounds on the planet earth," *Energy*, vol. 11, pp. 733-755, 1986.
- [63] J. Szargut, D. R. Morris, and F. R. Steward, *Exergy Analysis of Thermal, Chemical, and Metallurgical Processes*. New York: Hemisphere Publishing Corporation, 1988.
- [64] J. H. Van Gerpen and H. N. Shapiro, "Second-Law Analysis of Diesel Engine Combustion," *Journal of Engineering for Gas Turbines and Power*, vol. 112, pp. 129-137, 1990.

- [65] G. Tsatsaronis, J. Pisa, and L. Gallego, "Chemical exergy in exergoeconomics," in *Proceedings of the International Symposium of Thermodynamics Analysis and Improvement of Energy Systems, Beijing China*, 1989, pp. 195-200.
- [66] S. Ismail and P. S. Mehta, "Second law analysis of hydrogen–air combustion in a spark ignition engine," *International Journal of Hydrogen Energy*, vol. 36, pp. 931-946, 2011.
- [67] J. H. Lehman, M. I. Lester, and D. R. Yarkony, "Reactive quenching of OH $A^2\Sigma^+$ by O₂ and CO: Experimental and nonadiabatic theoretical studies of H- and O-atom product channels," *The Journal of Chemical Physics*, vol. 137, pp. 094312-14, 2012.
- [68] R. A. Young, G. Black, and T. G. Slanger, "Reaction and Deactivation of O(¹D)," *The Journal of Chemical Physics*, vol. 49, pp. 4758-4768, 1968.
- [69] D. R. Kearns, "Physical and chemical properties of singlet molecular oxygen," *Chemical Reviews*, vol. 71, pp. 395-427, 8/1/1971.
- [70] J. J. McKetta Jr, *Chemical processing handbook*: CRC Press, 1993.
- [71] D. Veynante and L. Vervisch, "Turbulent combustion modeling," *Progress in energy and combustion science*, vol. 28, pp. 193-266, 2002.
- [72] I. Glassman and R. A. Yetter, *Combustion* 4th ed. San Diego: Academic Press, 2008.
- [73] G. L. Schott and J. L. Kinsey, "Kinetic Studies of Hydroxyl Radicals in Shock Waves. II. Induction Times in the Hydrogen-Oxygen Reaction," *The Journal of Chemical Physics*, vol. 29, pp. 1177-1182, 1958.

- [74] F. A. Williams, "Detailed and reduced chemistry for hydrogen autoignition," *Journal of Loss Prevention in the Process Industries*, vol. 21, pp. 131-135, 3/2008.
- [75] L. Clifford, A. Milne, T. Turanyi, and D. Boulton, "An induction parameter model for shock-induced hydrogen combustion simulations," *Combustion and flame*, vol. 113, pp. 106-118, 1998.
- [76] S. M. Sarathy, S. Vranckx, K. Yasunaga, M. Mehl, P. Oßwald, W. K. Metcalfe, *et al.*, "A comprehensive chemical kinetic combustion model for the four butanol isomers," *Combustion and Flame*, vol. 159, pp. 2028-2055, 6/2012.
- [77] T. Weydahl, M. Poyyapakkam, M. Seljeskog, and N. E. L. Haugen, "Assessment of existing H₂/O₂ chemical reaction mechanisms at reheat gas turbine conditions," *International Journal of Hydrogen Energy*, vol. 36, pp. 12025-12034, 9/2011.
- [78] M. Poyyapakkam, J. Wood, S. Mayers, A. Ciani, F. Guethe, and K. Syed, "HYDROGEN COMBUSTION WITHIN A GAS TURBINE REHEAT COMBUSTOR," 2012.
- [79] W. SUN and Y. JU, "2. Nonequilibrium Plasma-Assisted Combustion: A Review of Recent Progress." *J. Plasma Fusion Res.*, vol. 89, pp. 208-219, 2013.
- [80] N. Popov, "The effect of nonequilibrium excitation on the ignition of hydrogen-oxygen mixtures," *High Temperature*, vol. 45, pp. 261-279, 2007.
- [81] D. Hamby, "A review of techniques for parameter sensitivity analysis of environmental models," *Environmental Monitoring and Assessment*, vol. 32, pp. 135-154, 1994.

- [82] J. Warnatz, U. Maas, and R. W. Dibble, *Combustion: Physical and Chemical Fundamentals, Modeling and Simulation, Experiments, Pollutant Formation*, 4th ed. Heidelberg: Springer, 2010.
- [83] S. Burke and H. Curran, "Uncertainties in rate constants of important reactions for propene oxidation."
- [84] V. Dias, C. Duynslaegher, F. Contino, J. Vandooren, and H. Jeanmart, "Experimental and modeling study of formaldehyde combustion in flames," *Combustion and Flame*, vol. 159, pp. 1814-1820, 5/2012.
- [85] C. K. Westbrook, Y. Mizobuchi, T. J. Poinso, P. J. Smith, and J. Warnatz, "Computational combustion," *Proceedings of the Combustion Institute*, vol. 30, pp. 125-157, 1/2005.
- [86] D. Beerer and V. McDonell, "Autoignition of hydrogen and air inside a continuous flow reactor with application to lean premixed combustion," *Transactions of the ASME-A-Engineering for Gas Turbines and Power*, vol. 130, pp. 51507-51600, 2008.
- [87] T. Ombrello, S. H. Won, Y. Ju, and S. Williams, "Flame propagation enhancement by plasma excitation of oxygen. Part I: Effects of O₃," *Combustion and Flame*, vol. 157, pp. 1906-1915, 10/2010.
- [88] T. Ombrello, S. H. Won, Y. Ju, and S. Williams, "Flame propagation enhancement by plasma excitation of oxygen. Part II: Effects of O₂(a¹Δ_g)," *Combustion and Flame*, vol. 157, pp. 1916-1928, 10/2010.

- [89] E. V. Kustova, E. A. Nagnibeda, and A. H. Chauvin, "State-to-state nonequilibrium reaction rates," *Chemical Physics*, vol. 248, pp. 221-232, 1999.
- [90] D. Bruno, M. Capitelli, E. Kustova, and E. Nagnibeda, "Non-equilibrium vibrational distributions and transport coefficients of N₂(v)-N mixtures," *Chemical Physics Letters*, vol. 308, pp. 463-472, 7/30/1999.
- [91] A. Chikhaoui, J. P. Dudon, E. V. Kustova, and E. A. Nagnibeda, "Transport properties in reacting mixture of polyatomic gases," *Physica A: Statistical Mechanics and its Applications*, vol. 247, pp. 526-552, 12/15/1997.
- [92] E. V. Kustova and E. A. Nagnibeda, "Strong nonequilibrium effects on specific heats and thermal conductivity of diatomic gas," *Chemical Physics*, vol. 208, pp. 313-329, 8/15/1996.
- [93] Y. Candau, "On the exergy of radiation," *Solar Energy*, vol. 75, pp. 241-247, 9/2003.
- [94] A. Burcat. (2006). *Laboratory for Chemical Kinetics - Institute of Chemistry, Eotvos University*. Available: <http://garfield.chem.elte.hu/Burcat/burcat.html>
- [95] B. McBride, S. Gordon, and M. Reno, "NASA Technical Memorandum 4513," 10/1993.
- [96] T. I.-P. Shih, *Fundamentals of Computational Fluid Dynamics*. East Lansing, MI: Department of Mechanical Engineering, Michigan State University, 2003.
- [97] J. C. Tannehill, D. D. A. Anderson, and R. H. Pletcher, *Computational fluid mechanics and heat transfer*: Taylor & Francis, 1997.

ABSTRACT**EXERGETIC ANALYSIS OF HYDROGEN COMBUSTION INVOLVING
ELECTRONICALLY EXCITED SPECIES**

by

DeVon A. Washington**August 2013****Advisors:** Dr. Howard N. Shapiro
Dr. Trilochan Singh**Major:** Mechanical Engineering**Degree:** Doctor of Philosophy

Plasma-assisted combustion (PAC) is a growing field of research that involves using nonthermal plasma (NTP) to enhance combustion. PAC research involves modeling reaction mechanisms and chemical kinetics. Exergy analysis of combustion devices focuses on combustion irreversibility, including mixing, internal heat transfer, and oxidation. This novel research project merges these two branches of research.

The focus of this work is the application of exergy analysis to PAC systems, to analyze the effect introducing NTP has on trends in exergy destruction associated with oxidation during hydrogen combustion. This was accomplished by developing a plug flow reactor model using the chemical simulation tool CHEMKIN-PRO[®] in conjunction with a reaction mechanism which includes explicit reaction pathways for NTP.

The primary results of the study identify an optimal range of exergetic efficiency when NTP composes between 0% - 20% of the oxidizer for a stoichiometric fuel-oxidizer ratio. Beyond 25% there is a dramatic reduction in the total exergy destruction before ignition. Additionally, the presence of NTP reduces the molar conversion of fuel while maintaining

slightly higher than normal combustion temperatures, which results in an increase in the exit chemical flow exergy; presenting an opportunity to extract additional work. Finally, when NTP is introduced into the combustion process, it creates reaction pathways which dominate the production of key radicals and chain carriers that drive the trends in exergy destruction. A detailed understanding of these characteristics informs how NTP can be used to enhance combustion efficiency and reduce fuel use to achieve desired energy conversion.

AUTOBIOGRAPHICAL STATEMENT

- Education** Doctor of Philosophy, Mechanical Engineering, Wayne State University, Detroit, Michigan, 2013
- Master of Science, Mechanical Engineering, Michigan State University, East Lansing, Michigan, 2004
- Bachelor of Science, Mechanical Engineering, Michigan State University, East Lansing, Michigan, 2001
- Employment** Consumers Energy, Engineering Services Department, Jackson, Michigan, 2001-Present, Senior Engineer/Project Manager
- Publications** Washington, D.A., Shapiro, H.N., 2013, “A Phenomenological Analysis of Exergy Destruction during Hydrogen Combustion with Electronically Excited Oxygen, Power2013-98169”, Proceedings of the ASME 2013 Power Conference, Boston, MA
- Presentations** Washington, D.A., Shapiro, H.N., “A Phenomenological Analysis of Exergy Destruction during Hydrogen Combustion with Electronically Excited Oxygen”, ASME 2013 Power Conference – Oral Presentation, July 30, 2013, American Society of Mechanical Engineers, Boston, MA
- Washington, D.A., Shapiro, H.N., “Exergetic Analysis of Hydrogen Combustion Involving Electronically Excited Species”, Michigan Department of Environmental Quality, 2012 Michigan Green Chemistry and Engineering Conference: Driving Sustainable Manufacturing – Poster Presentation, October 26, 2012, Wayne State University, Detroit, Michigan
- Washington, D.A., Shapiro, H.N., “Exergetic Analysis of Hydrogen Combustion Involving Electronically Excited Species”, Sixteenth Annual Michigan Space Grant Consortium Fall Conference – Poster Presentation, October 06, 2012, University of Michigan, Ann Arbor, Michigan
- Washington, D.A., Shapiro, H.N., “Exergetic Analysis of Hydrogen Combustion Involving Electronically Excited Species”, Third Annual Wayne State University Graduate Research Exhibition – Poster Presentation (third place winner), March 6, 2012, Wayne State University, Detroit, Michigan
- Awards** Michigan Space Grant Consortium Graduate Fellowship Program, 2010-2013
- NACME Alfred P. Sloan Foundation Graduate Scholarship Program, 2002-2004